

ROLE OF PRE-EXISTING STACKING FAULTS IN THE MECHANICAL
RESPONSE OF METALLIC MATERIALS: A MOLECULAR DYNAMICS STUDY

by
Dajla Neffati

A dissertation submitted to the department of mechanical engineering,
University of Houston
in partial fulfillment of the requirements for the degree of
DOCTOR OF PHILOSOPHY
in Mechanical Engineering

Chair of Committee: Yashashree Kulkarni
Committee Member: Roberto Ballarini
Committee Member: Theocharis Baxevanis
Committee Member: Shailendra Joshi
Committee Member: Pradeep Sharma

University of Houston

May 2020

Copyright 2020, Dajla Neffati

DEDICATION

*To my family and friends, for being there
through the ups and downs.*

ACKNOWLEDGEMENTS

My deepest and sincerest gratitude goes to my advisor, Dr. Yashashree Kulkarni, for her guidance and advice, her acceptance and kindness and for playing a big part in shaping me, both on a personal and professional level, into the individual that I am today and for encouraging and challenging me to reach my potential.

I would like to express my gratitude towards Dr. Pradeep Sharma for accepting me in his group as an intern and opening a window to this opportunity.

I'm deeply thankful towards the committee members, Dr. Shailendra Joshi, Dr. Theocharis Baxevanis and Dr. Roberto Ballarini, and all the teachers and professors who have contributed to my academic journey. My parents have raised me to always respect my teachers regardless of the situation, I had a hard time accepting that most of my life, but with the years, I came to understand how noble and selfless the teaching mission is.

I would also like to thank our collaborators Dr. Xinghang Zhang and his student, Ruizhe Su, for being such a wonderful team and their help and encouragement.

I consider myself lucky for having met my current and former labmates and friends. I'm very grateful towards them from making this tough journey considerably easier by creating a positive work atmosphere and being supportive and helpful throughout the years.

To my Tunisian community in Houston, especially Sana and Farah, for being like sisters and offering help and support whenever needed, I am forever grateful.

Last but not least, I would never be able to express how indebted I am to my parents, my brother and my husband, for their sacrifice, their support and their unconditional love. This thesis is my humble tribute to them.

ABSTRACT

Nanostructured metallic materials have gained significant interest for their superior performance in the fields of electronics, energy, defense and structural applications. They owe their outstanding mechanical properties to abundant interfaces such as grain boundaries and phase boundaries as well as nanoscale features such as grain size. The role of grain boundaries, twin boundaries, and other interfaces on mechanical response of materials has been richly investigated over decades. In contrast, stacking faults, which are also planar defects, have primarily been studied as defects that arise during deformation. Recent experimental work by our collaborators on hexagonal-closed packed (HCP) and face centered cubic (FCC) Co with stacking faults enables the investigation of how stacking faults may govern the deformation of metallic materials. This dissertation presents an atomistic study of the deformation mechanisms in HCP, FCC metals and nanostructured metallic multilayers dominated by pre-existing stacking faults and other planar defects.

First, nanopillar compression is used to investigate the deformation mechanisms in HCP Co with high density stacking faults. Molecular dynamics (MD) simulations reveal high yield strength and significant plasticity owing to stacking fault induced deformation mechanisms that activate phase transformation.

Second, we use MD simulations to show that FCC (111)Cu/HCP (0002)Co multilayers with an incoherent layer interface have dramatically better mechanical performance than FCC/FCC (100) and (110) Cu/Co multilayers with a coherent layer interface. Our study reveals a unique interplay among twin boundaries in Cu, stacking faults in HCP Co, and incoherent layer interfaces, which leads to partial dislocation dominated high strength and outstanding plasticity. We further perform MD simulations to investigate the distinct role of each of these pre-existing planar defects on the mechanical behavior of FCC Cu/ HCP Co multilayers.

Finally, we perform MD simulations on FCC Co nanopillars. They reveal that the

stacking faults and partial dislocations activity dominate the hardening and softening observed during plastic deformation of FCC Co where abundant dislocation junctions favor strengthening.

Our simulations, together with experimental data, provide compelling evidence that pre-existing stacking faults can enhance strength and plasticity and suggest future avenues for the design of nanostructured materials with optimized properties using defect networks.

TABLE OF CONTENTS

DEDICATION	iii
ACKNOWLEDGEMENTS	iv
ABSTRACT	v
TABLE OF CONTENTS	vii
LIST OF FIGURES	x
1 INTRODUCTION	1
1.1 Motivation	1
1.1.1 Grain Boundaries and Twin Boundaries	3
1.1.2 Stacking Faults	6
1.1.3 Layer Interfaces in Metallic Multilayers	11
1.2 Computational Modeling	13
1.2.1 Fundamentals of Molecular Dynamics	15
1.2.2 Visualization	17
1.3 Dissertation Outline	18
2 PHASE TRANSFORMATION INDUCED PLASTICITY IN HEXAGONAL CLOSE PACKED CO WITH STACKING FAULTS	20
2.1 Introduction	20

2.2	Experimental and Computational Methods	22
2.2.1	Simulation Method	22
2.2.2	Experimental Methods	22
2.3	Computational Results	23
2.4	Experimental Results	25
2.5	Discussion	27
2.6	Conclusion	29
3	ORIENTATION-DEPENDENT MECHANICAL RESPONSE OF CU-CO MULTILAYERS	30
3.1	Introduction	30
3.2	Computational and Experimental Methods	32
3.2.1	Computational Methods	32
3.2.2	Experimental Methods	33
3.3	Computational Results	33
3.4	Experimental Results	38
3.5	Discussion	43
3.5.1	Strain Hardening and Deformation Mechanisms of FCC Cu/Co Multilayers	43
3.5.2	Origins of Ultra-high Strength and Plasticity in Cu (111)/Co (0002) Multilayer System	46
3.5.3	Unique Morphology and Significant Deformability Of Cu (111)/Co (0002) Pillars	51
3.6	Conclusion	53
4	DEFECT NETWORK IN FCC CU/HCP CO MULTILAYERS	54
4.1	Introduction	54
4.2	Simulation and Experimental Methods	55

4.2.1	Simulation Methods	55
4.2.2	Experimental Methods	57
4.3	Computational Results	57
4.3.1	The Role of Pre-existing TBs in Cu	57
4.3.2	The Role of Pre-existing SFs in Co	59
4.3.3	The Role of Coherent versus Incoherent Interface	64
4.4	Experimental Results	67
4.5	Discussion	69
4.5.1	TBs and SFs Strengthening Effects in (111)Cu/(0002)Co Multilayers	69
4.5.2	Interface Dominated Deformation in Cu/Co Multilayers	71
4.6	Conclusion	72

**5 DEFORMATION MECHANISMS IN FACE CENTERED CUBIC
CO DOMINATED BY STACKING FAULTS 74**

5.1	Introduction	74
5.2	Computational and Experimental Methods	75
5.2.1	Computational Methods	75
5.2.2	Experimental Methods	75
5.3	Computational Results	77
5.4	Experimental Results	81
5.5	Discussion	83
5.5.1	Strengthening and Softening Mechanisms in FCC Co Revealed by MD Simulations	83
5.5.2	Strain Rate Dependent Deformation Mechanisms in FCC Co with SFs	84
5.6	Conclusion	88

6 SUMMARY	90
REFERENCES	94

LIST OF FIGURES

1.1	Two-dimensional representations of a typical GB (a) and a defect-less TB (b) [1].	3
1.2	Tensile response for NT Cu samples with different twin spacings for two grain sizes by MD simulations [2].	5
1.3	A perfect Face-Centered Cubic crystal layer stacking (left) versus structure with an interrupted stacking creating a SF (right).	6
1.4	Slip systems in an HCP single crystal [3].	8
1.5	The strength vs individual layer thickness for NMMs [4].	11
2.1	MD simulations of compression of HCP Co pillar with parallel SFs. Atoms are in common neighbor color coding (orange for FCC, purple for HCP and white for unidentified structures). Green and red lines represent Shockley partials and red lines represent other dislocations, respectively.	23
2.2	MD simulations of compression tests of HCP Co pillar with parallel SFs. Coloring of atoms is according to the Von Mises shear strain for various configurations during deformation.	24
2.3	MD simulations of compression tests of HCP Co pillar without SFs. Atoms are in common neighbor color coding where orange, purple and white denote FCC, HCP and unidentified structures, respectively. . .	25

2.4	In situ micropillar compression tests on HCP Co. (a) True stress-strain curves. (b-e) SEM snapshots of an HCP Co pillar showing uniform deformation during compression. No cracks were observed.	26
2.5	Cross-section TEM micrographs of an HCP Co pillar deformed to $\sim 20\%$ true strain. (a) A TEM micrograph at low magnification. (b) A higher magnification TEM micrograph of the box (in a). (c,d) HRTEM micrographs of the boxes in (b).	27
3.1	Comparison of MD simulation results for the FCC (100) and (110) Cu/Co 5 nm multilayer nanopillars. (a-b) Stress-strain curves. (c-f) Microstructure and dislocation analyses of FCC (100) and (110) multilayer at different levels of strain. orange, purple and white atoms are in FCC, HCP and unidentified structures, respectively.	34
3.2	Dislocation analysis of the deformed FCC (100) and (110) Cu/Co 5 nm multilayer nanopillars during compression showing only defects. Green, yellow and blue lines denote Shockley partials, Hirth locks, and perfect dislocations, respectively. Red lines denote other dislocations.	35
3.3	MD simulation results for the compression of FCC Cu (111)/ HCP Co (0002) 5 nm nanopillars. (a) The true stress-strain curve. (b-c) Cu/Co pillar before deformation. (d-f) Cross-section view of the pillar at different stages of deformation where atoms are in common neighbor color coding.	36
3.4	Top view of the simulated interfaces between Cu and Co before compression in (a) (100) Cu/Co, (b)(110) Cu/Co and (c) Cu (111)/Co (0002) multilayers in common neighbor color coding. Pink is for unidentified structure.	37
3.5	Dislocation analysis of the FCC Cu (111)/ HCP Co (0002) 5 nm nanopillar at different stages of compression showing only defect	

	atoms and dislocation lines where Shockley partials are in green, full dislocations in blue, stair-rod in pink other dislocation are in red.	38
3.6	Comparison of the microstructures of three Cu/Co 25 nm multilayers with different types of layer interfaces. (a, f, k) XRD profiles. (b, g, l) Cross-section EDS maps of Cu/Co nanolayers. Cross-section TEM (XTEM) micrographs of (c-e) FCC Cu/Co (100), (h-j) FCC Cu/Co (110) and (m-o) Cu (111)/Co (0002).	39
3.7	In situ micropillar compression tests for the three Cu/Co multilayer systems obtained at a strain rate of 5×10^{-3} /s.(a) True stress-strain curves of Cu/Co (100) and (110) multilayers.(b) Engineering stress-strain curves. SEM snap shots of (c1-c4) Cu/Co (100), (d1-d4) Cu/Co (110) and (e1-e4) Cu (111)/Co (0002) during compression.	41
3.8	Comparison of the flow stress (true stress at 5-10% true strain) of Cu/Co multilayers to other 'ductile' multilayers under pillar compression.	42
3.9	Snapshots of MD simulations showing SFs crossing the Cu-Co interface after yield in (100) and (110) Cu/Co multilayers where only atoms of the SF (purple) and Shockley partials (green lines) are depicted.	43
3.10	XTEM micrographs of the FCC (110) Cu/Co pillar after compression at 20% strain.	44
3.11	Snapshots of MD simulations at $\sim 6.5\%$ showing twin growth in (110) Cu/Co multilayers. (a) Atoms are in Common Neighbor color coding. (b) A close-up of the steps on TBs caused by the intersection with SFs lead by Shockley partials (green lines).	45
3.12	XTEM micrographs and EDS maps of the deformed Cu (111)/Co (0002) pillar. (a1,a2) EDS maps of Cu (111)/Co (0002) pillar after deformation to 5% true strain. (a3,a4) XTEM micrographs at the center of the pillar. (b1,b2) EDS map of the multilayers at 20% true	

strain. (b3, b4) HRTEM micrographs of an extruded but less deformed portion of the pillar top.	49
3.13 Top view of the interface between Cu (111) and Co (0002) at different strain levels. Atoms are in Common Neighbor color coding, where orange is for FCC and purple is for HCP.	50
3.14 Cross-section of the Cu (111)/Co (0002) multilayers after deformation at ~14% strain. (a) Atoms are in Common Neighbor color coding. (b) Atoms are in atom type color coding where Co atoms are green and Cu atoms are red.	51
4.1 MD simulations of compression of (111)Cu/(0002) Co nanopillars with and without pre-existing TBs in Cu in common neighbor color coding (orange is for FCC, purple for HCP and grey for unidentified structure). Green and pink lines are Shockley partials and stair-rod dislocations, respectively.	58
4.2 MD simulations of compression of (111)Cu/(0002) Co nanopillars with and without pre-existing SFs in Co in common neighbor color coding. Green and pink lines are Shockley partials and stair-rod dislocations, respectively.	60
4.3 MD simulations of compression of (111)Cu/(0002) Co nanopillars with 1 nm (c1-c4), 2 nm (d1-d4) and 3.3 nm (e1-e4) SF spacing in Co in common neighbor color coding. Green and pink lines are Shockley partials and stair-rod dislocations, respectively.	62
4.4 MD simulations of compression of (111)Cu/(0002) Co nanopillars with and without pre-existing defects in common neighbor color coding. Green and pink lines are Shockley partials and stair-rod dislocations in Cu, respectively. In Co, $1/3\langle 1\bar{2}10 \rangle$, $1/3\langle 1\bar{1}00 \rangle$ and other dislocations are green, orange and red, respectively.	64

4.5	MD simulation of compression of FCC Cu/FCC Co 5 nm (b) and FCC Cu/HCP Co 10 nm nanopillars (c). (a) Stress-strain curves. (b,c) Pillars before deformation. Microstructural evolution and dislocation activity in (d-f) FCC Cu/FCC Co pillar and (g-i) in FCC Cu/HCP Co pillar in common neighbor color coding.	66
4.6	In-situ micropillar compression results of Cu/Co multilayers with different h. (a1, b1, c1) Engineering stress-strain curves. SEM images of Cu/Co (a2-a5) 5 nm, (b2-b5) 25 nm and (c2-c5) 100 nm multilayers.	68
4.7	TEM (a) and STEM (b) micrographs of Cu/Co 5 nm pillar deformed up to 20% strain. (c),(d) HRTEM micrographs of two different zones of the deformed pillar defined in (b).	72
5.1	(a)Plan-view TEM micrograph from the Co [100] zone axis. (b-c) Cross-section TEM (XTEM) micrographs examined from the Co [110] zone intersecting SF ribbons that keep propagating after interception. (d) HRTEM micrograph.	76
5.2	MD simulation results for compression of a Cu-Co bilayer nanopillar. (a1) Cross-section view of the pillar before deformation. (a2)A tilted top-down view of initial SFs formed in FCC Co. (a3) Shockley partials (green) and Hirth locks ($\mathbf{b}=1/3 \langle 100 \rangle$, black).The stress-strain curves for nanopillar compression at a strain rate of (b) $1.37 \times 10^8/s$ and (c) $1.37 \times 10^9/s$	77
5.3	Nanostructure evolution at different strains during Region I and II in common neighbor color coding using dislocation analysis. Only defect atoms arranged in HCP structure are shown(orange). Using dislocation analysis, the green lines show Shockley partials (SP), Hirth locks (HL) are in black, and the red lines show other types of dislocations.	79
5.4	Nanostructure evolution at different strains during Region III and IV	

	in common neighbor analysis (orange is for HCP, grey for FCC and pink for BCC) along with dislocation analysis.	80
5.5	In situ micropillar compression tests of FCC (100) Co at different strain rates. (a) At low strain rate ($1 \times 10^{-3}/s$, red), at high strain rate ($5 \times 10^{-3}/s$, blue). (b) True stress-true strain curves of jump test at different strain rate ($5 \times 10^{-4}/s$ - $1 \times 10^{-2}/s$).	81
5.6	SEM images obtained from in situ compression tests of FCC (100) Co pillars at (a) $1 \times 10^{-3}/s$ and (b) $5 \times 10^{-3}/s$ strain rates and (c) a jump test with a varying strain rate.	82
5.7	Dislocation analysis of MD simulations at the valley and peak of Region III on both stress-strain curves of relatively (a) low ($1.37 \times 10^8/s$) and (b) high ($1.37 \times 10^9/s$) strain rates. The density (c) and number (d) of Hirth locks function of the strain at low and high strain rates. . . .	87

Chapter 1

INTRODUCTION

1.1 Motivation

Interfaces and interfacial phenomena play a vital role in the physical behavior of materials across multiple spatio-temporal scales. The scientific and technological implications of interfacial processes are immense, ranging from electronics, and energy industry to defense and structural applications. With the advent of nanotechnology, interfaces have gained even more prominence owing to their impact on the properties of nanostructured materials and have been the subject of intense research theoretically, experimentally, and computationally [2, 5, 6, 7, 8, 9, 10, 11, 12, 13, 14, 15, 16, 17, 18, 19, 20]. In metallic materials, which are the focus of this study, interfaces refer to grain boundaries, twin boundaries or phase boundaries and metal-metal interfaces. As discussed in detail in the following sections, these planar defects play a vital role in governing the mechanical properties (as well as electrical, optical, and thermal properties) of metals and metallic alloys. For example, twin boundaries and grain boundaries can resist the transmission of dislocations to increase strength, while twin boundaries also accumulate dislocations to accommodate plasticity, and do not scatter electrons as much as regular grain boundaries do to permit high electric

conductivity [21, 22, 23, 24, 25, 26, 27, 28, 29, 30, 31, 32, 33, 34, 35, 36, 37, 38]. Similarly, metal-metal interfaces have shown very attractive role in imparting radiation tolerance in metallic multilayers as they serve as effective barriers for radiation-induced point defects [39, 40, 41, 42, 43, 44].

Stacking faults are also planar defects on which we have a rich literature based on research going back decades [45, 46]. Interestingly, however, stacking faults have been studied primarily as defects that arise commonly during deformation in metallic materials [47, 48, 49]. This begs the question: If stacking faults are planar defects like grain boundaries and twin boundaries, can they play a role in enhancing mechanical properties such as strength and ductility? This fundamental materials science question has been largely unaddressed until very recently. Recently, our experimental collaborators, Zhang et al. [50] were able to synthesize FCC Co at room temperature by using an epitaxial Cu seed layer. Since Co is naturally in HCP phase at room temperature, this stabilization of FCC Co resulted in the formation of high density stacking faults in FCC Co. This presented an unprecedented opportunity to examine the role of pre-existing stacking faults on the mechanical behavior of FCC and HCP metals, as well as metallic multilayers. This is primarily the focus of this dissertation. In this dissertation, we will present our work on atomistic simulations of FCC and HCP Co and Cu/Co multilayers that provide insights into the role of pre-existing stacking faults and other planar defects in the mechanical behavior of these materials.

In the rest of this chapter, we will provide a review of existing studies on grain boundaries, twin boundaries, stacking faults and multilayers. These are broad topics that have been investigated via experiments and computational modeling on various length scales. We will restrict our discussion to atomistic modeling results and experimental data that are more germane to our current study.

1.1.1 Grain Boundaries and Twin Boundaries

A grain boundary (GB) is the interface separating two adjacent grains with different orientations in a polycrystalline material (Figure 1.1(a)). A twin boundary (TB) is a special type of GB that is highly symmetric because the grain on one side of the interface is a mirror reflection of the grain on the other side as depicted by Figure 1.1(b) illustrating a TB in an FCC structure. Although the TB is a high angle GB, its high symmetry lowers its energy.

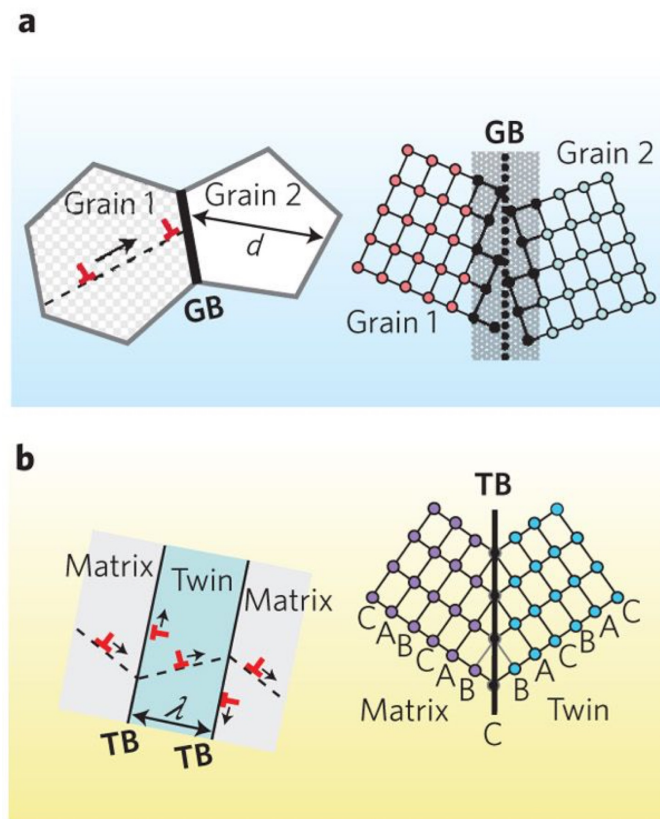


Figure 1.1: Two-dimensional representations of a typical GB (a) and a defect-less TB (b) [1].

Nanocrystalline Metals

The mechanical properties of nanocrystalline materials with GBs deviate from those of a single crystal due to the dimensions of the nanometer-sized grains as well

as the high density of interfaces. The increase in strength of polycrystalline materials arises from the GBs acting as effective barriers for dislocation motion, inhibiting the onset of plasticity. The Hall-Petch relation links the yield strength σ_y to the grain size d as

$$\sigma_y = \sigma_0 + kd^{-\frac{1}{2}}, \quad (1.1)$$

where σ_0 is the intrinsic strength of a material having a dislocation density low enough so that dislocation interactions are inconsequential and k is a d -independent constant. It is an empirical relationship and the strengthening coefficient is material specific and is typically obtained from experimental data. Several studies have focused on determining the optimal dimensions for enhancing the mechanical properties of nanocrystalline materials [7, 27, 51, 52, 53, 54, 55, 56, 57, 58, 59, 60, 61, 62].

Nanotwinned Metals

A novel class of nanostructured materials was developed in early 2000's known as nanotwinned metals which have ultra-fine grains containing twin boundaries with spacing around 20-100 nm [63]. The ultra-high yield strength and ductility observed in nanotwinned metals as well as enhancement of other properties including high strain rate sensitivity and electrical conductivity motivated further research on them.

Experimental research has shown that nanotwinned metals have higher tensile and yield strengths as well as better hardness than nanocrystalline metals owing to the dislocations/TB interactions [21, 63, 64, 65]. Interactions between CTBs and dislocations and their impact on strength and ductility have been extensively investigated using atomistic simulations by several research groups [26, 58, 66, 67, 68, 69, 70]. In fact, dislocations accumulate against TBs making them a strong barrier to dislocation motion increasing strength, similar to GBs. CTB-dislocation interactions lead to dislocation dissociation which results in either multiple partial dislocations propagating through the CTB or along it or producing a sessile dislocation lock at the

CTB depending on the type of metal chosen and the applied strain [26, 66]. Thus, in contrast to GBs, CTBs accommodate plasticity and improve ductility because partial dislocations can glide along their (111) planes through the process of absorption and transmission [67]. MD simulations of nanoindentation on monocrystalline and nanotwinned BCC Ta films with different twin thickness show that three kinds of dislocation-TB interaction namely absorption, desorption and direct transmission activate the migration of TBs, the formation of steps along TBs, and the formation of new sites for dislocation nucleation, inducing softening in samples with small twin lamellae [70].

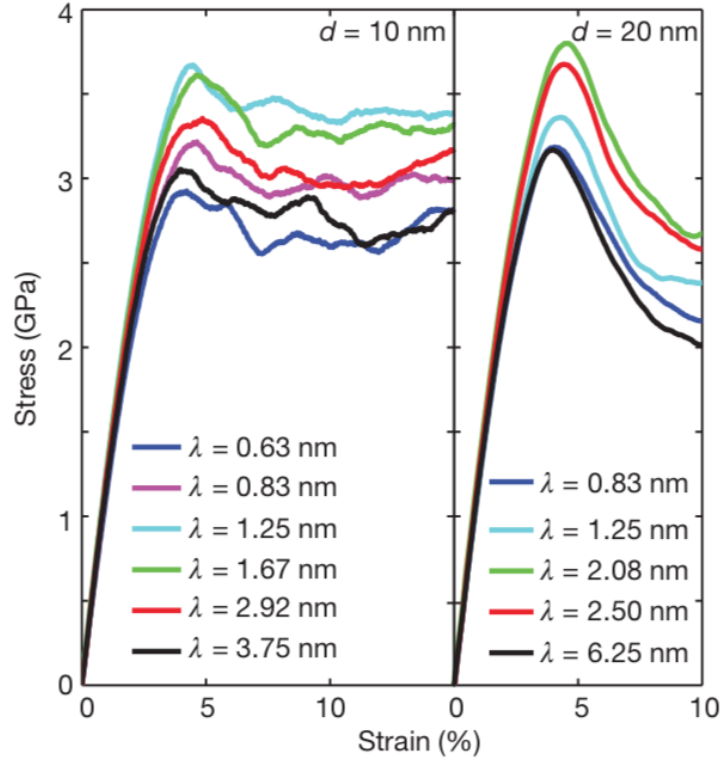


Figure 1.2: Tensile response for NT Cu samples with different twin spacings for two grain sizes by MD simulations [2].

The deformation mechanisms of nanotwinned Cu with a wide range of twin spacing were studied by Li et al. [2] via molecular dynamics and theoretical modeling. Below

a critical twin spacing, softening occurs in the presence or the absence of pre-existing dislocations. Dislocations nucleating from the GB-twin intersections and propagating parallel to TBs govern softening. They found that a finer grain size leads to a smaller critical twin spacing and a higher maximum strength of the material (Figure 1.2).

1.1.2 Stacking Faults

Structure and Characteristics

A perfect crystal consists of identical atomic layers arranged in a regular sequence called stacking. Stacking faults (SFs) are planar defects and as the name implies, they are local regions in the crystal where the regular atomic layer arrangement is interrupted as illustrated in Figure 1.3.

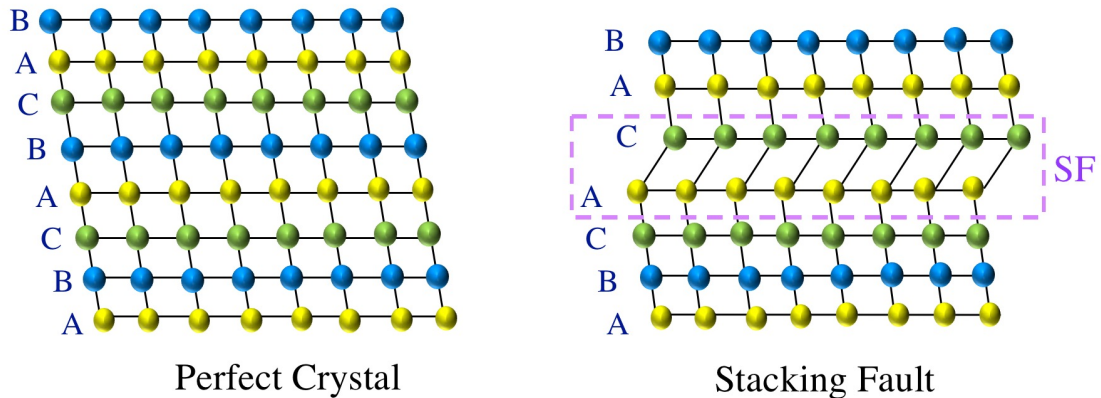


Figure 1.3: A perfect Face-Centered Cubic crystal layer stacking (left) versus structure with an interrupted stacking creating a SF (right).

They are not typically seen in ABABAB... sequence in body centered cubic (BCC) and face-centered cubic (FCC) structures since there's no alternative for an A layer adjacent to a B layer, unlike close-packed planes with an ABCABC... sequence, where

it's possible for an A layer to equally rest on a B or a C position.

There are two types of SFs in FCC structures: Intrinsic and extrinsic SFs. An intrinsic SF occurs due to the lack of an atomic layer in the stacking sequence, similar to the case depicted in Figure 1.3 where a layer B is clearly missing compared to the sequence of the perfect crystal. In contrast, an extrinsic SF is an extra layer introduced within the regular sequence, for example, an extra A layer is introduced between a B and a C layer.

Since SFs are imperfections, they are associated with an energetic cost called the stacking fault energy (SFE). In fact, a SF is the product of a full dislocation dissociating into two partial dislocations: a leading one and a trailing one. The dissociation of a full dislocation depends on energy considerations as it's energetically more favorable [45].

Following dissociation, the partial dislocations repel each other. As the partials separate, the SF grows until the equilibrium spacing is reached when the net repulsive force (per unit length) of the two partials equals the SFE. Hence, if the SFE is low, the partials are widely separated; conversely, if the SFE is high, dislocation dissociation doesn't occur and slip dislocation will be a full dislocation.

This characteristic related to SFs reflects on the mechanical properties and behavior of materials since it's crucial to certain deformation mechanisms, as will be discussed in the next paragraph.

SFs in Metals and Alloys

Unlike materials with pre-existing TBs and GBs, the effect of pre-existing SFs on deformation mechanisms as well as strength and ductility is yet to be explored. In single crystal metals and alloys, several studies reckon them as defects that form during deformation in metals and alloys [47, 48, 49, 71, 72, 73, 74, 75, 76] and focus on their contribution to plastic deformation but their effects on the deformation

mechanisms themselves are still unclear.

Yet, many studies have looked at the effects of pre-existing SFs on triggering alternative deformation mechanisms instead of the classical dislocation slip, that improve strength and ductility, mainly in HCP structures known for their brittle behavior due to the lack of slip systems. In fact, Taylor [77] following Von Mises [78] proved that a general homogeneous deformation without cracks in polycrystalline materials requires five independent slip systems. In HCP crystals, the two favorable Burgers vectors are \mathbf{a} and $\mathbf{c}+\mathbf{a}$ and the possible slip systems are shown in Figure 1.4.

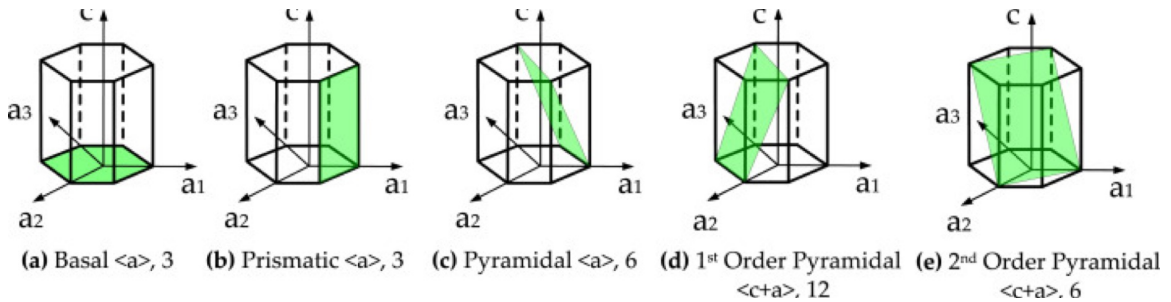


Figure 1.4: Slip systems in an HCP single crystal [3].

The most common basal and pyramidal slip systems in HCP materials offer only four independent modes which are insufficient to fulfill the Von Mises requirement generally compromising their ductility compared to FCC metals.

Some HCP metals and alloys exhibit a better ductility under mechanical loading thanks to alternative deformation mechanisms. Specifically, in HCP metals and alloys with low SFE, pre-existing basal SFs seem to play an important role in defining their deformation mechanisms. For instance, α -Ti with pre-existing equally spaced SFs on its basal planes has a better yield and flow stress than the single crystal case in compressive loading [79]. In fact, an FCC phase nucleating by the process of continuous slip of dislocations on adjacent planes is observed. However, pre-existing basal SFs serve as a barrier for propagation of the FCC phase, which contributes to the increase of the yield stress and a generally harder stress-strain behavior compared

to SF-free Ti nanopillars.

The distance separating pre-existing SFs also affects the mechanical behavior of HCP materials. Song and Li [80] found an optimal spacing for which the strength and ductility are maximized by running *c*-axis compression atomistic simulations on Mg nanopillars. This results from the repulsive forces exerted by the SF on dislocations that hinder the nucleation and glide of dislocations which in turn results in a high yield strength. In the work afore-mentioned [80], they suggest that when the SF spacing is small, the pillars exhibit hardening due to the lack of dislocation movement in the confined space between the pre-existing SFs. To carry plasticity, the sample resorts to an alternate deformation mechanism and results in the nucleation of a new grain with a 90° angle rotation with respect to the basal plane of the original grain. These two examples present alternative deformation mechanisms for HCP metals with pre-existing basal SFs, preventing slip on other planes, further compromising ductility.

Previous studies focused on the plastic behavior of metals detail the interactions between SFs and other types of defects, which play, later on, a significant role in the mechanical deformation of these materials. In Wei and Wei [81], the impingement of screw dislocations on intrinsic and extrinsic SFs in FCC metals such as Al, Au, Ni, Cu and Ag is investigated. According to Wei and Wei [81], when a screw dislocation encounters an intrinsic SF, the latter either (1) transforms to an extrinsic SF by the dissociation of the screw dislocation into Shockley partials and their glide on a plane parallel to the SF, (2) is annihilated when the two Shockley partials glide along the SF or (3) is penetrated by the screw dislocation that glides on a slightly shifted slip plane relative to its former slip plane.

On the other hand, three other modes of interaction are possible in the case of an extrinsic SF. In fact, the screw dislocation can dissociate into two Shockley partials that propagate between the two planes of the extrinsic SF adding a third plane that transforms the extrinsic SF into a three-layer twin. It can also transform into an

intrinsic SF if the two Shockley partials propagate near one of the two planes of the initial extrinsic SF. The last mode of interaction is penetration of the extrinsic SF by the screw dislocation and its glide on a slightly shifted slip plane. It is the stacking fault energy of the different metals that favors one of these modes against others.

In other FCC materials, stacking fault tetrahedra (SFT), a cluster of vacancies generated by an intersection of SFs in multiple slip planes forming a tetrahedron, are often observed in quenched or irradiated metals and alloys. Zhang et al. [82] report that the compressive stress can truncate the SFT and initiate their destruction by transforming faulted Frank loops to full dislocation loops. In Wang et al. [83], SFT in gold nanocrystals are prone to annihilation by dislocations in the confined volume of nanocrystals. The confined volume that decreases the distance between SFT and the TBs constituting a nucleation site for Shockley partials facilitates the annihilation process.

In low SFE steel [84], partial dislocations nucleating from GBs at initial stages of plasticity propagate through the grains creating a complex SF network with SFs nucleating on intersecting planes obstructing the propagation of each other. Plasticity is carried, in this case, by the high density of these extended dislocations.

In metals and alloys, as mentioned earlier, the SFE plays an important role in favoring certain deformation mechanisms over others. For instance, the SFE of Cu (~ 78 mJ/m²) decreases by more than an order of amplitude when alloyed with Al (6 wt pct Al, SFE ~ 6 mJ/m²) [85]. It's well established that twinning and dislocation slip are two major and competing modes of plastic deformation in metals and alloys. In Cu-Al alloys [85], it is proven that higher SFE leads to a smaller spacing between partials and therefore, a higher tendency for cross-slip. On the other hand, lower SFE stemming from alloying Cu with Al results in a higher probability for SFs and twins to form, which results in work-hardening at late stages of deformation. In addition, nanocrystalline Cu-Al alloys exhibit a higher yield strength and lower

uniform elongation than nanocrystalline pure Cu under tensile deformation, thanks to their lower SFE energy [86]. This effect is also observed in Ni-Co alloys, where Co reduces the SFE, ensuring a higher strength and tensile ductility [87]. Since lower SFE leads to an improvement in strength and ductility, alloying is often looked into as a way to lower the SFE of metals and achieve better mechanical properties [88, 89, 90, 91].

1.1.3 Layer Interfaces in Metallic Multilayers

Nanostructured metallic multilayers (NMMs) consisting of alternating layers of metals gained interest over the last years owing to their outstanding mechanical and magnetic properties as well as their radiation tolerance making them good candidates for a variety of potential applications in industry [50, 92, 93, 94, 95, 96, 97, 98, 99, 100, 101].

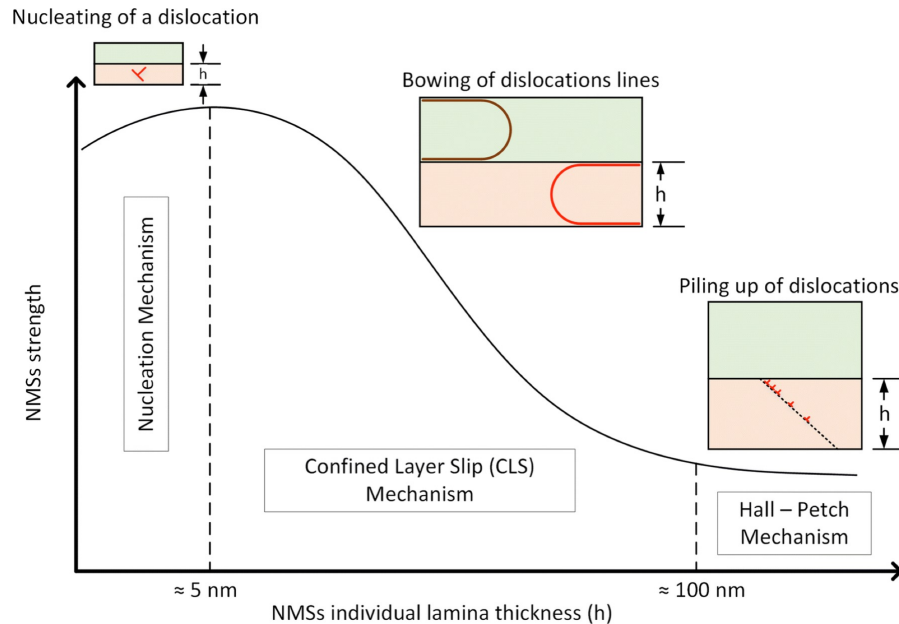


Figure 1.5: The strength vs individual layer thickness for NMMs [4].

In terms of mechanical properties, it has been established that under certain circumstances, yield strengths of NMMs exceed those of the bulk crystalline forms of

either one of the single metallic components of the multilayers. This enhancement has been the subject of multiple studies in literature [102, 103, 104].

Layer thickness plays an important role in setting the deformation mechanisms that NMMs follow. At a layer thickness greater than 50 nm, dislocation pile-up against the layer interfaces following the Hall-Petch relationship [105] is the most commonly observed deformation mechanism. According to this model, dislocations accumulate at layer interfaces until the applied stress and the stress concentration due to the pile-up surpass the barrier strength and transmit slip across the boundary. When the thickness varies in the range of 5-50 nm, confined layer slip (CLS) governs the deformation of NMMs and the yield strength as a function of the layer thickness follows the Orowan model, where slip may occur by bowing of dislocations between interfaces rather than pile-up formation. At a smaller size of ~ 5 nm, NMMs exhibit hardening and as the thickness gets smaller (1 nm lengthscale), softening is observed due to slip across the layer interface (Figure 1.5).

Nevertheless, layer thickness is not an exclusive factor in determining the deformation mechanisms in metallic multilayers. Another important aspect that plays a significant role in the deformation process is the nature of the layer interface separating the two materials, whether coherent or incoherent.

In fact, there can be three types of layer interfaces. The first one is the coherent interface which separates two crystals that match perfectly at the interface plane so that the two lattices are continuous across it. This can only exist if the interfacial plane has the same atomic configuration in both phases, which might require the two crystals to be oriented in a specific way relative to each other. However, the strains associated with such an interface increase the total energy of the system. In this case, it's energetically more favorable for interfaces to arrange in a semi-coherent manner, where the mismatch is compensated by misfit dislocations. The last type of interfaces is the incoherent interface; it forms when the interface plane has a very

different atomic configuration in the two adjacent layers and there is no possibility of good matching across the interface. It can either stem from very different atom patterns such as an FCC and an HCP adjacent layers or interatomic distances that differ by more than 25%.

Depending on the nature of the interface, NMMs can exhibit deformation mechanisms that are different from those discussed above. Indeed, in Cu/Nb multilayers with FCC-BCC interfaces, the interface barrier stress for slip transmission in the absence of dislocation pile-up, depends on how strongly a glide dislocation interacts with the interface, which depends on the nature of the interface among other factors [95]. An incoherent interface in Cu-Nb systems is a strong barrier to dislocation transmission and prohibits their slip from one layer to the other even with a small layer thickness (< 5 nm) where dislocation transmission through the interface is usually observed. In other systems such as Cu/Ni and Cu/Ni/Nb, interfacial defect configurations significantly alter the strength and mechanical behavior of the material [106]. In general, depending on the nature of the interface and the stresses attributed to it, it can act as a strong barrier for dislocation propagation, inducing strengthening [107, 108, 109, 110] and promoting alternative deformation mechanisms [111, 112, 113, 114, 115].

1.2 Computational Modeling

Physical phenomena can be examined by experimental methods, computational modeling and theoretical analysis. When it comes to the properties of materials, it's known that they depend on a variety of processes and mechanisms occurring at a large range of length scales. Computer simulations in particular are a great means to providing atomistic insights, that are not possible by experimental methods, to a variety of phenomena and systems. Indeed, computational modeling allows

us to understand continuum-level processes in depth by revealing the evolution of the microstructure through them. Although advances in technology currently allow experimental studies at the nanoscale, computational techniques provide a predictive tool for understanding the microstructure, particularly for nanostructured materials, often lowering the cost compared to experimental methods. At the atomic scale, defects such as GBs, TBs or SFs, their structure, their nucleation and growth mechanisms and the interactions between them have a significant role in defining the mechanical properties at the engineering scale. Therefore, atomistic simulations complement experimental findings to provide a broad and deep knowledge of the atomistic underpinnings of physical phenomena that may span several time and length scales.

Molecular Dynamics (MD) method is commonly utilized to model mechanisms at the atomic length and timescale mechanisms. MD captures the trajectory of each atom in a system during deformation based on classical mechanics, that is, by solving Newton's equations of motion. The interaction forces between the atoms are modeled by interatomic potentials which are empirically obtained by fitting to experimental data or quantum mechanical calculations.

Although MD simulations are widely used owing to their reliability and their low cost compared to several other methods, they have certain limitations like any model. MD simulations model the trajectories of each and every atom at each timestep, as well as their thermal excitation, therefore, as the system grows larger in terms of number of atoms, it becomes computationally expensive to run MD simulations and only systems upto a few hundred nanometers at most can be studied. In addition, the timestep is a small fraction of atomic vibrations, making 1 fs a typical timestep of MD simulations, resulting in very high strain rates of about $10^8 \sim 10^9$ /s which are not accessible experimentally. This timescale limitation prohibits direct comparison of MD simulations to experiments when modeling time-dependent or strain rate

dependent phenomena. Despite these restrictions, MD is one of the most popular methods for modeling material behavior with atomistic resolution and has successfully furnished valuable atomistic insights into response of materials at the nanoscale.

1.2.1 Fundamentals of Molecular Dynamics

The molecular dynamics method attempts to simulate the "true" dynamics of atoms in the context of Boltzmann's statistics. Molecular dynamics is simply the numerical integration of the classical equation of motion

$$m \frac{d^2 \mathbf{r}_i}{dt^2} = - \frac{\partial V(\{\mathbf{r}_i\})}{d\mathbf{r}_i}, \quad (1.2)$$

where \mathbf{r}_i is the position of atom i and $V(\{\mathbf{r}_i\})$ is the potential energy. This expression is equivalent to Newton's second law

$$\mathbf{f}_i = m \mathbf{a}_i, \quad (1.3)$$

where $\mathbf{f}_i = - \frac{\partial V(\{\mathbf{r}_i\})}{d\mathbf{r}_i}$ is the force on atom i and $\mathbf{a}_i = \frac{d^2 \mathbf{r}_i}{dt^2}$ is its acceleration.

Time integration of this system of equations with proper initial positions and velocities provides trajectories of all atoms as a function of time. The Verlet algorithm is one of the simplest and most stable algorithms used to determine the positions and velocities of all atoms at a specific timestep.

Velocity Verlet Algorithm By the Verlet algorithm, the updated positions and velocities are obtained as follows:

$$\mathbf{r}_i(t + \Delta t) = \mathbf{r}_i(t) + \mathbf{v}_i \Delta t + \mathbf{a}_i(t) \frac{\Delta t^2}{2}, \quad (1.4)$$

$$\mathbf{a}_i(t + \Delta t) = - \frac{1}{m} \frac{\partial V(\{\mathbf{r}_i(t + \Delta t)\})}{d\mathbf{r}_i(t + \Delta t)}, \quad (1.5)$$

and

$$\mathbf{v}_i(t + \Delta t) = \mathbf{v}_i(t) + [\mathbf{a}_i(t) + \mathbf{a}_i(t + \Delta t)] \frac{\Delta t}{2}, \quad (1.6)$$

with initial conditions $\{\mathbf{r}_i(0)\}, \{\mathbf{v}_i(0)\}$.

Since Newton's equations of motion conserve the total energy, an integration scheme has to take this aspect into account. Over long time scales, the Verlet algorithm seems to preserve the energy quite accurately [116] allowing MD to capture macroscopic long time scale responses.

Embedded-Atom Method (EAM) Interatomic Potential Throughout the course of this dissertation, we detail MD simulations where inter-atomis interactions are based on the embedded-atom method (EAM) potential originally developed by Daw and Baskes [117]. It's usually used for metallic systems such as Cu, Al, steel... in which electrons are more diffuse and shared by many neighboring atoms.

This inter-atomic potential is based on the following form:

$$V = \sum_a F(\rho_a) + \frac{1}{2} \sum_a \sum_b \phi(r_{ab}), \quad (1.7)$$

with $F(\rho_a)$ being the embedding function of atom a that takes into account the effect of electron density, where ρ_a is the local density of electrons in the neighborhood of atom a and $\phi(r_{ab})$ being a pairwise potential that represents the interactions between atoms a and its neighbor b, function of the distance between them. The EAM potential considers interactions only up to second neighbors to ensure computational efficiency.

The EAM potential developed by Zhou et al. [97] used for the simulations presented in this dissertation has been tested for accuracy in modeling the mechanical and material properties of Cu and Co and compared to the EAM potential for Co only developed by Pun et al. [118] to verify that HCP and FCC Co properties match

those obtained by experimental data.

Energy Minimization A conjugate gradient (CG) minimization method is used at 0 K when the kinetic energy is absent to ensure a stable equilibrium of the system at the lowest potential energy possible. Although numerous algorithms have been developed to optimize the minimization process, the CG algorithm is utilized in MD simulations for its simplicity and efficiency [119]. The CG algorithm is an iterative algorithm for finding a local minimum more efficiently by updating the search direction to be conjugate to the previous one.

Nose-Hoover Thermostat This type of thermostat is used in our MD simulations during the equilibration process that aims at bringing the system to a steady state by stabilizing the temperature. It mimics the heat exchange between the simulation volume and its surroundings. This heat bath exchanges heat with the atomic subsystem by scaling the atoms velocities.

1.2.2 Visualization

Visualization of MD simulations results is performed using Ovito [120]. To study the defect structures, a filtering method that will differentiate atoms in their perfect structures from those occupying defect positions is required. Common neighbor analysis [121] is used in the studies presented in this dissertation to determine the local atomic structure, therefore, defects. For example, in an FCC structure, atoms of a stacking fault occupy the sites of an HCP lattice, thus, when applying the common neighbor analysis, they will have a different common neighbor parameter than other atoms in the structure.

To identify dislocations and partial dislocations, Ovito provides a dislocation analysis tool called the Dislocation Extraction Algorithm (DXA) [120]. This tool identifies all dislocation line defects in an atomistic crystal, determines their Burgers

vectors, and outputs a line representation of the dislocations. It's a very useful tool in identifying the types and characteristics of dislocations as they play a significant role in the deformation mechanisms during plasticity, which allows a close examination of their evolution during mechanical deformation.

1.3 Dissertation Outline

This dissertation consists of six chapters. Chapter 1 is an introduction that provides a definition of the main concepts mentioned throughout the dissertation as well as an overview of the methods used. It also presents a review of the literature that focuses on studying the properties of nanostructured metallic multilayers and the role of different planar defects and interfaces in defining the mechanical behavior of metals through experiments as well as computational and theoretical modeling. In Chapter 2, we investigate the plastic deformation of HCP Co with pre-existing high density SFs on its basal planes. The deformation mechanism dominated by phase transformation is investigated. Chapter 3 provides insights into the orientation-dependent deformation mechanisms of Cu/Co multilayers. In this chapter, we link the different nanostructures as well as pre-existing defects and layer interfaces emanating from the different crystal orientations to deformation mechanisms observed in Cu/Co multilayers. Chapter 4 extends the analysis of FCC Cu/HCP Co studied in Chapter 3 by looking into the three planar defects present in the system: TBs, SFs and incoherent layer interfaces. We focus on the individual effect of each of the pre-existing planar defects (TBs, SFs, incoherent layer interfaces), as well as their density on the mechanical response of the multilayers, since experiments reveal that varying the layer thickness of such a system alters the nature and the density of the pre-existing defects. Chapter 5 is a study of the alternating hardening and softening mechanisms dominated by SFs and their interactions in FCC Co nanopillars. We also

examine strain rate effects on the density of SFs, hence the deformation mechanisms. Finally, Chapter 6 concludes this dissertation by summarizing the main findings of the work and presenting some avenues for future studies.

We wish to note that the experimental studies detailed throughout this dissertation were performed by our collaborators, therefore, we will only mention some of the main results that support the hypotheses and conclusions discussed in the following chapters.

Chapter 2

PHASE TRANSFORMATION INDUCED PLASTICITY IN HEXAGONAL CLOSE PACKED CO WITH STACKING FAULTS

2.1 Introduction

Cobalt (Co) and its alloys have various applications in high strength structural materials, magnetic devices as well as corrosion and wear resistant coatings [122, 123, 124, 125, 126]. At room temperature, Co has a stable hexagonal close-packed (HCP) structure and a small fraction of metastable face centered cubic (FCC) structure due to the low stacking fault energy (SFE) of HCP Co, 31 mJ/m^2 [127]. Planar defects such as twin boundaries (TBs) and stacking faults (SFs) have been previously studied in FCC metals[2, 21, 22, 24, 92, 94, 128, 129, 130, 131, 132, 133, 134, 135, 136, 137, 138, 139, 140, 141, 142, 143, 144, 145, 146, 147, 148, 149]. It has been shown that TBs and SFs can strengthen FCC metals by blocking the transmission of

dislocations. Meanwhile, there are numerous studies that show partial dislocation-planar defect interactions and detwinning could also provide mobile dislocations and thus, improve the ductility [38, 68, 136, 144, 150, 151, 152, 153]. However, there are few studies on deformation mechanisms of HCP metals with pre-existing SFs. It has been reported that high density SFs in Mg alloy can increase yield strength by impeding the movement of dislocations [154].

HCP metals are generally less ductile than FCC metals due to insufficient number of independent slip systems, which does not satisfy the Von Mises criterion [155, 156]. Another deformation mechanism for HCP metals - deformation twinning - can also accommodate plastic deformation and contribute to tensile ductility [157, 158, 159, 160, 161]. However, when grain size is under 100 nm, deformation twinning is often rarely observed in HCP metals [162], resulting in poor plasticity. Thus, it is very challenging to enhance the plasticity of nanocrystalline HCP metals.

In this chapter, we report on molecular dynamics (MD) simulations of compression on HCP Co (0002). The stress-strain behavior has a high yield strength followed by a sharp decrease in stress. A closer examination of the structure evolution shows that the high strength and deformability originate primarily from HCP to FCC phase transformation. Micropillar compression studies on mechanical behavior of HCP Co (0002) with high density parallel SFs on basal planes also reveal a high yield strength, ~ 1.1 GPa, followed by prominent work hardening to a flow stress of 2.0 GPa, up to $\sim 20\%$ strain. Post deformation transmission electron microscopy (TEM) analysis shows HCP-to-FCC phase transformation that promotes plasticity. This study provides a fresh perspective, that is, phase transformation can be a major deformation mechanism in HCP metals for imparting high strength and plasticity.

2.2 Experimental and Computational Methods

2.2.1 Simulation Method

Molecular dynamics simulations were performed on HCP Co nanopillars by using the Large-scale Atomic/Molecular Massively Parallel Simulator (LAMMPS)[163] and the results were visualized using Ovito [164] and DXA [120], the dislocation analysis tool. The digital HCP Co pillars were 4 nm in diameter and 8 nm in height and contained stacking faults on the (0002) planes. These stacking faults with an average spacing of 1.6 nm were introduced by applying rigid body motion on the (0002) planes along the $\langle 10\bar{1}0 \rangle$ direction. Specifically, the layers were held fixed and one rigid block was moved relatively to the other on the (0002) planes in the $\langle 10\bar{1}0 \rangle$ direction. Then, the entire sample was allowed to relax. First, the pillar was equilibrated at 0 K using the conjugate gradient energy minimization. Subsequently, the sample was equilibrated at 300 K under the NVT ensemble with a Nose-Hoover thermostat. Finally, compression was applied for 160 ps at a strain rate of $6.25 \times 10^8 s^{-1}$. The Co-Co atomic interactions are described by the embedded-atom method (EAM) potential developed by Zhou et al. [97].

2.2.2 Experimental Methods

2 μm thick Co films were deposited on Si (110) substrates with 100 nm Cu seed layers at a deposition rate of ~ 0.35 nm/s for Co. In situ micropillar compression tests were performed in a scanning electron microscope (SEM). HCP Co pillars with ~ 1 μm in diameter and ~ 2 μm in height were fabricated using the same SEM microscope equipped with focused-ion-beam (FIB). Additional details can be found in [165].

2.3 Computational Results

MD simulations were performed on HCP Co with SFs on basal planes to investigate the atomistic deformation mechanisms and detailed phase transformation process during nanopillar compression. The stress-strain curve shows a high yield strength of ~ 12 GPa followed by sharp stress reduction to ~ 1.8 GPa after yielding (Figure 2.1(a)).

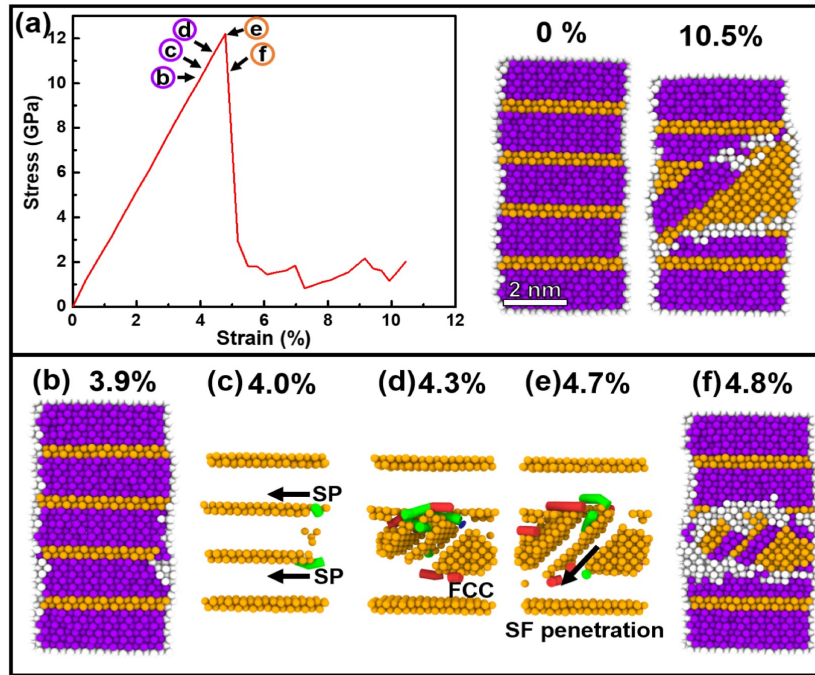


Figure 2.1: MD simulations of compression of HCP Co pillar with parallel SFs. Atoms are in common neighbor color coding (orange for FCC, purple for HCP and white for unidentified structures). Green and red lines represent Shockley partials and red lines represent other dislocations, respectively.

Prior to yielding, at about 4% strain, two Shockley partials (green lines) are nucleated at the intersection of the horizontal SFs and the pillar surface (Figure 2.1(c)). With increasing stress, the Shockley partials start to glide along the SF planes resulting in defaulting. Consequently, this partial annihilation of the pre-existing SFs creates space for the FCC Co phase to nucleate and propagate. We have visualized

the evolution of the microstructure using the local Von Mises shear strain in Figure 2.2, which highlights the concentration of local large shear strains around the areas of HCP-to-FCC phase transformation. Figure 2.1(d) shows that, after a patch of FCC Co is formed, Shockley partials nucleate from the interface between the HCP and FCC phases and glide on FCC (111) planes forming SFs in the FCC phase, leading to plastic yielding accompanied by a major stress drop (Figure 2.1(e)). Stair rod dislocations with Burgers vector of $1/6 [110]$ (red lines) also form at the interception of the inclined SFs by the pre-existing horizontal SFs, which prevent the propagation of partial dislocations and may contribute to work hardening. the crystallographic orientation relation between HCP and FCC Co revealed by MD simulations is in good agreement with the HRTEM analyses presented later in this chapter (Figure 2.5(c-d)). It is worth mentioning that Burgers reported a HCP-to-FCC phase transformation mechanism in Zr that is to some extent similar to what MD simulations show in the present study [166].

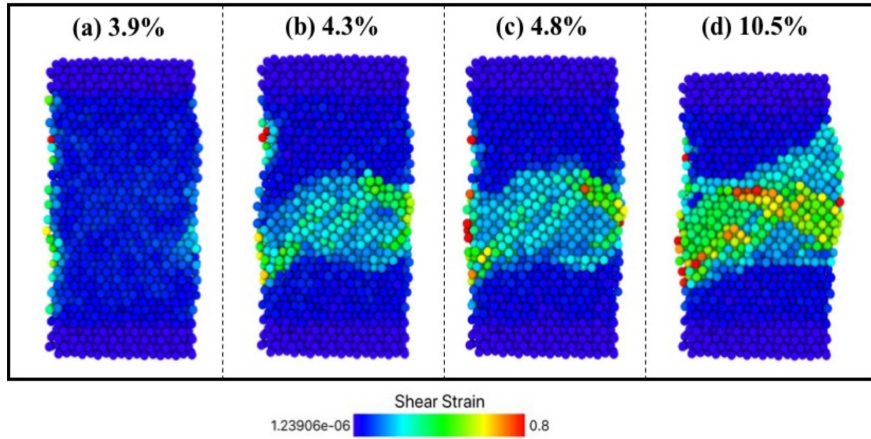


Figure 2.2: MD simulations of compression tests of HCP Co pillar with parallel SFs. Coloring of atoms is according to the Von Mises shear strain for various configurations during deformation.

Another MD simulation of compression of HCP Co without basal plane SFs was

also performed (Figure 2.3). MD simulations show that basal slip and prismatic slip dominate the plastic deformation. These observations indicate that basal SFs are critical in inhibiting dislocation glide in HCP Co and consequently, SFs can strengthen the materials.

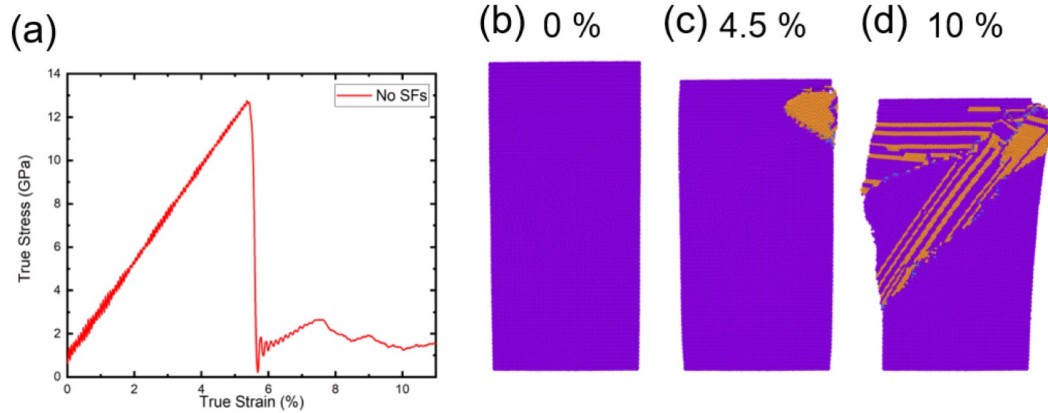


Figure 2.3: MD simulations of compression tests of HCP Co pillar without SFs. Atoms are in common neighbor color coding where orange, purple and white denote FCC, HCP and unidentified structures, respectively.

2.4 Experimental Results

Mechanical behavior of epitaxial HCP Co (0002) was also studied by in situ SEM pillar compression testing. Figure 2.4(a) shows the true stress-strain curves. Pillars yield at ~ 1.2 GPa and show a prominent work hardening capability to a peak stress of ~ 2 GPa. The work hardening exponent is calculated as $n \simeq 0.55$. Figures 2.4(b)-(e) show SEM snapshots of the HCP Co pillar (presented by the red stress-strain curve) during compression. The HCP Co pillar experiences a uniform deformation without forming any voids or cracks up to 20% strain, an indication of prominent plasticity.

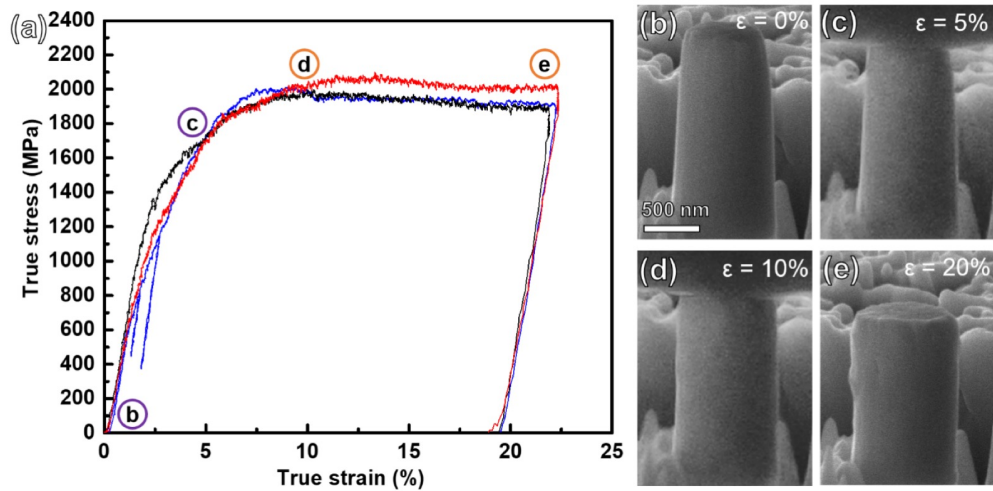


Figure 2.4: In situ micropillar compression tests on HCP Co. (a) True stress-strain curves. (b-e) SEM snapshots of an HCP Co pillar showing uniform deformation during compression. No cracks were observed.

Figure 2.5 shows TEM micrographs of the deformed HCP Co pillar. Figure 2.5(a) confirms that no slip bands or cracks formed during deformation. The deformation induced dilation near the pillar top. The SAD in Figure 2.5(a) reveals two sets of diffraction patterns, associated with HCP (red lines) and FCC (blue lines) Co, respectively. Higher magnification TEM micrographs in Figure 2.5(b) show multiple sets of inclined SFs. HRTEM micrographs in Figure 2.5(c)-(d) show the phase boundaries between FCC and HCP Co as decorated by white dashed lines. In FCC Co, the high-density of inclined SFs are along (111) planes as determined by the inserted FFTs. Note that the (0002) planes in HCP Co are nearly parallel to the (111) planes in FCC Co (Figure 2.5(c)), similar to the orientation relation observed in MD simulations. The FCC Co phase shown in Figure 2.5(d) is distorted due to plastic deformation.

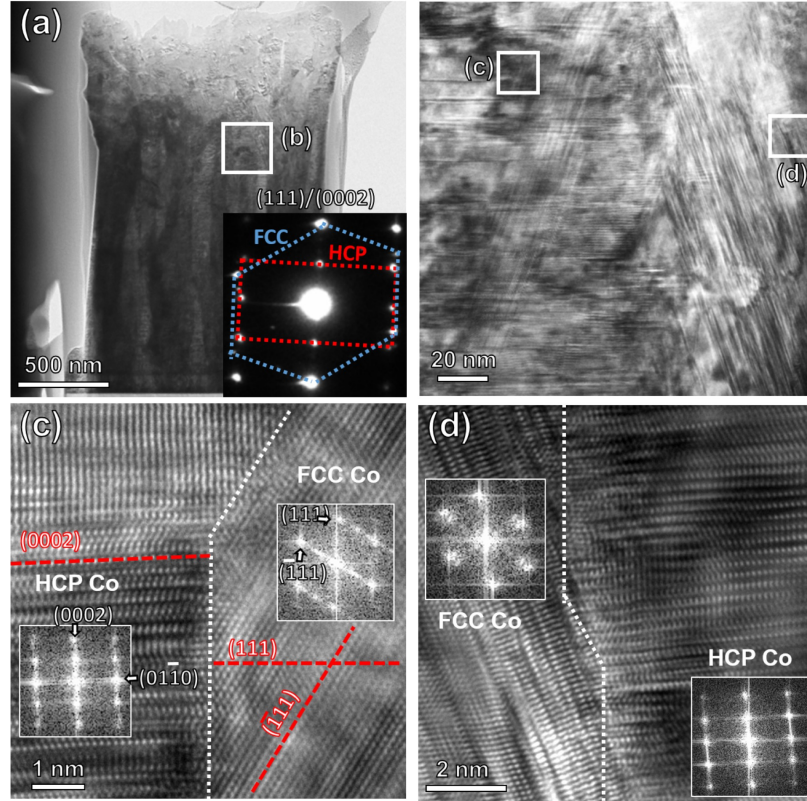


Figure 2.5: Cross-section TEM micrographs of an HCP Co pillar deformed to $\sim 20\%$ true strain. (a) A TEM micrograph at low magnification. (b) A higher magnification TEM micrograph of the box (in a). (c,d) HRTEM micrographs of the boxes in (b).

2.5 Discussion

Deformation modes in HCP metals have been extensively studied. At room temperature, dislocation glide and deformation twinning are two principal deformation mechanisms in HCP metals. For dislocation glide, $\langle a \rangle$ type dislocation $[11\bar{2}0]$ gliding on basal or prismatic plane is one of the most common slip systems in HCP metals [167]. However, in this study, HCP Co has (0002) out-of-plane texture, which means the Schmid factors for $\langle a \rangle$ type dislocations on both basal and prismatic planes would be very small (close to 0), therefore, neither the basal nor the prismatic slip would be the prominent deformation mechanism. Another major dislocation,

$\langle c+a \rangle$ type dislocation with Burgers vector of $[11\bar{2}3]$, can glide on pyramidal planes and accommodate plastic strain along the c direction [167]. However, the pyramidal slip of $\langle c+a \rangle$ type of dislocations is largely prohibited by the high-density of SFs on basal plane [154].

Deformation twinning is another fundamental deformation mechanism in HCP metals in addition to their limited slip systems [157, 158, 159, 160, 161]. However, deformation twinning is not observed in MD simulations and is largely absent in the TEM micrographs of the deformed HCP Co pillar. Prior studies show that when the grain size is less than 100 nm, deformation twinning may be easier to operate in FCC metals [162, 168, 169, 170], but becomes much more difficult in HCP metals, except under severe plastic deformation [171] or by adding an alloying element [172]. Since the grain size of HCP Co in this study is ~ 50 nm and the MD simulations are performed at the nanoscale, deformation twinning is also largely inhibited during deformation.

If the classical dislocation glide and deformation twinning mechanisms are both prohibited in HCP Co with high-density SFs, then how do we explain the deformation mechanisms and work hardening capability observed in the current study? MD simulations (Figure 2.1(f)) and Post compression TEM micrographs (Figure 2.5) show the coexistence of both the HCP and the FCC phase in the deformed pillar. As FCC Co was not observed in the as-deposited Co and the MD sample is solely HCP, the FCC phase should have formed during deformation, which may be triggered by high local stresses [173, 174, 175]. TEM micrographs (Figure 2.5(c)-(d)) show that FCC Co is formed on two sets of inclined (111) planes relative to the horizontal HCP (0002) basal planes. Furthermore, high-density inclined SFs along (111) planes in FCC Co are also observed (Figure 2.5(b)) due to the migration of Shockley partial dislocations along the inclined (111) planes. Thus, phase transformation and partial dislocation activity in the FCC Co phase may contribute to the significant plasticity

during compression of HCP Co.

2.6 Conclusion

We report an intriguing deformation mechanism in HCP Co dominated by phase transformation. Epitaxial HCP Co thin films with high density SFs exhibit simultaneous high strength and plasticity as revealed by in situ SEM compression tests. Post deformation TEM analysis shows the formation of an FCC Co phase during compression. MD simulations elucidate that the HCP-to-FCC phase transformation arises from partial dislocations gliding along the pre-existing SFs parallel to the basal plane during compression. The subsequent generation of inclined SFs on (111) planes in FCC Co plays a key role in accommodating plasticity. This study provides a new perspective for designing high-strength deformable HCP metals by introducing a high density of SFs.

Chapter 3

ORIENTATION-DEPENDENT MECHANICAL RESPONSE OF CU-CO MULTILAYERS

3.1 Introduction

Nanostructured metallic multilayers have drawn significant attention because of their high strength, good wear resistance, resilient radiation tolerance, and intriguing magnetic properties for a variety of potential applications in industry [50, 92, 93, 94, 95, 96, 97, 98, 99, 100, 101]. In terms of mechanical properties, previous studies have mostly focused on the layer thickness (h) and layer interface dependent strengthening and deformation mechanisms in different systems, such as FCC/FCC [92, 101, 176, 177, 178, 179, 180], FCC/HCP [50, 96, 181, 182], FCC/BCC [96, 99, 101, 182, 183, 184, 185, 186, 187], HCP/HCP [188], HCP/BCC [189, 190], metal/ceramic [191, 192, 193] and metal/amorphous [93, 194, 195, 196] multilayers, where FCC, BCC and HCP stand for face-center cubic, body-center cubic and hexagonal close packed crystal structures.

In general, coherent interfaces, such as those in Cu/Ni, are weak barriers to transmission of dislocations [101, 176]; whereas incoherent interfaces, such as those in Cu/Nb, are stronger dislocation barriers due to slip discontinuity [96, 99, 101]. Nanostructured metallic multilayers are known for their high strength, testified by nanoindentation [50, 176, 178, 179, 183] and micropillar compression [93, 181, 184, 188, 192, 197, 198, 199] studies. However, most high strength multilayers show shear instability under compression (formation of slip band or crack) [99, 180, 182, 184, 186, 187, 190, 193, 200]. There are abundant studies on the extrinsic (pillar diameter d) and intrinsic (layer thickness h) size effects on toughening in metallic multilayers. These studies show that by increasing d or h , multilayer pillars show more 'ductile' (uniform deformation or barreling) deformation mechanisms, but doing so also leads to softening. However, there are few studies that focus on the influence of texture and layer interface on the strength and deformability of multilayers with chemically identical layer constituents and layer thickness.

In this chapter, we detail the results obtained by MD simulations of compression on Cu/Co multilayers with three different crystallographic orientations, $\{100\}$, $\{110\}$ and FCC $\{111\}$ /HCP $\{0002\}$ having significantly different layer interfaces. The simulations reveal that the semicoherent $\{100\}$ and $\{110\}$ layer interfaces have low resistance to the transmission of partial dislocations; whereas $\{111\}$ textured Cu/Co nanolayer has a defect network consisting of TBs in FCC Cu, stacking faults (SFs) in HCP Co, and the incoherent layer interface, thus, offering superior strength by prohibiting the propagation of partials. In situ compression tests performed on 25 nm Cu/Co multilayers with the same orientations used in MD simulations reveal a surprisingly high yield strength of $\{111\}$ textured multilayers, exceeding 2.4 GPa, compared to ~ 600 MPa yield strength for both $\{100\}$ and $\{110\}$ textured multilayers.

In fact, the high deformability of FCC $\{111\}$ /HCP $\{0002\}$ multilayers results from detwinning and HCP-to-FCC Co phase transformation induced softening. The

experimental sample with the same orientation undergoes a superelastic deformation of its cap layer observed post compression, due to the high deformability. This study provides an important concept, that is tailoring the network of planar defects can lead to the design of ultra-high strength, deformable nanocomposites for a variety of industrial and defense applications.

3.2 Computational and Experimental Methods

3.2.1 Computational Methods

Three cylindrical nanopillars of Cu/Co multilayers with $\{100\}$, $\{110\}$ and $\{111\}$ / $\{0002\}$ crystallographic structures, respectively, were studied by performing MD simulations using LAMMPS [163]. For FCC (100) and (110) pillars, the thickness of each layer is 5.3 nm, the total specimen height is about 32 nm and the diameter is about 19 nm. For Cu (111)/Co (0002) pillars, the thickness of each layer is 5 nm, the total specimen height is about 30 nm and the diameter is about 15 nm. Thus, the aspect ratio of the FCC pillars is about 1:1.7 and that of the FCC Cu/HCP Co pillar is 1:2. The simulations were performed at 300 K under the NVT canonical ensemble. The interactions between Cu and Co were modeled by the embedded-atom method (EAM) potential developed by Zhou et al. [97]. The potential was validated by calculating the elastic constants and the stacking fault energies for Cu as well as Co. The values were found to be in reasonable agreement with experimental results as well as simulations performed using another EAM potential for HCP and FCC Co developed by Mishin et al. [118]. Non-periodic boundary conditions were used in all directions. First, conjugate gradient energy minimization was performed, followed by equilibration of the specimens at 300 K. Then, the specimens were subjected to compression at a constant strain rate. The FCC (100) and (110) pillars were subjected to compression for 800 ps at a strain rate of $1.66 \times 10^8 s^{-1}$. Cu (111)/Co (0002)

pillars were subjected to compression for 900 ps at a strain rate of $1.86 \times 10^8 s^{-1}$. The HCP/FCC multilayer specimens were created layer by layer in order to introduce pre-existing coherent TBs (CTBs) in the FCC Cu layers and SFs in the Co layers parallel to the basal plane, to be consistent with the experimental specimens. The defect structures were visualized using OVITO [164] and the dislocation analysis tool DXA [120].

3.2.2 Experimental Methods

2 μm thick Cu/Co 25 nm multilayers were deposited on Si (100), Si (110) and Si (112) substrates with 100 nm Cu seed layers at deposition rates of ~ 0.5 nm/s for Cu and ~ 0.15 nm/s for Co. Then, Cu/Co multilayer pillars with ~ 1 μm in diameter and ~ 2 μm in height were fabricated using an SEM microscope equipped with focused-ion-beam (FIB), where compression is also performed.

3.3 Computational Results

MD simulation results for nanopillar compression of (100) and (110) Cu/Co 5 nm multilayers are performed to elucidate their deformation mechanisms. True stress-strain curves (Figure 3.1(a),(b)) reveal higher flow stress in FCC Cu/Co (110) nanopillar. For the FCC Cu/Co (100) nanopillar, Shockley partials transmit through the Cu/Co interface (Figure 3.1(c)) near the onset of yielding, leading to penetration of SFs across the interface (Figure 3.1(c)). A closeup of this process is detailed in the dislocation analysis Figure 3.2, where only defaulting atoms and dislocation lines are depicted, showing the penetration of a Shockley partial across the Cu-Co interface (Figure 3.2(a)). During plastic deformation, the glide of Shockley partials and subsequent propagation of SFs dominate the deformation, and slip bands form from the surface of the pillar as shown in Figure 3.1(d), a result of Shockley partials

exiting the outer surface (Figure 3.2(b)).

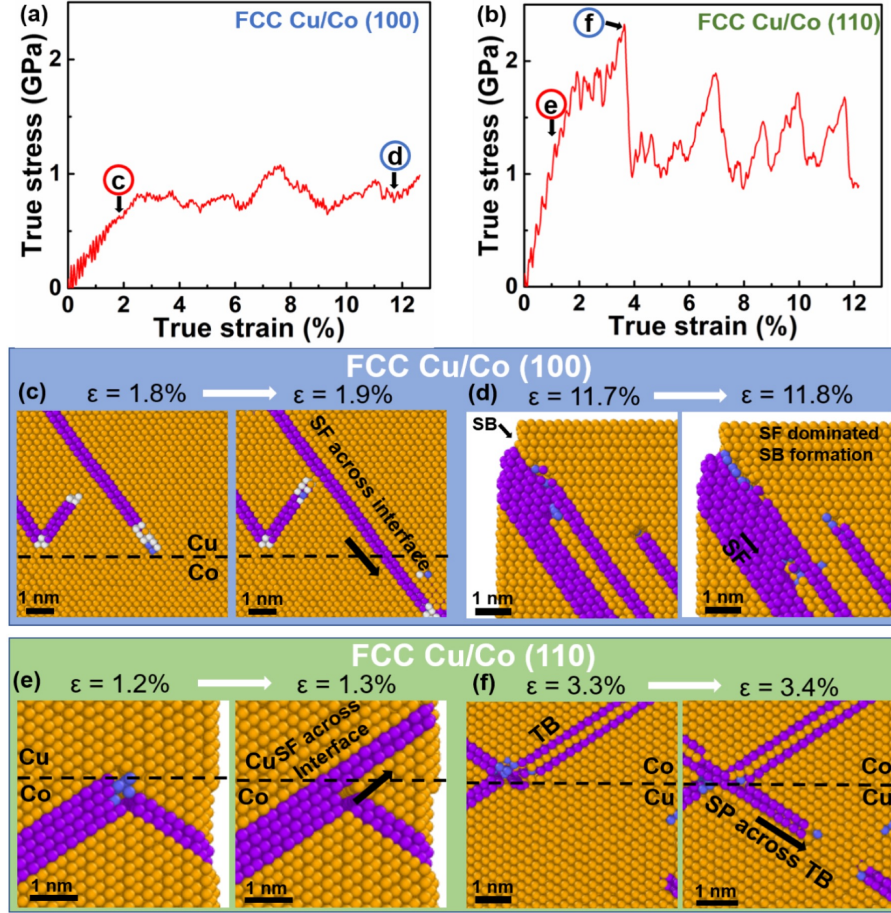


Figure 3.1: Comparison of MD simulation results for the FCC (100) and (110) Cu/Co 5 nm multilayer nanopillars. (a-b) Stress-strain curves. (c-f) Microstructure and dislocation analyses of FCC (100) and (110) multilayer at different levels of strain. orange, purple and white atoms are in FCC, HCP and unidentified structures, respectively.

Similarly, in the FCC Cu/Co (110) pillar, Shockley partials migrate easily across the Cu/Co interface, leading to plastic yielding (Figure 3.1(e)). Detailed view of this process is presented in Figure 3.2(c). Furthermore, CTBs formed in FCC (110) pillar during deformation, block the transmission of partials, and consequently contribute to work hardening (strengthening). The substantial softening (manifested as the stress drop in Figure 3.1(b)) arises from the transmission of Shockley partials across the CTBs as shown in Figure 3.1(f) and detailed in Figure 3.2(d). Although

the multilayers in MD simulations only have 5 nm individual layer thickness, these findings reveal that the coherent (100) and (110) FCC Cu/Co interfaces are weak dislocation barriers, and thus the strength and plasticity of these coherent systems are dominated by the glide and transmission of partial dislocations across layer interfaces.

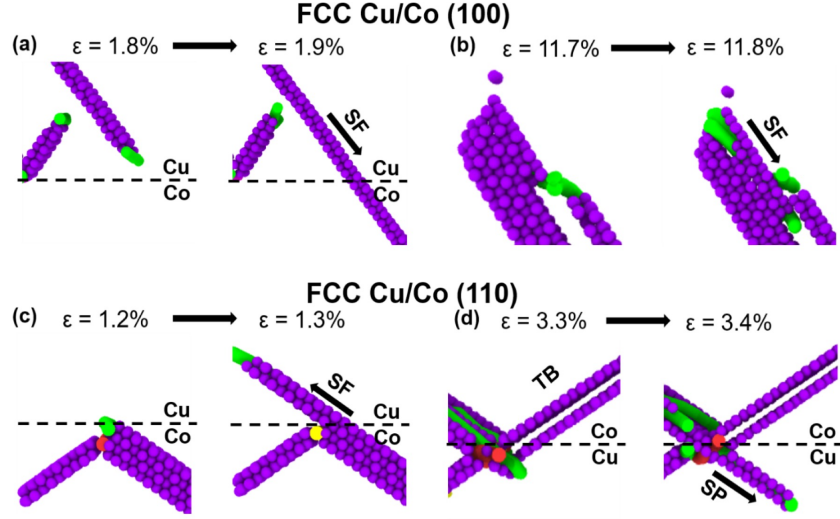


Figure 3.2: Dislocation analysis of the deformed FCC (100) and (110) Cu/Co 5 nm multilayer nanopillars during compression showing only defects. Green, yellow and blue lines denote Shockley partials, Hirth locks, and perfect dislocations, respectively. Red lines denote other dislocations.

MD simulations of compression on Cu (111)/Co (0002) multilayers with pre-existing nanotwins in Cu and SFs in Co (Figure 3.3(b)) were performed to reveal the atomistic mechanisms of high strength and significant plasticity. Briefly speaking, the horizontal coherent twin boundaries (CTBs) in Cu layers, SFs in HCP Co and incoherent layer interfaces all prohibit the penetration of dislocations, and thus the defect networks consisting of TB-SF-layer interfaces lead to ultra-high strength in Cu/Co nanolayers with FCC/HCP layer interfaces. The yield strength of the nanopillar is found to be ~ 5.5 GPa, much higher than that of the two simulated FCC Cu/Co multilayers.

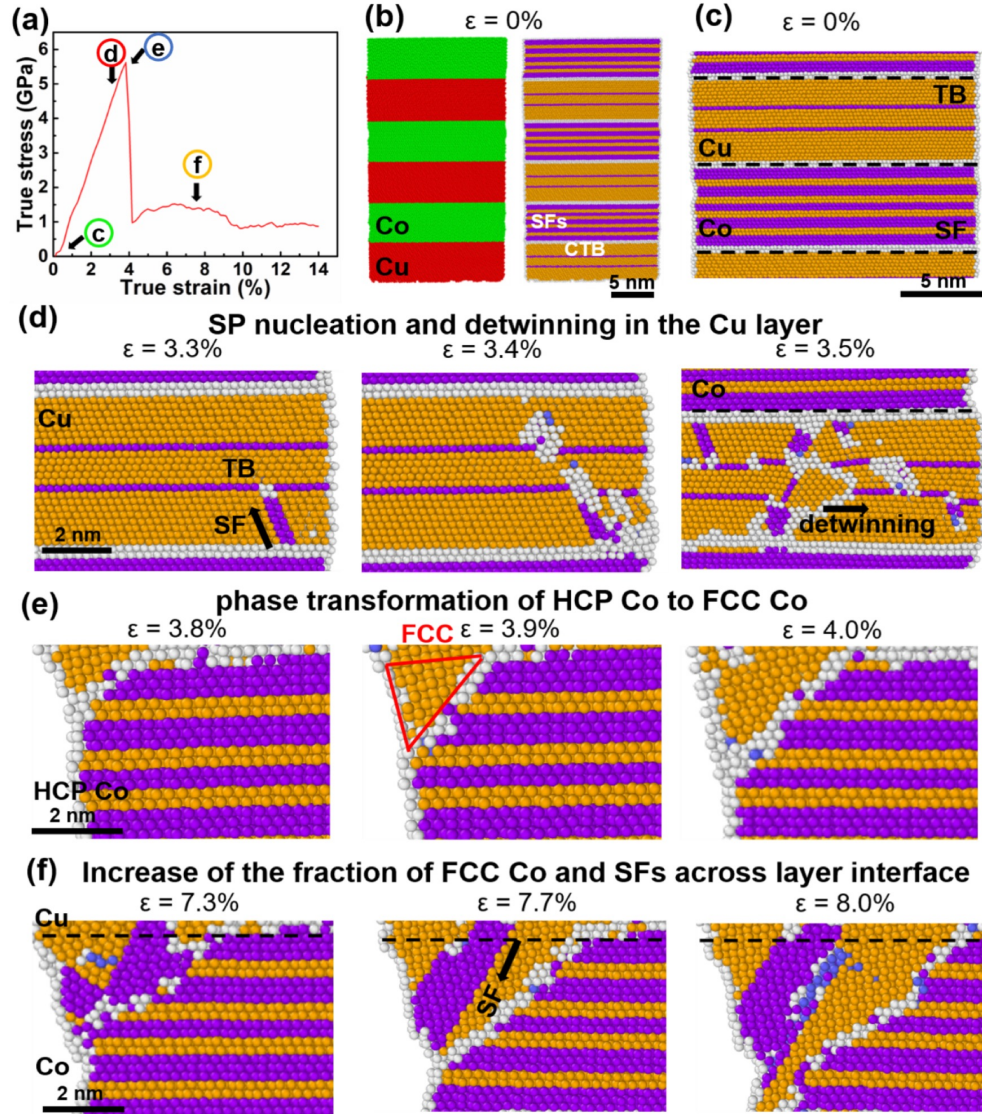


Figure 3.3: MD simulation results for the compression of FCC Cu (111)/ HCP Co (0002) 5 nm nanopillars. (a) The true stress-strain curve. (b-c) Cu/Co pillar before deformation. (d-f) Cross-section view of the pillar at different stages of deformation where atoms are in common neighbor color coding.

Before yielding, Shockley partials are nucleated from Cu/Co interface and glide along the inclined $\{111\}$ planes, interact and transmit across the CTBs in Cu (Figure 3.3(d)), leading to steps on the CTBs [66, 68, 201, 202]. These steps trigger the onset of detwinning in Cu via the migration of Shockley partials along CTBs. Note that the microscopic yielding in the Cu layer does not lead to the significant stress drop

in the stress-strain curve (Figure 3.3(a)). In the Co layer, basal slip is prevented due to the small resolved shear stress (the loading direction is orthogonal to basal planes). Prismatic slip and pyramidal slip are also inhibited by the high density SFs on basal planes. Therefore, the Co layer is also strengthened by the high-density SFs. It has been frequently shown that macroscopic yielding for multilayers occurs when dislocations transmit across the layer interface [18, 50, 96, 179, 203, 204, 205].

In the current study, dislocation transmission across interfaces is prohibited due to slip discontinuity between HCP Co (0002) and FCC Cu (111). The collaborative defect network inhibits the glide of dislocations in Cu and Co layers, and hinders the transmission of dislocations across layer interface, resulting in the ultra-high strength in Cu/Co nanolayers. At increasing stresses, MD simulations reveal that HCP-to-FCC phase transformation occurs in Co at the onset of yielding (Figure 3.3(e)).

The nature of the interfaces (incoherent/coherent) is clearly revealed by top-down view of MD snapshots of the latter, presented in Figure 3.4, where the two types of FCC (100)(Figure 3.4(a)) and (110)(Figure 3.4(b)) Cu/Co interface are dominated by FCC phase with orthogonal SFs, whereas the Cu (111)/Co (0002) interface (Figure 3.4(c)) is incoherent, consisting mainly of atoms in an unidentified crystal structure.

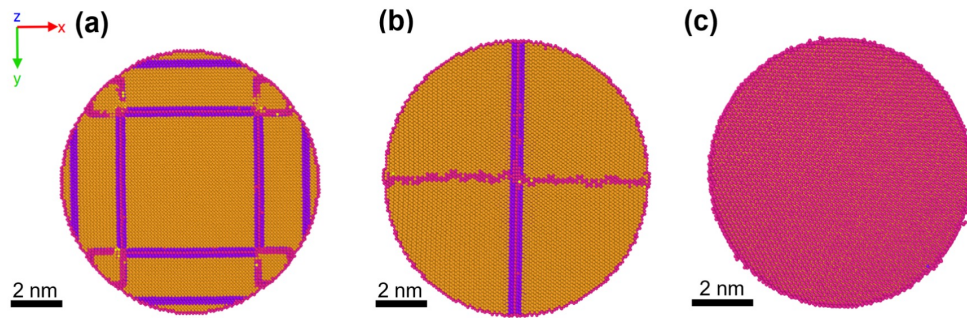


Figure 3.4: Top view of the simulated interfaces between Cu and Co before compression in (a) (100) Cu/Co, (b)(110) Cu/Co and (c) Cu (111)/Co (0002) multilayers in common neighbor color coding. Pink is for unidentified structure.

The entire process - detwinning, phase transformation and propagation of phase fronts - was also examined via dislocation analysis. Dislocation arrays are observed at the FCC Cu/HCP Co phase boundaries and move with the phase boundaries during phase transformation (Figure 3.5). The nucleation of Shockley partials from the interface, their migration along the inclined $\{111\}$ planes and later on along the CTBs resulting in their annihilation are depicted in Figure 3.5(a). Figure 3.5(b) depicts the HCP to FCC phase transformation process. Finally, the expansion of the FCC Cu phase and the nucleation of SFs lead by Shockley partials within it are detailed in Figure 3.5(c).

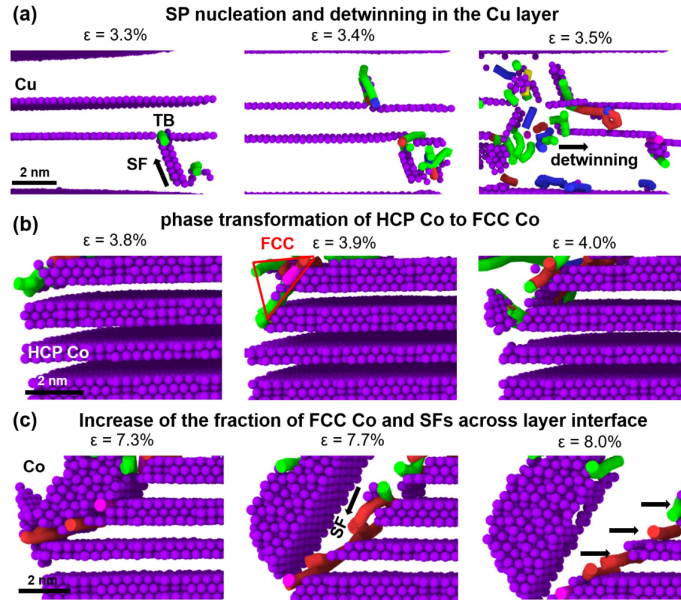


Figure 3.5: Dislocation analysis of the FCC Cu (111)/ HCP Co (0002) 5 nm nanopillar at different stages of compression showing only defect atoms and dislocation lines where Shockley partials are in green, full dislocations in blue, stair-rod in pink other dislocation are in red.

3.4 Experimental Results

XRD patterns of Cu/Co 25 nm multilayers on different substrates reveal highly textured FCC Cu/Co (100) on Si (100) (Figure 3.6(a)), FCC Cu/Co (110) on Si

(112) (Figure 3.6(f)) and Cu (111)/Co (0002) on Si (110) (Figure 3.6(k)). Cu/Co multilayers deposited on Si (100) and Si (112) substrates have FCC Co, while HCP Co (0002) forms on Si (110) substrate. Cross-section EDS analyses show chemically abrupt Cu/Co layer interfaces (Figure 3.6(b),(g),(l)). Cross-section TEM micrographs in Figure 3.6(c)-(e) show that the FCC Cu/Co (100) multilayer contains high-density inclined SFs in the FCC Co layers, but has little defects in Cu layers.

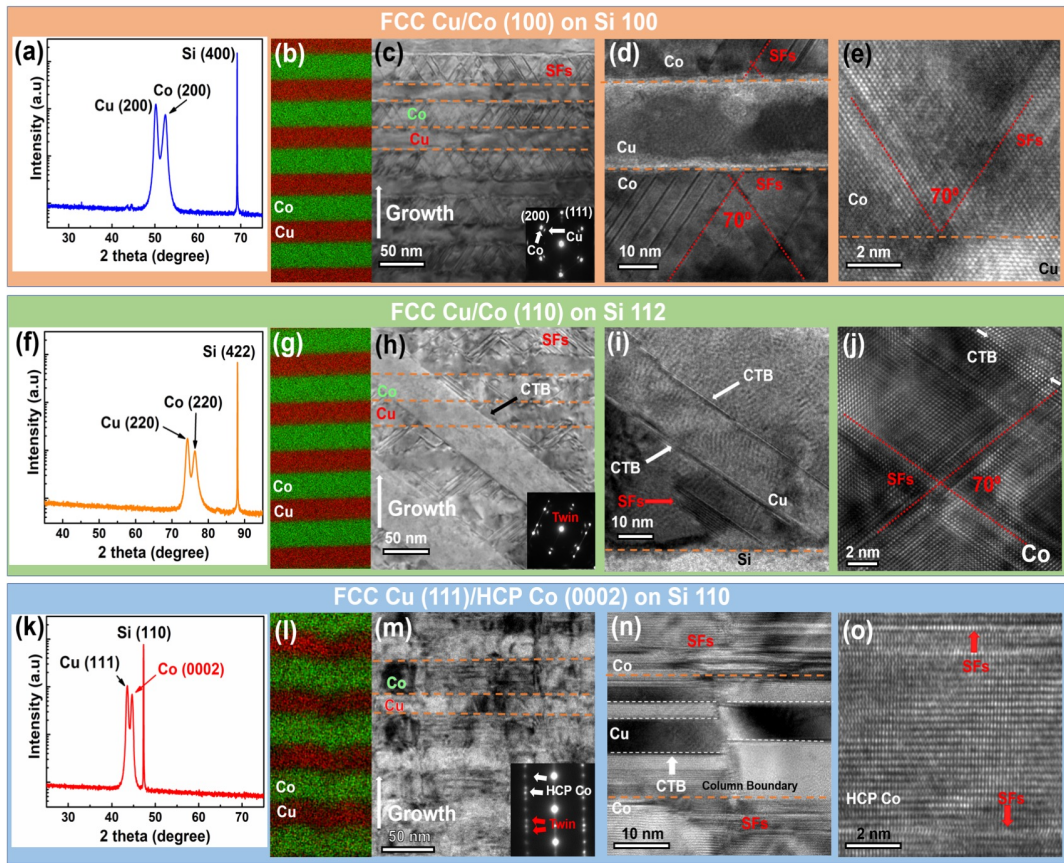


Figure 3.6: Comparison of the microstructures of three Cu/Co 25 nm multilayers with different types of layer interfaces. (a, f, k) XRD profiles. (b, g, l) Cross-section EDS maps of Cu/Co nanolayers. Cross-section TEM (XTEM) micrographs of (c-e) FCC Cu/Co (100), (h-j) FCC Cu/Co (110) and (m-o) Cu (111)/Co (0002).

However, in FCC Cu/Co (110) multilayers, besides the inclined SFs in the Co layers, coherent twin boundaries (CTBs) with ~ 60 nm twin spacing are also observed as confirmed by the selected area diffraction (SAD) pattern in Figure 3.6(h). CTBs

are initiated from Cu/Si interface (Figure 3.6(i)). In contrast to SFs confined within the Co layers, CTBs often penetrate across $\{110\}$ Cu/Co interfaces throughout the entire film thickness.

Cu (111)/Co (0002) films deposited on Si (110) substrates show dramatically different microstructures. Instead of FCC stacking, HCP Co (0002) grows on top of the Cu (111) (Figure 3.6(m)). High-density SFs on the basal planes in the HCP Co layers and CTBs in the Cu layers are observed (Figure 3.6(m),(o)). The three types of defects, SFs-TBs-incoherent layer interfaces, thus, form a defect network. Twin spacing in Cu layer is ~ 8 nm and SF spacing in Co layer is ~ 5 nm. Given the small lattice mismatch between Cu (111) and Co (0002) (as shown in Figure 3.6(k)), highly textured Cu (111)/Co (0002) films form on Si (110) substrate. Consequently, the Cu (111)/Co (0002) multilayer contains the defect network consisting of parallel CTBs (in Cu), SFs (in Co) and incoherent Cu/Co layer interfaces.

Mechanical behavior of Cu/Co multilayers is studied by in situ SEM pillar compression tests. Figure 3.7(a) shows the true stress-strain curves for FCC Cu/Co (100) (blue and light blue) and Cu/Co (110) (orange and yellow) pillars respectively under compression. Both multilayer systems yield at ~ 600 MPa. However, FCC Cu/Co (110) pillars show a more prominent strain hardening with a maximum flow stress of about 1 GPa. On the other hand, the maximum flow stress for FCC Cu/Co (100) pillars is ~ 800 MPa.

Figure 3.7(c) shows SEM snapshots of a deformed FCC Cu/Co (100) pillar (with respect to the blue curve) during compression. One major slip band is nucleated at 10% strain (Figure 3.7(c3)). In the deformed FCC Cu/Co (110) pillar shown in Figure 3.7(d2)-(d4), the first slip band emerges at $\sim 8\%$ strain, followed by the continuous formation of multiple parallel slip bands. Note that the slip bands in the FCC (100) and (110) pillars are both parallel to the $\{111\}$ planes.

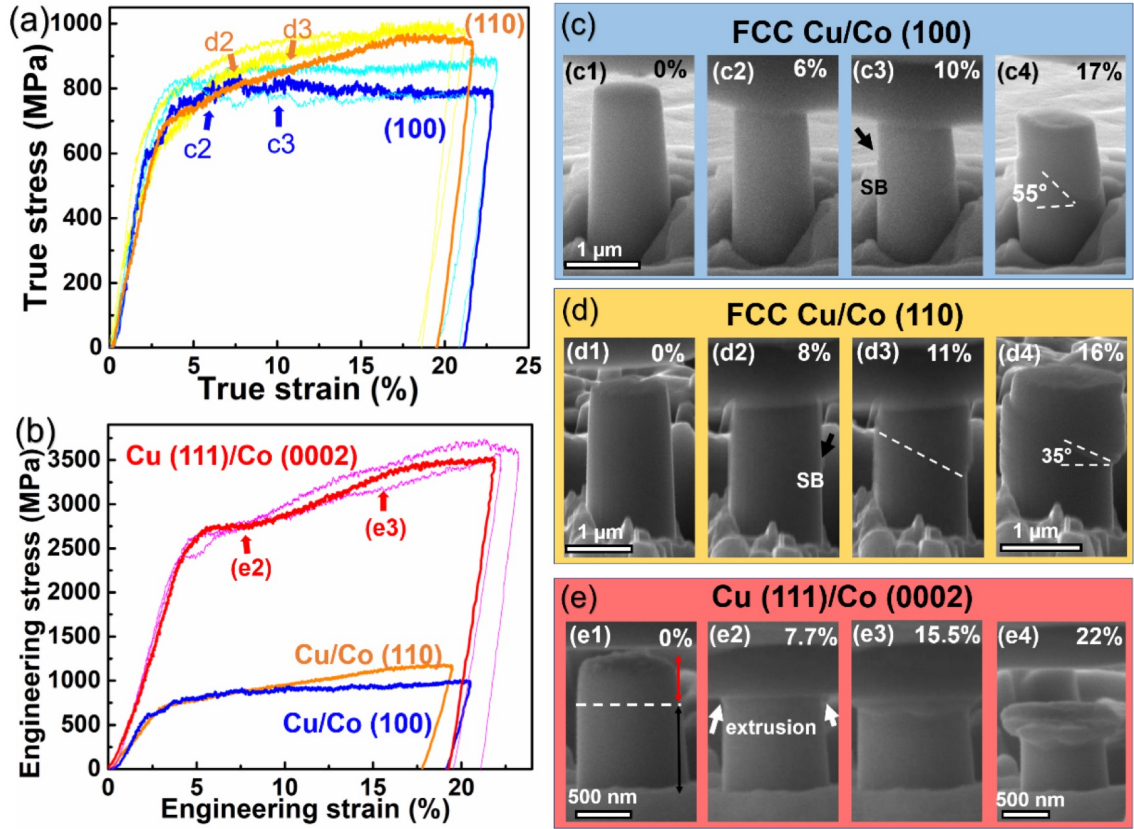


Figure 3.7: In situ micropillar compression tests for the three Cu/Co multilayer systems obtained at a strain rate of 5×10^{-3} /s. (a) True stress-strain curves of Cu/Co (100) and (110) multilayers. (b) Engineering stress-strain curves. SEM snap shots of (c1-c4) Cu/Co (100), (d1-d4) Cu/Co (110) and (e1-e4) Cu (111)/Co (0002) during compression.

In contrast to the two FCC multilayer systems, compression tests on the Cu (111)/Co (0002) pillars reveal drastically different mechanical behavior as shown in Figure 3.7(b). Due to the non-uniform deformation of the Cu (111)/Co (0002) pillar, we compare the engineering stress-strain curves for all three systems. As shown in Figure 3.7(b), the Cu (111)/Co (0002) pillars (red and pink) show a dramatically higher yield strength, ~ 2.4 GPa, which is 4 times that of the two FCC Cu/Co systems and the flow stress exceeds 3 GPa.

SEM snapshots in Figure 3.7(e) show the significant extrusion of the pillar top, as evidenced by the formation of a 200 nm-thick pancake shaped cap, while the bottom

part of the pillar remains largely unchanged. The flow stress is one of the highest among all multilayers under pillar compression studied to date [93, 99, 180, 181, 182, 184, 185, 186, 187, 188, 190, 191, 192, 193, 194, 200, 206, 207, 208].

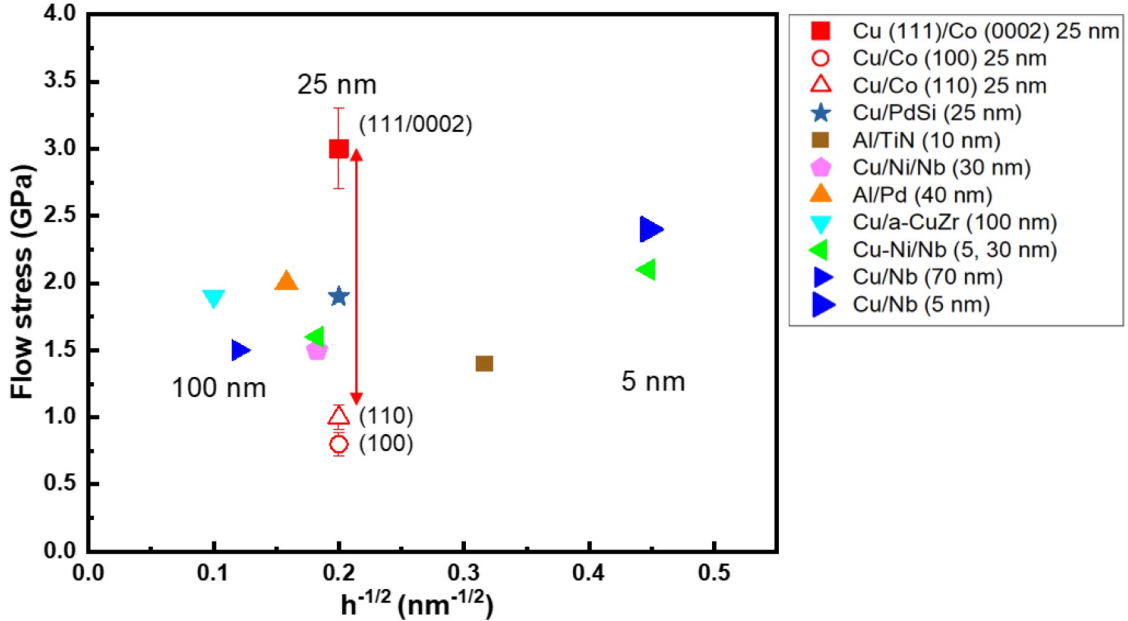


Figure 3.8: Comparison of the flow stress (true stress at 5-10% true strain) of Cu/Co multilayers to other 'ductile' multilayers under pillar compression.

Besides, we compare the flow stress between Cu/Co multilayers with other multilayer systems showing 'ductile' deformation mechanisms (no slip band or crack formation) under pillar compression and plot it as a function of $h^{-\frac{1}{2}}$ in Cu (111)/Co (0002) multilayers have the highest flow stress of ~ 3 GPa among all 'ductile' deformed multilayer pillars reported to date (Cu/PdSi [93], Al/TiN [191], Cu/Ni/Nb [207], Al/Pd [180], Cu/a-CuZr [181], Cu-Ni/Nb [207] and Cu/Nb (5 [99], 70 nm [208])). The detailed strengthening and toughening mechanisms will be discussed in the next section.

3.5 Discussion

3.5.1 Strain Hardening and Deformation Mechanisms of FCC Cu/Co Multilayers

Size dependent strengthening has been well documented in metallic multilayers. In this study, the layer thickness h is 25 nm for all experimental samples, a regime where confined layer slip (CLS) is normally believed to be the dominant deformation mechanism, although dislocation pile-up cannot be entirely suppressed [209].

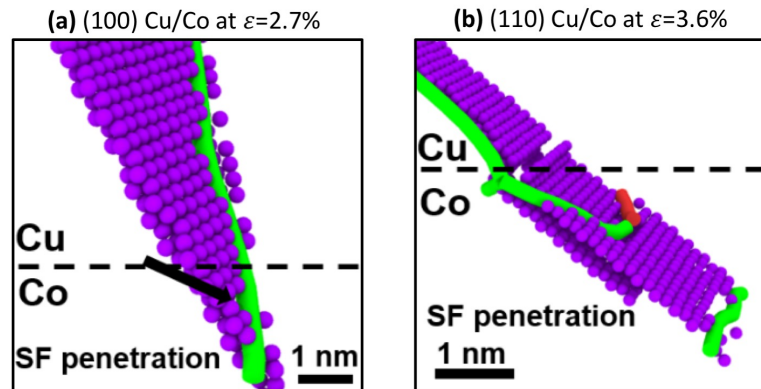


Figure 3.9: Snapshots of MD simulations showing SFs crossing the Cu-Co interface after yield in (100) and (110) Cu/Co multilayers where only atoms of the SF (purple) and Shockley partials (green lines) are depicted.

However, instead of the extrusion of the soft Cu layers, slip bands were observed in both experimental (Figures 3.7(c),(d) and 3.10(a),(b)) and MD (Figures 3.1(d) and 3.11(a)) FCC (100) and (110) Cu/Co multilayers, indicating that CLS may not be the preferred deformation mode. MD simulations of (100) and (110) Cu/Co multilayers with pre-existing strain mismatch induced SFs show that yielding coincides with the SFs crossing the semi-coherent Cu-Co interface (Figure 3.9). On the other hand, TEM micrographs of a deformed (110) Cu/Co pillar (Figure 3.10(c)) show SFs in Cu, which were not observed before deformation.

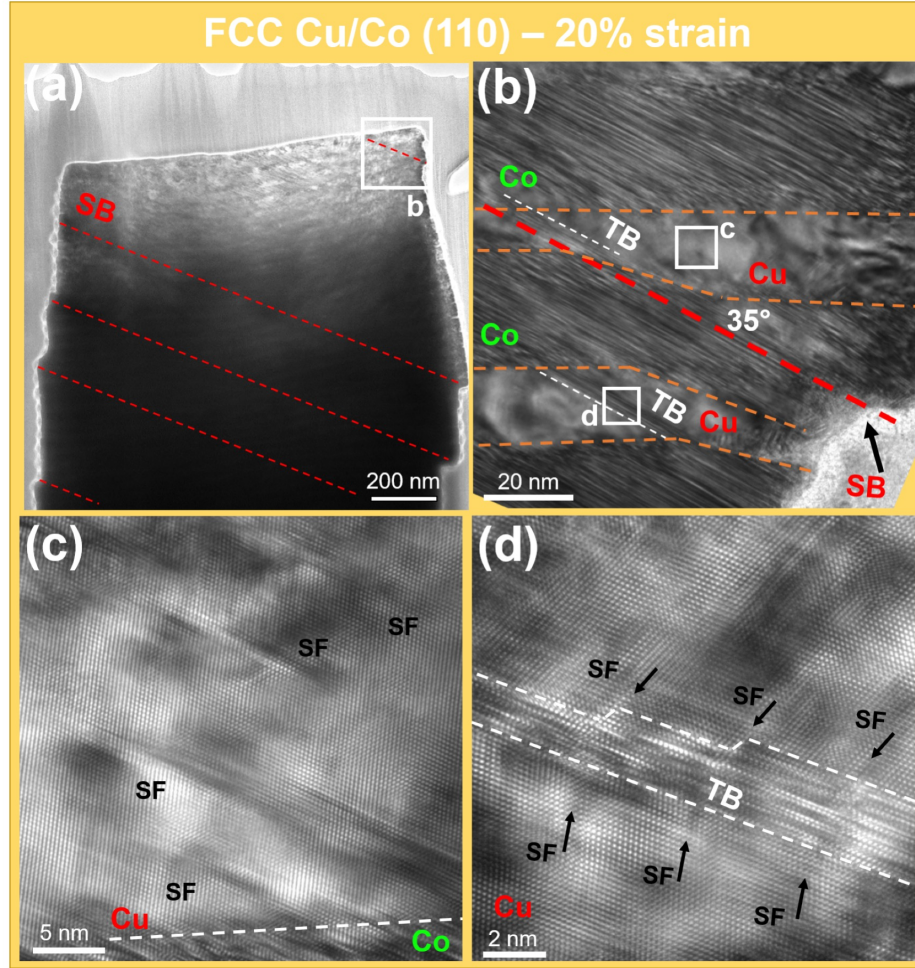


Figure 3.10: XTEM micrographs of the FCC (110) Cu/Co pillar after compression at 20% strain.

These SFs form due to the transmission of Shockley partials across layer interfaces in a similar process to the one depicted by Figure 3.1(e). The transmission of single dislocations through the semi-coherent Cu/Co interface along $\{111\}$ glide plane may set the yield strength of the multilayers. The interface barrier strength can be expressed as

$$\tau_{int} \simeq \tau_K + \tau_{ch}, \quad (3.1)$$

where τ_{int} is the interface barrier resistance, τ_K is Koehler stress originating from modulus mismatch, and τ_{ch} is the chemical interaction term related to SFE difference

between layer constituents [210].

The koehler stress is expressed as

$$\tau_K = \frac{\mu_1(\mu_2 - \mu_1)b}{4\pi(\mu_1 + \mu_2)}, \quad (3.2)$$

where μ_1 and μ_2 are the moduli of Cu and Co, b is Burgers vector, l is dislocation core size, $\sim 2-4 b$. The calculated τ_K is $\sim 170-330$ MPa for both FCC systems. Additionally,

$$\tau_{ch} = \frac{\gamma_2 - \gamma_1}{b}, \quad (3.3)$$

where γ_1 and γ_2 are the respective SFE of Cu and Co.

$$\sigma = \frac{\tau_{int}}{\cos\Phi\cos\lambda}. \quad (3.4)$$

In FCC (100) and (110) multilayers, Φ or λ are complementary to each other, thus, the two systems should have similar yield strength, calculated as $520\sim 870$ MPa.

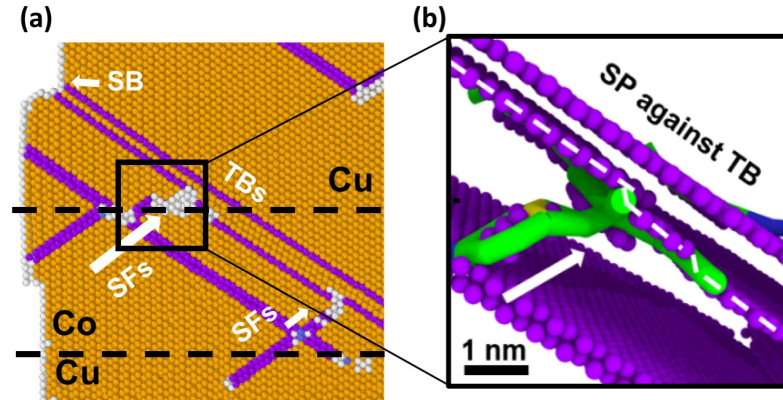


Figure 3.11: Snapshots of MD simulations at $\sim 6.5\%$ showing twin growth in (110) Cu/Co multilayers. (a) Atoms are in Common Neighbor color coding. (b) A close-up of the steps on TBs caused by the intersection with SFs lead by Shockley partials (green lines).

Next, we examine the difference in strain hardening ability between the two FCC multilayers. A major microstructure difference between the two FCC systems are the observed inclined TBs along $\{111\}$ planes crossing the layer interfaces in the FCC Cu/Co (110) film (Figure 3.6(h)-(j)). TBs are known as effective dislocation barriers and contribute to strengthening and work hardening [21, 66, 129, 150, 153, 211, 212], which is observed on the MD simulations stress-strain curve in Figure 3.1(b). MD simulations of (110) Cu/Co pillar show a thickened TB with SF decorations on both sides and steps resulting from the TB-SF interaction appearing at late stages of deformation as depicted in Figure 3.11, similar to what TEM micrographs of the deformed (110)Cu/Co pillar reveal (Figure 3.10(d)). CTBs decorated with SFs have been predicted in simulation [26, 66, 68] and observed experimentally [153, 213], resulting from interactions between the gliding partials and CTBs. The CTBs block the propagation of partials, leading to strengthening and work hardening [21, 66, 129, 150, 153, 211, 212].

3.5.2 Origins of Ultra-high Strength and Plasticity in Cu (111)/Co (0002) Multilayer System

The Cu (111)/Co (0002) 25 nm multilayer is the strongest ductile metallic multilayer reported to date as shown in Figure 3.8. Cu/W 20 nm multilayers have a higher flow stress, but fail in a brittle way. The yield strength and flow stress of Cu (111)/Co (0002) 25 nm multilayer are also much higher than the benchmark values of Cu/Nb 5 nm multilayer [99]. In addition, Cu/Nb 5 nm multilayers form a major slip band after compression to a strain of 28%; whereas, the Cu/Co 25 nm pillar forms a large cap, and sustains up to 90% of true strain without the formation of slip band induced fracture.

The significant yield strength discrepancy between the two FCC Cu/Co systems and Cu (111)/Co (0002) multilayers originates from their different microstructures.

Compared with FCC Cu/Co multilayers, the Cu (111)/Co (0002) multilayers have a defect network, containing three types of mutually parallel planar defects: TBs in Cu, SFs in Co, and incoherent FCC/HCP layer interfaces. We start the discussion with TBs.

TBs are shown to be effective barriers for the transmission of dislocations on the inclined slip systems [58, 66, 129, 130, 150, 153, 170, 211]. However, In situ tensile testing of nanotwinned Cu [213] has revealed that when TB spacing is below 10 nm, dislocation glide along TBs becomes the dominant deformation mechanism, and the stress required to activate partials migration is low, leading to softening observed in nanotwinned metals with small twin spacing. Although the twin spacing in Cu is less than 10 nm, during the uniaxial compression test of Cu (111)/Co (0002) pillar, there is no resolved shear stress for the migration of partials along TBs, and hence, the strengthening of nanotwinned Cu layers is anticipated.

Second, the easy glide plane in HCP Co is the {0002} basal plane [214, 215], which is also normal to the loading direction in this study. At the same time, the activation of $\langle c \rangle$ and/or $\langle c + a \rangle$ dislocations on the pyramidal or prismatic slip planes may be blocked by high density SFs [154], consequently increasing the yield strength of HCP Co.

Third, unlike the coherent FCC Cu/Co interfaces, the incoherent FCC/HCP layer interface is another strong barrier for dislocation transmission. Dislocations in Cu layers may be difficult to transmit through the incoherent interface due to slip discontinuity in FCC Cu and HCP Co.

To sum up the aforementioned rationale, the inclined slip of dislocations and the propagation of slip bands are prohibited by a defect network, consisting of the nanotwins in Cu, high-density SFs in Co, and the incoherent FCC/HCP interfaces, therefore, we may obtain ultra-high strength in the FCC Cu/HCP Co nanolayers.

We also compared the in situ pillar compression results on pure HCP Co with

high density SFs on basal plane [165] and nanotwinned Cu with similar defects density [216], and their flow stresses are both less than 2 GPa with a rule-of-mixture stress of flow stress of 1.5 GPa. These comparisons indicate that the ultra-high strength of Cu (111)/Co (0002) multilayers arises from the TB-SF-interface defect network, rather than from any type of stand-alone defects, as observed through MD simulation, which are in excellent agreement with the post compression TEM analysis, in showing the effectiveness of the previously-mentioned defect networks in blocking partials migration and prohibiting slip band propagation, leading eventually to strengthening and toughening Cu (111)/Co (0002) multilayers. This hypothesis is tested and the mechanisms for the onset of plastic yielding of these high strength nanolayer composites are investigated further.

Mainly, the deformation of Cu (111)/Co (0002) multilayers is dominated by the detwinning in Cu (Figure 3.3(d)) followed by the HCP to FCC phase transformation in Co (Figure 3.3(e)) which turns the incoherent HCP/FCC layer interface into a coherent one, a weak allowing SF transmission across it.

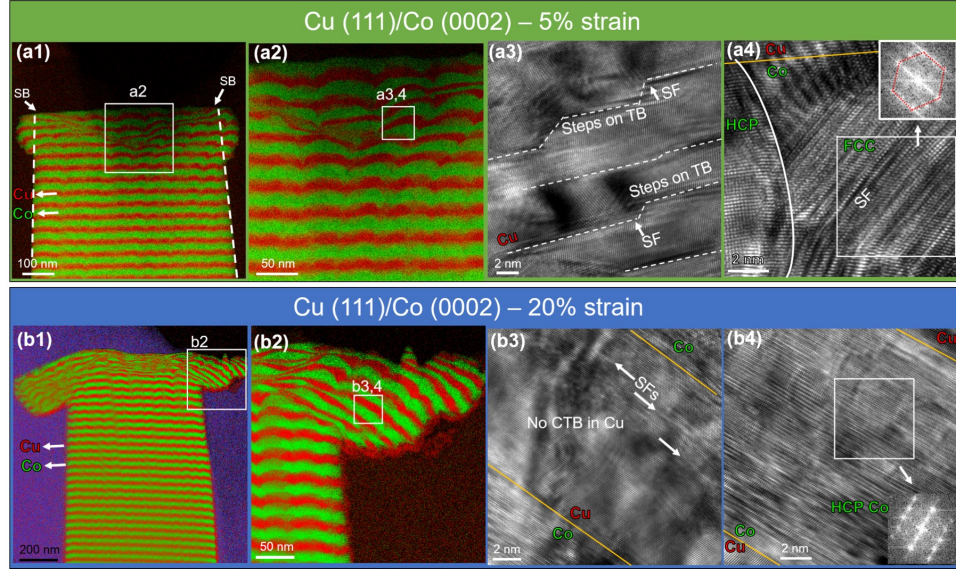


Figure 3.12: XTEM micrographs and EDS maps of the deformed Cu (111)/Co (0002) pillar. (a1,a2) EDS maps of Cu (111)/Co (0002) pillar after deformation to 5% true strain. (a3,a4) XTEM micrographs at the center of the pillar. (b1,b2) EDS map of the multilayers at 20% true strain. (b3, b4) HRTEM micrographs of an extruded but less deformed portion of the pillar top.

Similar mechanisms are also observed in the experimental pillar with the same orientation detailed in Figure 3.12. EDS maps of Cu (111)/Co (0002) pillars deformed to a compressive strain of 5% in Figure 3.12(a1)-(a2) show the prominent dilation of the pillar top. HRTEM micrograph in Figure 3.12(a3) shows steps and SFs on CTBs in Cu. CTBs in as-deposited multilayers are mostly sharp boundaries, and hence the steps on CTBs form presumably due to partial dislocation-TB intersections, similar to what has been observed previously [22, 201]. The steps on the TBs are also active sources for the emission of mobile Shockley partials, promoting plasticity during deformation. In the deformed HCP Co layers (Figure 3.12(a4)), phase transformation from HCP to FCC phase transformation is observed, which may be triggered by high local stresses [173, 174, 175]. In the pillar deformed to 20% of strain, significant co-deformation of Cu and Co to more than 90% has been observed in the top of the pillar as shown in Figure 3.12(b1)-(b2). Significant detwinning was observed in the

Cu layer (Figure 3.12(b3)); and an extremely high density of SFs was observed in the Co layer in the "shoulder of the T-shirt" (Figure 3.12(b4)). FCC Co was the dominant phase in the center of the pillar cap.

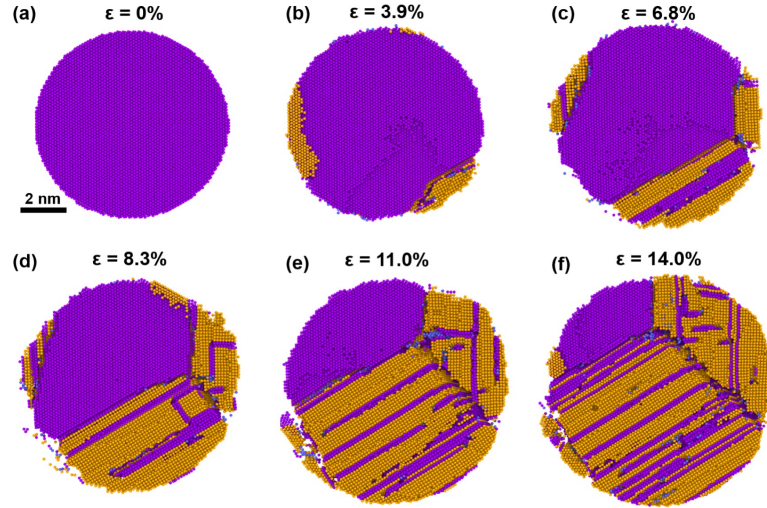


Figure 3.13: Top view of the interface between Cu (111) and Co (0002) at different strain levels. Atoms are in Common Neighbor color coding, where orange is for FCC and purple is for HCP.

When HCP Co is transformed to an FCC crystal structure, the incoherent interface in the Cu(111)/Co(0002) gradually transforms into an FCC/FCC coherent interface. The FCC Cu/FCC Co interface is transparent to dislocation migration, and partial dislocations can easily glide on the inclined $\{111\}$ planes. Figure 3.13 shows the gradual transformation of the Cu-Co interface into an FCC coherent one (orange) decorated with purple lines representing the SFs. At 0% strain, Co is pure HCP (Figure 3.13(a)). When the pillar is deformed to 3.9% strain, HCP Co starts to transform to FCC phase from pillar surface (Figure 3.13(b)). The FCC phase continues to grow, transforming the interface into a coherent one that partials can cross (Figure 3.13(b)-(e)). At 14% strain, more than half of HCP Co transformed to FCC Co and abundant inclined SFs formed across the interface (Figure 3.13(f)). Basically, the deformation induced dislocations are able to penetrate across the

interface, signaled by the penetration of SFs through layer interfaces, leading to plastic yielding accompanied by a significant load drop as shown in Figure 3.3(a).

Continuous deformation leads to rapid propagation of the FCC Co phase front across the HCP layer (Figure 3.3(f)). The softening of Cu/Co system leads to significant co-deformation of Cu and Co (Figure 3.14).

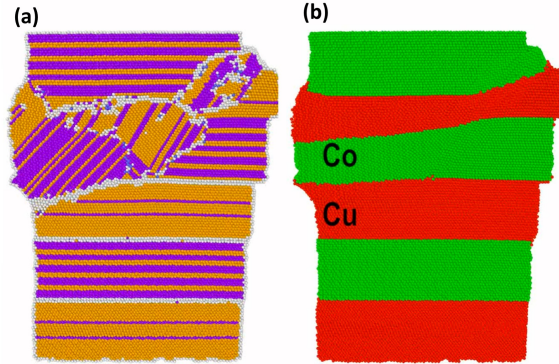


Figure 3.14: Cross-section of the Cu (111)/Co (0002) multilayers after deformation at $\sim 14\%$ strain. (a) Atoms are in Common Neighbor color coding. (b) Atoms are in atom type color coding where Co atoms are green and Cu atoms are red.

3.5.3 Unique Morphology and Significant Deformability Of Cu (111)/Co (0002) Pillars

The strain softening and significant plasticity of the cap layer observed in Figure 3.7(e2)-(e4) arise from dominant partial dislocation activities, manifested by detwinning and phase transformation. The activation of Shockley partials leads to detwinning and softening of the Cu layer. The softening of the Cu layer also leads to the interaction of partials with incoherent layer interface and results in phase transformation in HCP Co layer. The HCP-to-FCC phase transformation of Co leads to transparent Cu/Co layer interface and significant softening. The glide of partials on inclined $\{111\}$ slip systems enables rapid propagation of FCC Co in the multilayers.

Strain softening is critical to accommodate significant plasticity in the deformed pillar cap.

When layer rotation occurs in the top of the pillar (Figure 3.12(b1)), the Schmid factor of the inclined slip systems would increase, consequently promoting the glide of partial dislocations within the layers. In the lower portion of the pillar, there is insignificant layer rotation, and hence, partials cannot be activated and the pillar retains its high resistance to plastic deformation. This unique strain softening mechanism is quite important here to enhance plasticity in this multilayer system. Instead of forming slip bands or cracks like most high strength multilayer systems, the softened layer would sustain the majority of plastic deformation and protect the bottom part from yielding. It is worth mentioning that although detwinning and phase transformation lead to softening in the cap layer, ultra-high stress is needed to activate such activities, leading to the observed high yield strength of Cu (111)/Co (0002) multilayers.

Clearly more experimental and simulation work are necessary to examine the defect network enabled deformation mechanisms in future studies. The current study only unravels a corner of an exciting field, where defect networks may change the deformation mechanisms and impact how we design advanced strong and deformable metallic materials. There are numerous unresolved issues, some of which are listed here. First, the influence of layer thickness on deformation mechanisms of multilayers with defect network requires further investigation. In other words, size effects on deformation mechanisms may be pivotal in conjunction with the defect networks. Second, the current MD simulation focuses on a small model system given by limited computational ability. Large scale MD simulations are necessary, provided the required resources, to examine the deformation mechanisms with greater layer thickness. Third, the general applicability of the defect network concept requires further validation in other systems. Defect networks that contain grain boundaries,

nanovoids, phase boundaries may also operate collaboratively to enable high strength and deformability. Finally, phase transformations occur in Co in the current study. It is unclear if phase transformation is necessary to enable high strength and plasticity in other systems with defect network.

3.6 Conclusion

We report on drastically different mechanical strength and deformability of Cu/Co multilayers with identical individual layer thickness, but having three types of crystallographic orientations and layer interfaces. MD simulations reveal that the transparent FCC (100) and (110) Cu/Co interfaces are weak barriers to the transmission of dislocations or the formation of slip bands. However, the superior strength in FCC/HCP Cu/Co multilayers arises from a defect network consisting of TBs, SFs and parallel incoherent layer interfaces. The plastic yielding of the FCC/HCP multilayer is due to the HCP-to-FCC phase transformations in Co.

In situ micropillar compression studies show that the coherent interface of FCC (100) and (110) Cu/Co, results in a low yield strength of ~ 600 MPa and prominent slip bands during deformation. In contrast, the incoherent Cu (111)/Co (0002) 25 nm multilayer delivers unmatched yield strength, ~ 2.4 GPa, and high flow stress, exceeding 3 GPa, thanks to a defect network consisting of parallel CTBs in Cu, SFs in Co and incoherent layer interfaces. The system also exhibits local superplastic deformation as evidenced by the formation of a cap layer.

Chapter 4

DEFECT NETWORK IN FCC CU/HCP CO MULTILAYERS

4.1 Introduction

In Chapter 3 detailing the study on Cu/Co 25 nm multilayers [217], we show that FCC/HCP Cu(111)/Co (0002) has much higher strength than FCC Cu/Co multilayers although they have identical layer thickness. Coherent twin boundaries (CTBs) in Cu, SFs in Co and FCC/HCP incoherent layer interface forming a defect network collaboratively enhance the strength and deformability.

In order to understand the contribution of each of the different defects on the stress-strain behavior, we performed, via MD, compression simulations on (111)Cu/Co(0002) multilayers with different nanostructures. To this end, we report on four different samples: one with pre-existing TBs in Cu only, one with SFs in Co only, one with no defects in either Co or Cu to isolate the effect of the incoherent interface, and the last one is (111)Cu/Co multilayers with a FCC/FCC coherent interface. We have found that TBs strengthen Cu and prevent the localization of deformation in Cu layers that is observed in the sample with no TBs in its Cu layers.

SFs in Co, however, don't alter the mechanical response significantly since the loading direction inhibits basal slip which is the preferred slip system in HCP metals in both cases. The change in nature of the interface from an incoherent HCP/FCC one to a coherent FCC/FCC one significantly compromises the strength of the multilayers.

We also vary the density of pre-existing SFs in Co to understand their contribution to the strengthening in NMMs, since it has been previously shown that varying the spacing between basal plane SFs in single crystal HCP metals affects their mechanical response [80, 218, 219]. As expected, the sample with a lower SF density has a higher flow stress.

To validate computational findings with experimental results, we rely on systematic studies of highly textured Cu/Co multilayers deposited on Si (110) with three different layer thickness (5 nm, 25 nm and 100 nm). These samples reveal different microstructures and density of defects. Transmission electron microscopy (TEM) analyses are performed on multilayers before and after compression. They show that when h is 100 nm, the deformation is mainly localized in Cu layers due to the lower CTBs density. When h decreases to 5 nm, high resolution TEM (HRTEM) analysis reveals a coherent Cu/Co interface (FCC Cu/FCC Co). The in situ pillar compression studies reveal a softening phenomenon occurring when layer thickness h is 5 nm and 100 nm. Shockley partial dislocations can easily penetrate through the coherent layer interface, which leads to softening.

4.2 Simulation and Experimental Methods

4.2.1 Simulation Methods

The role of pre-existing defects in the response of (111) Cu/(0002) Co multilayers under compression was studied by molecular dynamics simulations using the software LAMMPS [163] with an embedded-atom method potential developed by Zhou et

al. [97]. The simulation models consist of a nanopillar with non-periodic boundary conditions on each of direction. The multilayers differ by the nanostructure. Henceforth, we create the first set of models of (111) Cu/(0002) Co multilayers with a 5 nm layer thickness, a diameter ~ 15 nm and a total height of 30 nm, one with only pre-existing (111) TBs in Cu, one with only pre-existing stacking faults on the basal plane in Co, another with no pre-existing defects in either Co or Cu and one. We also perform compression simulations on (111) Cu/Co FCC/FCC multilayers with the same dimensions having TBs in Cu. The pre-existing TBs in these samples have a spacing of ~ 1.5 nm and the SFs have a spacing of about 1 nm. We compare the results obtained from all models to results from similar simulations on a pillar that has both types of pre-existing defects studied in Chapter 3.

The second part of this study focuses on the impact of SF density in Co layers on the overall strength of (111)Cu/(0002)Co. For that, we consider (111) Cu/(0002) Co multilayers with a 10 nm layer thickness and the same diameter and total height of the previously described set. All of the pillars have pre-existing TBs in Cu and stacking faults in Co with a spacing that takes the values 1 nm, 1.5 nm, 2 nm respectively, although the outcome of the second case is only used to study the defect networks for comparison purposes to support the conclusions drawn from the first and last cases. Note that we opt for a different layer thickness than that of the previous sets of simulations to allow a wider range of SF density.

The simulations are performed at 300 K under the NVT canonical ensemble using the Nose-Hoover thermostat after energy minimization by conjugant gradient to stabilize the structures. After equilibration, the pillars undergo compression at a strain rate of $1.67 \times 10^8/s$ up to a strain value $\sim 15\%$. The results are visualized using Ovito [164] and DXA [120], the dislocation analysis tool embedded in it, and are detailed in the upcoming section. We also rely on stress-strain curves to understand the difference in the mechanical behavior arisen from the difference in the

nanostructure.

4.2.2 Experimental Methods

2 μm thick Cu/Co multilayer films with different layer thickness, $h = 5$ nm, 25 nm and 100 nm, were deposited on Si (110) substrates. Cu/Co multilayers pillars with different layer thickness (5 nm, 25 nm and 100 nm) were then fabricated using SEM and FIB. Their diameter is ~ 1 μm and their height is ~ 2 μm .

4.3 Computational Results

4.3.1 The Role of Pre-existing TBs in Cu

Figure 4.1 is a comparison of simulation results obtained from two similar samples, where the first one has no defects in Cu layers and the second one has pre-existing TBs in Cu 1.5 nm apart (Figure 4.1(b)). The stress-strain curves in Figure 4.1(a) show that pre-existing TBs in Cu increase the yield strength of the multilayers but decrease the flow stress. In both cases, plastic yield occurs when stacking faults nucleate from the highly incoherent Cu-Co interface into Cu (Figure 4.1(c)).

In the pillar with no TBs, as depicted by Figure 4.1(d), Shockley partials migrate freely along intersecting $\{111\}$ planes in the single crystal Cu leading to a complex network of SFs in Cu owing to its low SFE. The interlocking partials form stair-rod type of locks. The high number of locks in Cu, with Co remaining undeformed, leads to hardening. Intersecting stair-rod dislocations form the edges of SF tetrahedra (Figure 4.1(e)) by the mechanism proposed in [83]. At later stages of deformation SF tetrahedra multiply, replacing the complex network of Shockley partials that had nucleated at yield. Figure 4.1(f) depicting a cross-section of the sample at $\sim 11.6\%$ strain reveals undeformed Co, deformation localization in Cu with several SFT created.

Alternatively, A closer observation of the pillar with TBs in Figure 4.1(g) reveals detwinning occurring after yield. Shockley partials nucleate at the Cu-Co interface and migrate towards the TBs.

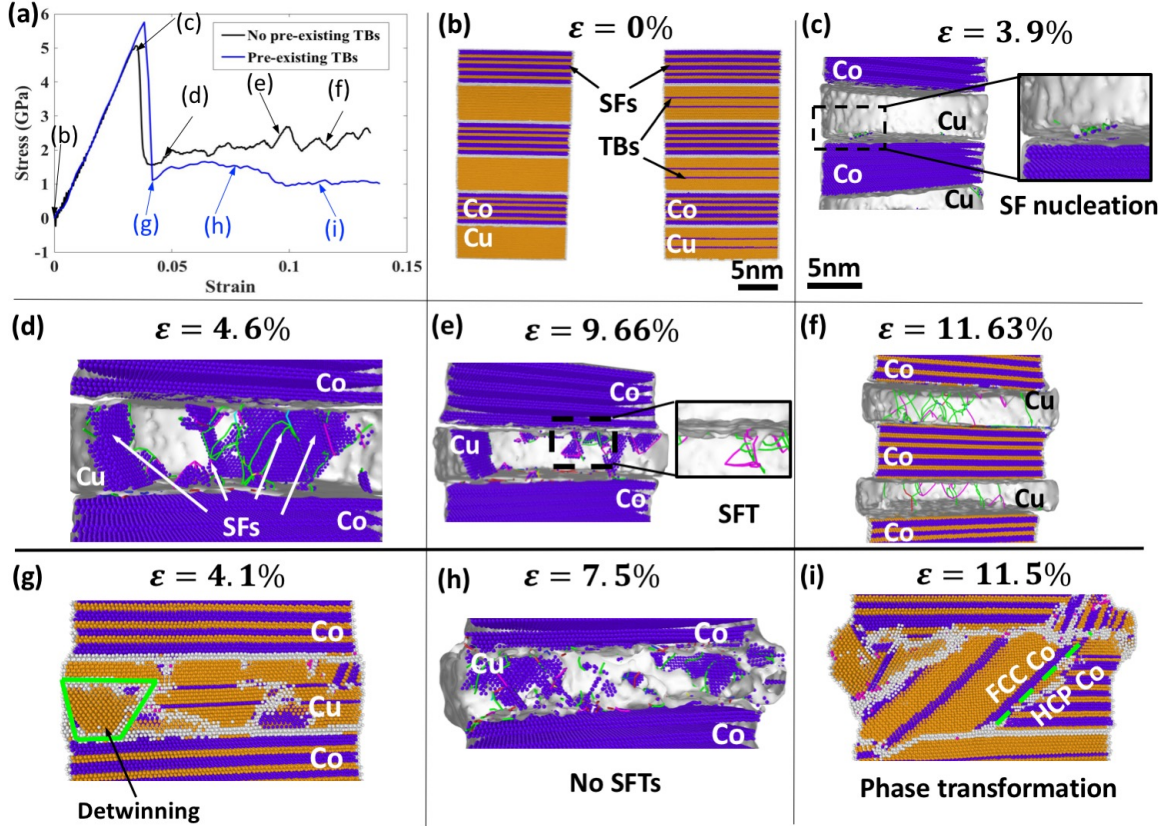


Figure 4.1: MD simulations of compression of (111)Cu/(0002) Co nanopillars with and without pre-existing TBs in Cu in common neighbor color coding (orange is for FCC, purple for HCP and grey for unidentified structure). Green and pink lines are Shockley partials and stair-rod dislocations, respectively.

Arrested by the TBs, partials glide along the TBs annihilating them and leaving a detwinned Cu layer where SFs can propagate (Figure 4.1(h)). The accumulation of partials near the interface triggers the nucleation of an FCC phase in the HCP Co layer, in contrast to the system with single crystal Cu layers, where Co remains in its original HCP structure. Dislocation pile-up is due to the incoherence between FCC Cu and HCP Co and the inability of partials to cross the interface and propagate

further, as well as the confined space between the interface and the TBs. The high density of dislocations on the Cu-Co interface along with the stress fields introduced by SFs increase the local stress around it, eventually triggering the HCP to FCC phase transform in Co as an alternate mechanism to carry plasticity (Figure 4.1(i)) as explained in Chapter 3. Consequently, a comparison of the stress-strain curves illustrated in Figure 4.1(a) for both cases reveals different behaviors caused by the different mechanisms.

4.3.2 The Role of Pre-existing SFs in Co

Unlike pre-existing TBs in Cu, pre-existing SFs in Co don't seem to be directly related to promoting the co-deformation of Cu and Co ensured by the HCP to FCC phase transformation in Co. In fact, the nucleation of the FCC Co phase is observed in both samples, with and without SFs, as demonstrated by Figures 4.2(e) and 4.2(h). The stress-strain curves presented in Figure 4.2(a) are quite similar in both trend and magnitude, an unexpected result given the visible differences in the nanostructures. The pillar with pre-existing stacking faults in Co has a yield stress of 5.75 GPa versus 5.63 GPa for the pillar with single crystal Co. In fact, plastic yield is mainly a consequence of yielding Cu layers, due to the lack of slip systems in HCP Co and the low resolved shear stress on its basal planes that make a 90° angle with the direction of compression. Nevertheless, the pillar with pre-existing SFs in Co undergoes phase transformation in Co and detwinning in Cu simultaneously (Figure 4.2(g)), while phase transformation follows after full detwinning in Cu in the pillar with single crystal Co (Figure 4.2(d)). We attribute this the localization of stress around the Cu-Co interface caused by the presence of SFs in Co. In contrast, the stress required to trigger phase transformation in the pillar with single crystal Co is achieved by dislocation pile-up against the Cu-Co interface after full detwinning in Cu (Figures 4.2(c)-(d)).

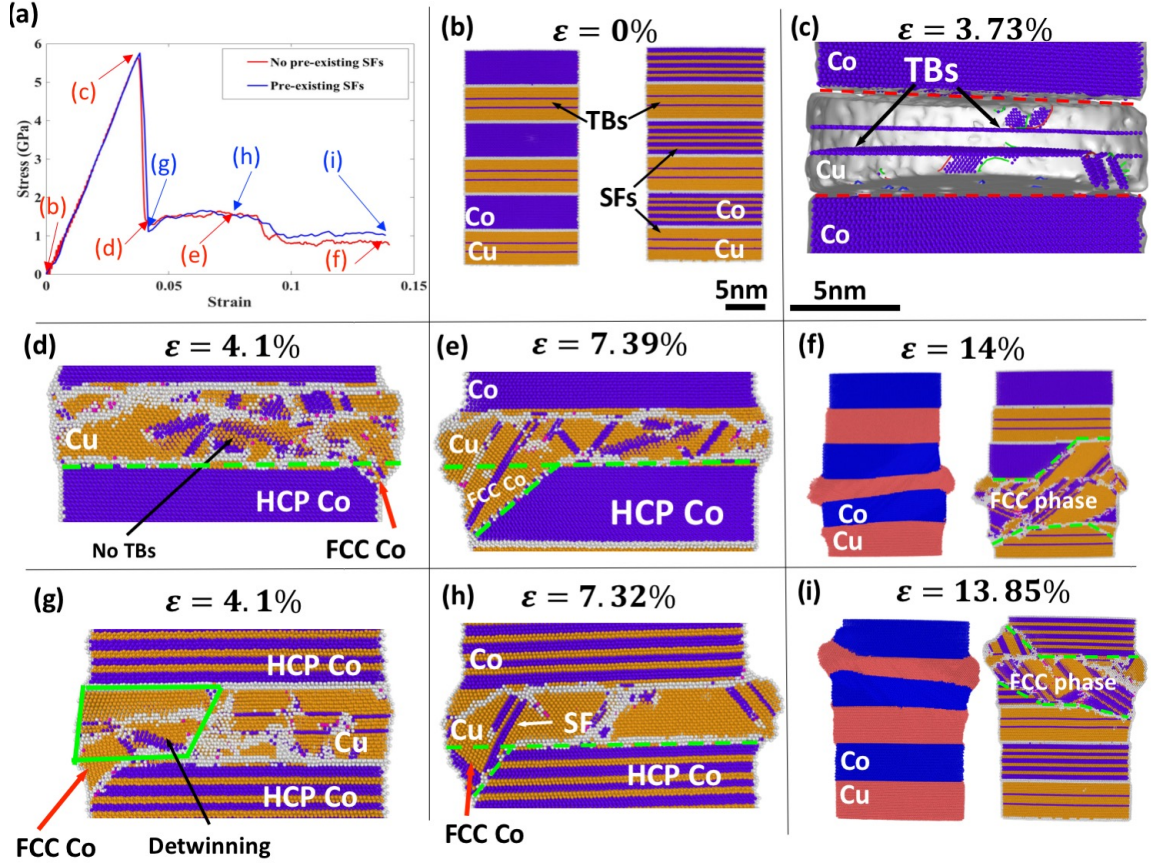


Figure 4.2: MD simulations of compression of (111)Cu/(0002) Co nanopillars with and without pre-existing SFs in Co in common neighbor color coding. Green and pink lines are Shockley partials and stair-rod dislocations, respectively.

HCP to FCC phase transformation turns the incoherent interface to a semi-coherent one allowing SFs in Cu to traverse the FCC Co in both pillars (Figure 4.2(e),(h)). At a late stage of deformation (Figure 4.2(f) and (i)), we observe co-deformation of Cu and Co and the pillars bulge and exhibit a ductile behavior. Comparing Figure 4.2(e) to Figure 4.2(h) taken at the same level of deformation ($\sim 7.3\%$ strain) reveals that the growth of the FCC phase in Co depends on the Co layer's nanostructure. The FCC phase clearly expands further in the sample with no pre-existing SFs, where the growth of the FCC phase is dominated by the defaulting process following partials glide along the SFs similar to the process observed in pure

HCP Co described in Chapter 2.

The unexpected similarities in the mechanical response and the respective evolution in the nanostructure stimulated a question: what is the effect of density of the pre-existing SFs in HCP Co on promoting or demoting certain deformation mechanisms such as phase transformation in Cu-Co multilayers? To answer this question, three other cases where we vary the density of pre-existing stacking faults in Co were investigated and the results are detailed below.

Effect of SF Density

Previous studies on pre-existing SFs in HCP materials have shown that these planar defects and the spacing between them play an important role in determining the mechanical behavior of these materials under mechanical loading. In fact, varying the spacing between pre-existing SFs in Mg nanopillars affects their yield strength and the highest yield stress is achieved by an optimal stacking fault spacing of 6.78 nm at 300K [80]. Additionally, the ability of pre-existing basal SFs to impede dislocation motion helped develop Mg alloys with better mechanical properties [154]. Briefly, these types of planar defects play an important role in defining the mechanical properties of HCP metals.

In this section, we study the effect of varying the density of pre-existing SFs in Co on the mechanical response of Cu/Co multilayers with pre-existing TBs in Cu, equally spaced by ~ 1.7 nm. The goal is to determine whether the stress fields generated by stacking faults and the interactions between them influence the deformation mechanisms and, as a result, the mechanical response.

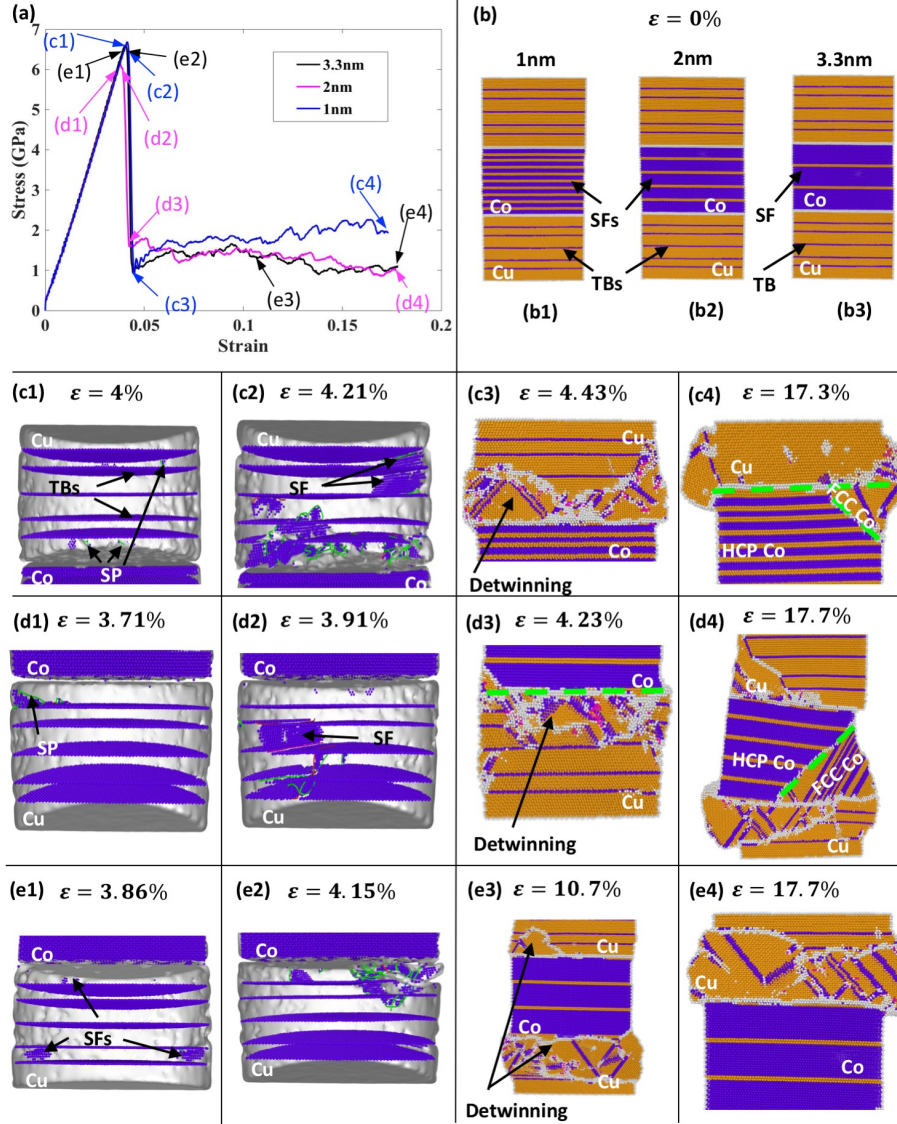


Figure 4.3: MD simulations of compression of (111)Cu/(0002) Co nanopillars with 1 nm (c1-c4), 2 nm (d1-d4) and 3.3 nm (e1-e4) SF spacing in Co in common neighbor color coding. Green and pink lines are Shockley partials and stair-rod dislocations, respectively.

For that, we consider three samples with 10 nm layer thickness and different stacking fault spacing (1, 2 and 3.3 nm), depicted in Figure 4.3(b).

Figure 4.3(a) illustrates the stress-strain curves and Figure 4.3(b) is a cross-section view of the nanopillars pre-compression. Although the three curves match closely until yield, the pillar with a 2 nm SF spacing in Co has a lower yield strength (~ 6 GPa

versus ~ 6.7 GPa for the other two cases). On the onset of yield, SFs nucleate into Cu from the Cu-Co interface in the samples with SF spacing 1 nm and 3.3 nm (Figure 4.3(c1) and (e1)) and detwinning is observed simultaneously (Figure 4.3(c2) and (e2)). However, they nucleate from the outer surface of the pillar with 2 nm SF spacing (Figure 4.3(d1)) and migrate through the Cu layer by Shockley partials transmission across the TBs (Figure 4.3(d2)). This confirms that plastic yield is set by the yield in Cu layers, and the detwinning process leads to a higher yield strength. Further deformation activates phase transformation in HCP Co as an alternative deformation mechanism to accommodate plasticity. Since TBs strengthen Cu layers, the delay in detwinning reduces the strength discrepancy between Cu and Co (Figure 4.3(d3)) and increases the localized stress on the Cu-Co interface, triggering the phase transformation. Alternatively, the detwinning process decreases the strength of Cu layers and deformation is restricted to Cu (Figures 4.3(c3) and (e3)). Further deformation of the pillar with 2 nm SF spacing in Co leads to the growth of the FCC phase in Co and the extrusion of the detwinned regions in the Cu layers (Figure 4.3(d4)). The accumulated stress on the Cu-Co interface due to dislocation accumulation against it and the stress fields around SFs in Co leads to phase transformation in Co at later stages of deformation in the pillar with 1 nm SF spacing (Figure 4.3(c4)). With a lower density of SFs in the sample with 3.3 nm spacing, phase transformation isn't observed up to $\sim 17.7\%$ strain.

In essence, plastic yield in (111)Cu/(0002)Co multilayers is a result of yielding Cu layers. A higher SF density contributes to the localization of stress around the Cu-Co interface necessary to trigger the phase transformation, along with dislocation pile-up in Cu layers.

4.3.3 The Role of Coherent versus Incoherent Interface

In this section, we look into compression simulation results of Cu-Co multilayers with 5 nm layer thickness and no pre-existing defects in either Co or Cu (Figure 4.4(b)), in order to isolate the effects of the incoherent interface on their mechanical response.

The stress-strain curves illustrated in Figure 4.4(a) reveal an overall harder defect-free structure. In fact, the stress fields around the pre-existing TBs in Cu and the pre-existing SFs in Co promote the nucleation of partials from the Cu-Co interface and, hence, plastic yield.

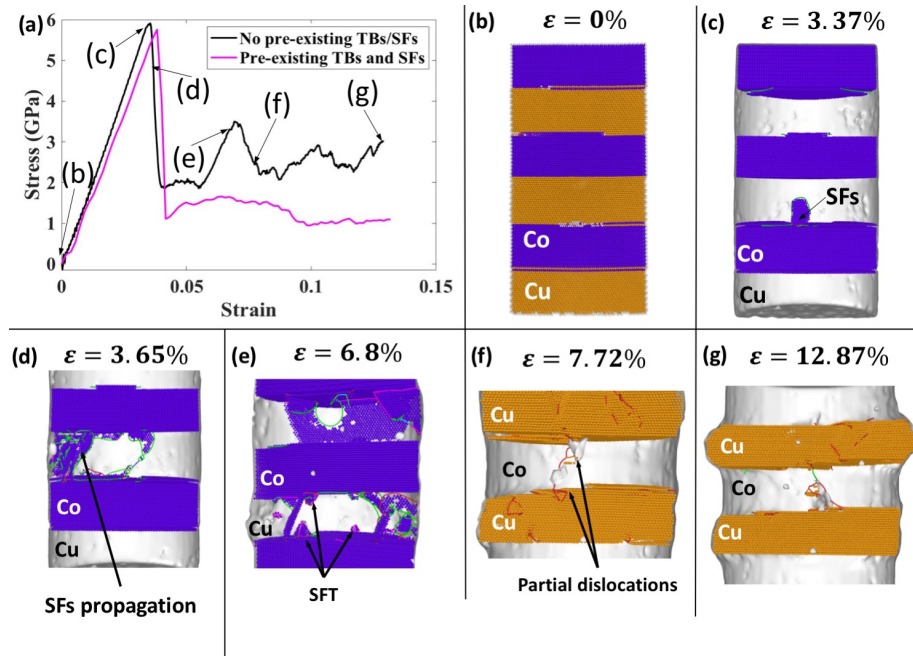


Figure 4.4: MD simulations of compression of (111)Cu/(0002) Co nanopillars with and without pre-existing defects in common neighbor color coding. Green and pink lines are Shockley partials and stair-rod dislocations in Cu, respectively. In Co, $1/3\langle 1\bar{2}10 \rangle$, $1/3\langle 1\bar{1}00 \rangle$ and other dislocations are green, orange and red, respectively.

Without those defects, when higher resolved shear stress is reached on $\{111\}$ planes in Cu, partials finally nucleate (Figure 4.4(c)) resulting in a higher yield stress

than that of the structure with pre-existing defects in both materials. However, the stress drop observed in the defect-free pillar to 2 GPa is less drastic than that of the pillar with pre-existing defects in both Cu and Co to 1 GPa.

The nucleation of numerous SFs on $\{111\}$ planes in Cu and their intersections lead to the formation of stair-rod type locks, similar to the mechanism detailed previously in section 4.3.1. Stair-rods are locks that result from the interactions between Shockley partials and consequently, they decrease their number and limit their mobility exhibiting a higher valley after the peak stress at yield on the stress-strain curve. Later on, the sample undergoes similar mechanisms as those observed in the sample with no TBs in Cu (Section 4.3.1), such as the subsequent nucleation of inclined SFs in Cu layers (Figure 4.4(d)) and their interactions that lead to the formation of several SFT (Figure 4.4(e)). The incoherent Cu-Co interface, especially with no HCP to FCC phase transformation, constitutes a strong barrier to partial dislocation migration and SF propagation increasing the flow stress to higher than 2 GPa versus 1 GPa in the case of the pillar with pre-existing defects, where phase transformation is an alternative mechanism to accommodate plasticity. After reaching a peak of 3.5 GPa at $\sim 7\%$ strain due to the incapacity of nucleating new dislocations in Cu layers and the inability of the existing ones to migrate because of the SFTs, the partials accumulated on the Cu-Co interface activate secondary slip systems in Co. As a result, $1/3\langle 1\bar{2}10 \rangle$ and $1/3\langle 1\bar{1}00 \rangle$ dislocations are observed (Figure 4.4(f)). Although their density is not comparable to those in Cu layers, they persist throughout the remainder of compression and aren't absorbed by the interface nor annihilated by further deformation (Figure 4.4(g)), but the flow stress certainly doesn't drop to the level of the sample that contains an FCC phase in Co that alters the nature of the interface.

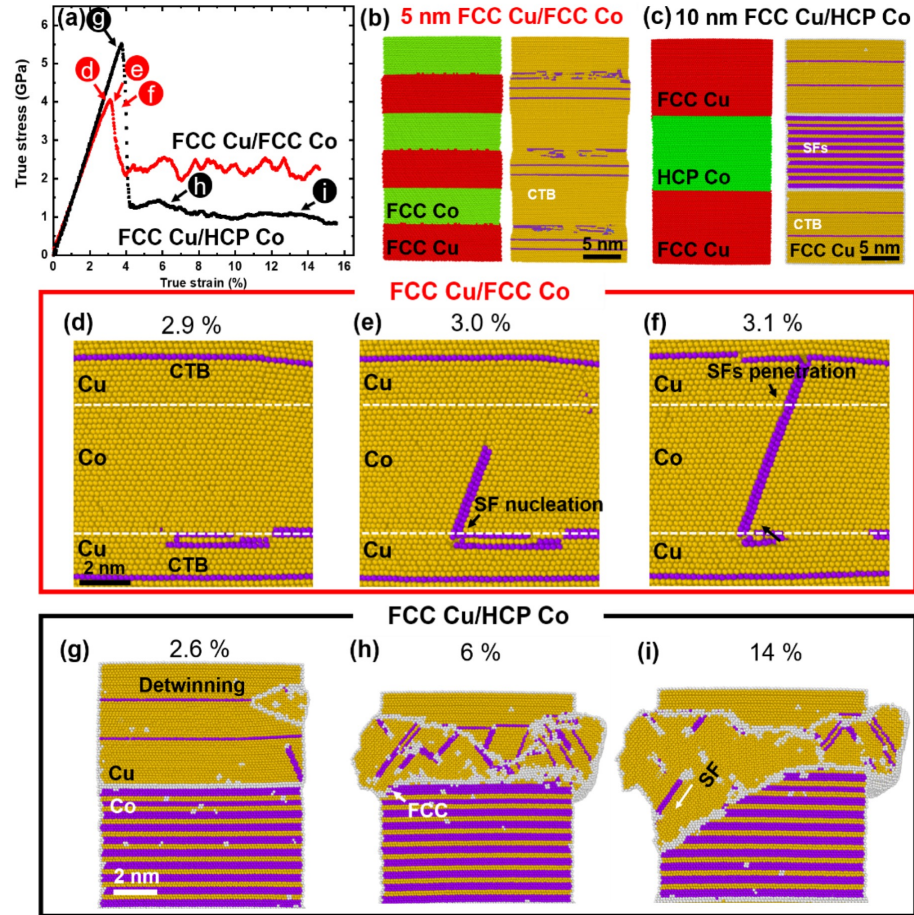


Figure 4.5: MD simulation of compression of FCC Cu/FCC Co 5 nm (b) and FCC Cu/HCP Co 10 nm nanopillars (c). (a) Stress-strain curves. (b,c) Pillars before deformation. Microstructural evolution and dislocation activity in (d-f) FCC Cu/FCC Co pillar and (g-i) in FCC Cu/HCP Co pillar in common neighbor color coding.

Figure 4.5 summarizes the MD simulations results of compression performed on a FCC Cu/FCC Co 5 nm nanopillar (Figure 4.5(b)) with a coherent interface and a FCC Cu/HCP Co 10 nm nanopillar (Figure 4.5(c)) with an incoherent interface. True stress-strain curves (Figure 4.5(a)) show that the FCC Cu/FCC Co 5 nm pillar has a much lower yield strength of about 4 GPa than that of FCC Cu/HCP Co 10 nm pillar. In the case of FCC Cu/FCC Co 5 nm pillar, at yield point (Figure 4.5(d)-(f)), Shockley partials transmit across the coherent Cu/Co interface, signaled by SF penetration, which leads to yield translating by the stress drop after 3.2% strain.

In fact, Before yielding, parallel SFs are observed at the Cu/Co interface in Figure 4.5(d). Then, inclined SFs nucleate at the interface (Figure 4.5(e)). Eventually, inclined SFs transmit across it prompting yielding. While in FCC Cu/HCP Co 10 nm pillar, partial dislocations can't transmit through the incoherent FCC Cu/HCP Co interface (Figure 4.5(g)). Instead, phase transformation of HCP Co to FCC Co is triggered (Figure 4.5(h)) to accommodate the plastic deformation, similar to the MD simulation results for FCC Cu/HCP Co 5 nm pillar described in Chapter 3. SFs can only propagate into the Co layer when it is transformed to the FCC phase as observed in Figure 4.5(i).

4.4 Experimental Results

It is clear that a quantitative comparison between computational and experimental results is not possible due to the inability to dictate the microstructure obtained in experiments, that usually results from growth. Therefore, this section will focus on three experimental samples with different microstructures arisen from layer thickness variation. In fact, the experimental results detailed below present some insight into the relation between the type of interface separating the two materials, as well as the density of defects within the layer, on the deformation mechanisms and thus, on the mechanical behavior of NMMs.

To investigate the mechanical behavior of Cu/Co multilayers with different layer thickness, in situ pillar compression tests were performed (Figure 4.6). Due to the different deformation mechanisms and pillars structure evolution, especially the non-uniform deformation in 25 nm pillars, we plot the engineering stress-strain curves instead of true stress-strain curves to compare the mechanical properties.

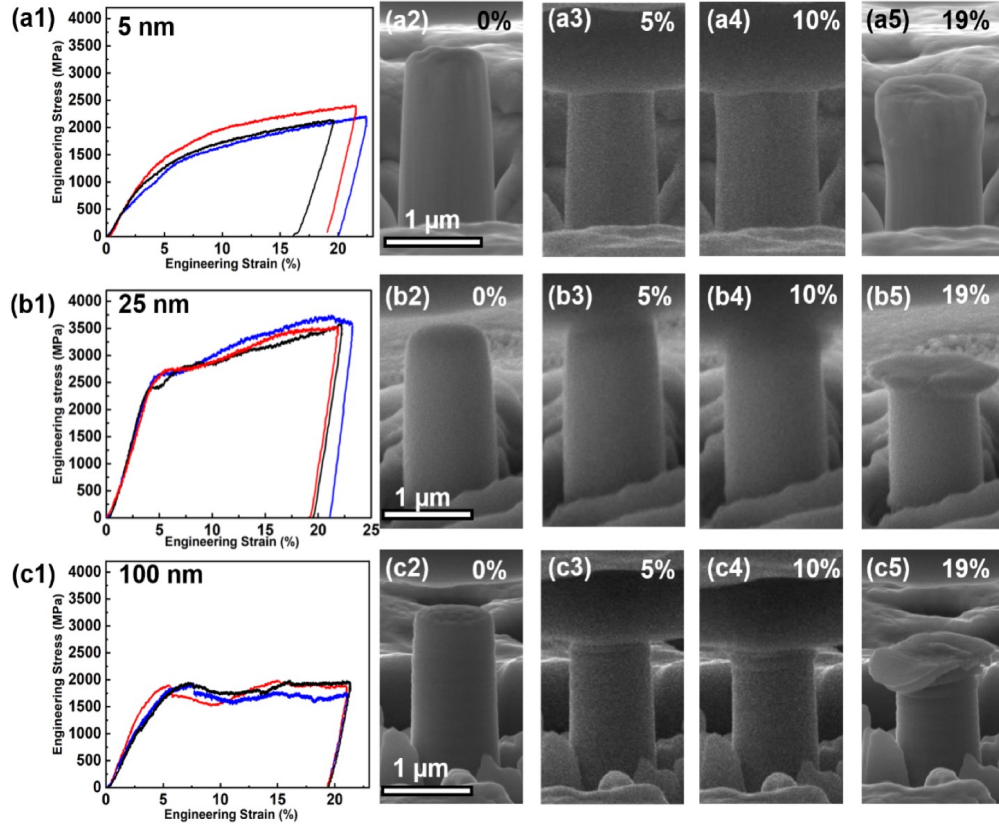


Figure 4.6: In-situ micropillar compression results of Cu/Co multilayers with different h . (a1, b1, c1) Engineering stress-strain curves. SEM images of Cu/Co (a2-a5) 5 nm, (b2-b5) 25 nm and (c2-c5) 100 nm multilayers.

Cu/Co 5 nm pillars have a yield strength of ~ 1 GPa and show prominent work hardening with ~ 2 GPa flow stress. Cu/Co 25 nm pillars exhibit the highest yield strength of ~ 2.4 GPa and flow stress of 3.5 GPa. The yield strength of the Cu/Co 100 nm pillars is ~ 1.2 GPa and it has the lowest flow stress. SEM snapshots of Cu/Co pillars during compression show different deformation mechanisms with different h . When h is 5 nm, traditional barreling at the pillar top is observed, leading to the reverse conical shape (Figure 4.6(a5)). A small slip band is also introduced which is examined by TEM analysis presented in the following section. When h increases to 25 nm, plastic deformation is accumulated at the top layer (~ 500 nm), while the pillar base only deforms elastically. When h increases to 100 nm, there is no co-deformation

of Cu layer and Co layer anymore. Instead, Cu layers yield first (Figure 4.6 (c3)) and extrude out (Figure 4.6 (c4),(c5)), reflected by the wavy stress-strain curve.

4.5 Discussion

4.5.1 TBs and SFs Strengthening Effects in (111)Cu/(0002)Co Multilayers

A comparison of the stress-strain curves illustrated in Figure 4.1(a) for both cases reveals different behaviors caused by the different mechanisms. Specifically, for Cu/Co multilayers with single crystal Cu layers, partial dislocations nucleate and propagate spontaneously across the layer, in contrast to partials in twinned Cu layers, where TBs constitute an obstacle for their migration during early stages of deformation and lead to a high number of dislocations nucleating in the confined space between the TB and the layer interface. As a result, the stress-strain curve of the sample with pre-existing TBs in Cu has a higher yield stress (6 versus 5.5 GPa for the sample with no pre-existing TBs), although they both have a relatively high yield strength due to the inability of partials to propagate through the Cu-Co interface and into the Co layer. The multilayers with no TBs in Cu exhibit localized deformation in Cu with Co layers remaining undeformed. In previous studies, TBs in single crystal Cu improve its hardness by refining the microstructure and impeding dislocation motion [220]. Additionally, the difference in flow stress is a consequence of the dissimilar deformation mechanisms during plasticity. Indeed, the multilayer with no TBs in Cu undergoes hardening during plasticity, due to the formation of SFTs that inhibit partials migration in Cu [221], whereas, the HCP to FCC phase transformation observed in Figure 4.1(i) transforms the Cu-Co interface into a coherent one, making it transparent to partials and enabling them to cross it, hence, the increase of SF density in FCC Co [144], which translates by a softer behavior in plasticity as well.

Overall, pre-existing TBs in Cu layers in (111)Cu/(0002)Co multilayers alter the primary mechanisms activated during plastic deformation and hence, the mechanical behavior of the multilayers under compression.

For HCP Co with a (0002) orientation, deformation is hard under compression because of the nonexistent resolved shear stresses on either basal planes or prismatic planes, which explains why there isn't much difference in the MD samples with and without SFs in Co presented in Figure 4.2. $\langle c+a \rangle$ type dislocations gliding along pyramidal planes are also prohibited by the high density of basal SFs [165]. Therefore, Co remains rigid because not only Co has inherent high strength but it's also along a hard deformation orientation, hence, the strength disparity between Cu with lower density or no TBs and Co with a high density of basal SFs.

With TBs strengthening Cu layers and the interacting stress fields of incoherent Cu-Co interfaces, HCP to FCC phase transform occurs in both samples presented in Figure 4.2, which leads to co-deformation of Cu and Co and softening observed after yield. Since plastic yield starts in Cu layers with a similar microstructure in both samples leading to similar yield strength in both samples specially that Co layers don't deform until the FCC phase nucleates, which occurs during plasticity.

The localized deformation in Cu is also observed in Cu/Co 100 nm experimental sample. In this sample, Cu layers have a lower density of TBs and Co layers have a lower density of SFs. The non-uniform deformation after yielding manifests by the preferential extrusion of Cu layers (Figure 4.6(c)). It is due to the strength disparity between FCC Cu (111) and HCP Co (0002) as mentioned earlier. The preferential deformation on the softer layer is also observed in Cu/Zr, Cu/a-CuNb and Al/Pd multilayers [180, 181, 196, 203].

4.5.2 Interface Dominated Deformation in Cu/Co Multilayers

In Chapter 3, we have established that incoherent interfaces separating FCC Cu and HCP Co in (111)Cu/(0002)Co are a strong barrier to dislocation migration due to slip discontinuity between (111)Cu and (0002)Co, which contributes to strengthening; and its conversion to a coherent interface by HCP to FCC phase transformation in Co makes it transparent to dislocations, therefore, improving ductility. Additionally, MD results summarized in Figure 4.4 prove that, even in the absence of defects in Co and Cu, the pillar still exhibits a higher yield strength and flow stress than the pillar with pre-existing defects, especially that no HCP to FCC phase transformation is observed and the incoherent interface is preserved. In contrast, a coherent interface such as the one separating Cu and Co in (111)Cu/Co multilayers (Figure 4.5) is a weak barrier for dislocations and they can glide easily across it.

Experimental compression results reveal that Cu/Co 5 nm pillars are unexpectedly much softer than Cu/Co 25 nm pillars under compression in contrast to the 'stronger' is smaller rule observed in NMMs. Although CTBs and SFs are observed in Cu/Co 5 nm multilayers, they could not form an effective defect network due to the absence of the incoherent interfaces.

Post deformation on Cu/Co 5 nm pillars TEM analysis is performed as shown in Figure 4.7. A slip band is observed in Figure 4.7(a) and Figure 4.7(b). Figure 4.7(c) shows a majority of FCC Co in the Co layer and a coherent interface between FCC Cu/Co. Near the slip band region, high density of inclined SFs and slip traces are observed, resulting from Shockley partial dislocations transmission across the Cu/Co interface along inclined (111) planes as observed in MD simulations (Figure 4.5(d)-(f)).

In metallic multilayers, when h is less than 10 nm, transmission of single dislocation across layer interface is the dominant deformation mechanism [18, 94, 96, 99, 176, 177, 210]. Under compression, partial dislocations gliding along inclined

(111) planes can easily propagate across the coherent Cu (111)/Co (111) interface, significantly degrading the maximum strength of Cu/Co multilayers.

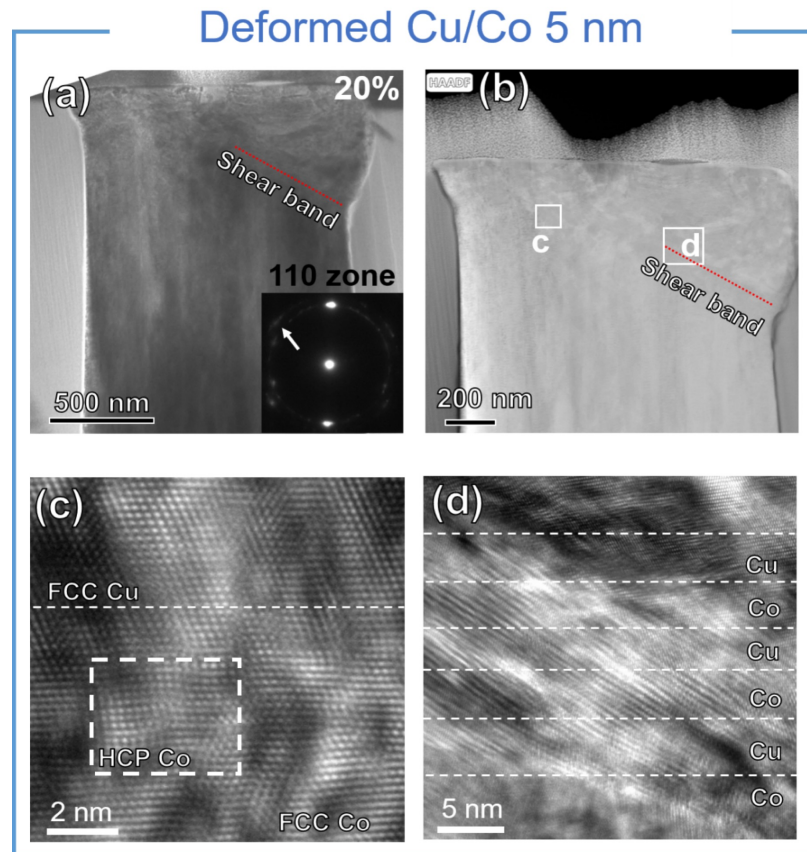


Figure 4.7: TEM (a) and STEM (b) micrographs of Cu/Co 5 nm pillar deformed up to 20% strain. (c),(d) HRTEM micrographs of two different zones of the deformed pillar defined in (b).

4.6 Conclusion

In summary, atomistic simulations of compression were performed on (111)Cu/(0002)Co multilayers with different nanostructures to elucidate the synergistic role of three specific types of pre-existing defects, namely the Cu-Co interface, CTBs in Cu and SFs in Co, in imparting ultra-high strength and plasticity. The simulations reveal that the incoherent HCP Co-FCC Cu interface serves as an

effective barrier for dislocation motion across layers leading to high strength. The CTBs in Cu play two roles. They decrease the strength discrepancy between Cu and HCP Co by obstructing the motion of partials that nucleate from the Cu-Co interface contributing to high yield strength. In addition, the glide of dislocations along the CTBs triggers detwinning and the dislocation pile-up contributes to the localized stress required to activate HCP to FCC transformation. Thus, Cu-Co interface becomes transparent to partial dislocations motion thereby accommodating plasticity and ensuring co-deformation of Cu and Co. Finally, SFs in Co contribute to high strength by prohibiting slip on prismatic or pyramidal systems in the HCP Co layer. In addition, their high density improves plasticity by increasing stress localization around the Cu-Co interface which leads to nucleation and dislocation pile-up in the Cu layer, hence, activates the phase transformation. Thus, consistent with experimental studies, our MD simulations show that the three parallel planar defects work together to impart an attractive combination of high strength and plasticity. This work opens avenues for the design of other metallic multilayer systems with superior mechanical properties using pre-existing defect networks.

Chapter 5

DEFORMATION MECHANISMS IN FACE CENTERED CUBIC CO DOMINATED BY STACKING FAULTS

5.1 Introduction

In this chapter, we investigate the mechanical properties of single crystal FCC Co pillar with pre-existing high-density inclined SFs by MD simulations and experimental compression tests to provide a comprehensive understanding of possible deformation mechanisms that may lead to SF-dominated response at different strain rates. Under compression, the Co pillars show strain softening and hardening respectively at different strain rates. It is worth mentioning that although most MD simulations are inherently limited by extremely high strain rates (of the order of $10^8/s$) and may not be ideal computational tools for studying strain rate dependence, especially at experimentally relevant strain rates [222], these simulations have been successfully

applied to explain deformation mechanisms in metallic materials. The purpose of MD simulations is to elucidate possible SF-mediated deformation mechanisms that may qualitatively explain the strain rate dependence observed in experiments.

5.2 Computational and Experimental Methods

5.2.1 Computational Methods

A nanopillar with circular cross-section consisting of a seed layer of FCC Cu and an upper layer of FCC Co was generated for atomistic simulations. The pillar had a diameter of 18.4 nm and the height of the Co layer was 38.4 nm, Thus, the height-to-diameter aspect ratio of the Co pillar for compression study is $\sim 2:1$. The thickness of the Cu layer was 6 nm. Both layers had the following crystallographic orientation: x: $[0\ 1\ \bar{1}]$, y: $[0\ 1\ 1]$, z: $[1\ 0\ 0]$. The Co layer consisted of $\sim 900,000$ atoms. Non-periodic boundary conditions were specified in all directions. The Cu seed layer was made rigid to promote the nucleation of defects in the Co layer. The Cu-Co interactions were modeled using the embedded-atom method (EAM) interatomic potential developed by Zhou et al. [97]. The system was first relaxed at 0 K by conjugate gradient energy minimization and then equilibrated at 300 K for 100 ps using the Nose-Hoover thermostat in the NVT ensemble. The compression simulations were performed at strain rates of $1.37 \times 10^8/\text{s}$ and $1.37 \times 10^9/\text{s}$, by keeping the Cu layer fixed and applying a constant velocity to a thin slab of Co, about 2 nm in thickness, at the top. All simulations were performed in LAMMPS [163], OVITO [164] was used for visualization and DXA tool in Ovito [120] for dislocation analysis.

5.2.2 Experimental Methods

1 μm thick Co film with 100 nm thick Cu seed layer was deposited on Si (100) substrates at a rate of $\sim 0.3\ \text{nm/s}$ for Co. Transmission electron microscopy (TEM)

image of FCC Co examined along $[100]$ zone axis (Figure 5.1(a)) shows arrays of orthogonal high-density SF ribbons. The inserted selected area diffraction (SAD) pattern shows superlattice types of diffraction spots arising from high-density SFs. SF ribbons intersecting at 70° are observed in the cross section TEM (XTEM) view along $[110]$ zone axis (Figure 5.1(b), 5.1(c)). High resolution TEM (HRTEM) micrograph in Figure 5.1(d) shows detailed intersections of two SF ribbons. Then, three single crystal FCC Co pillars with ~ 500 nm diameter were fabricated using the focused-ion-beam (FIB) technique. The height/diameter aspect ratio is $\sim 2:1$ for all micropillars. Compressive tests at low ($1 \times 10^{-3}/s$) and high ($5 \times 10^{-3}/s$) were performed, as well as a jump test. More details on the experimental techniques and methods can be found in [144].

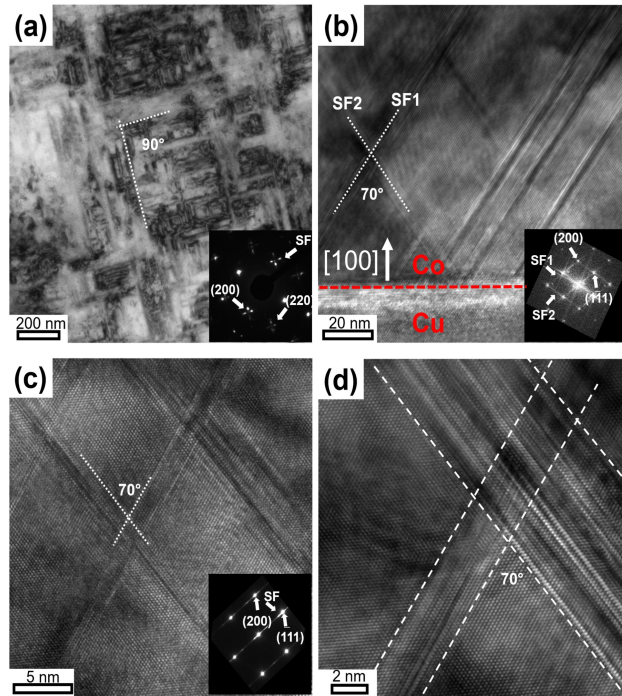


Figure 5.1: (a) Plan-view TEM micrograph from the Co $[100]$ zone axis. (b-c) Cross-section TEM (XTEM) micrographs examined from the Co $[110]$ zone axis showing intersecting SF ribbons that keep propagating after interception. (d) HRTEM micrograph.

5.3 Computational Results

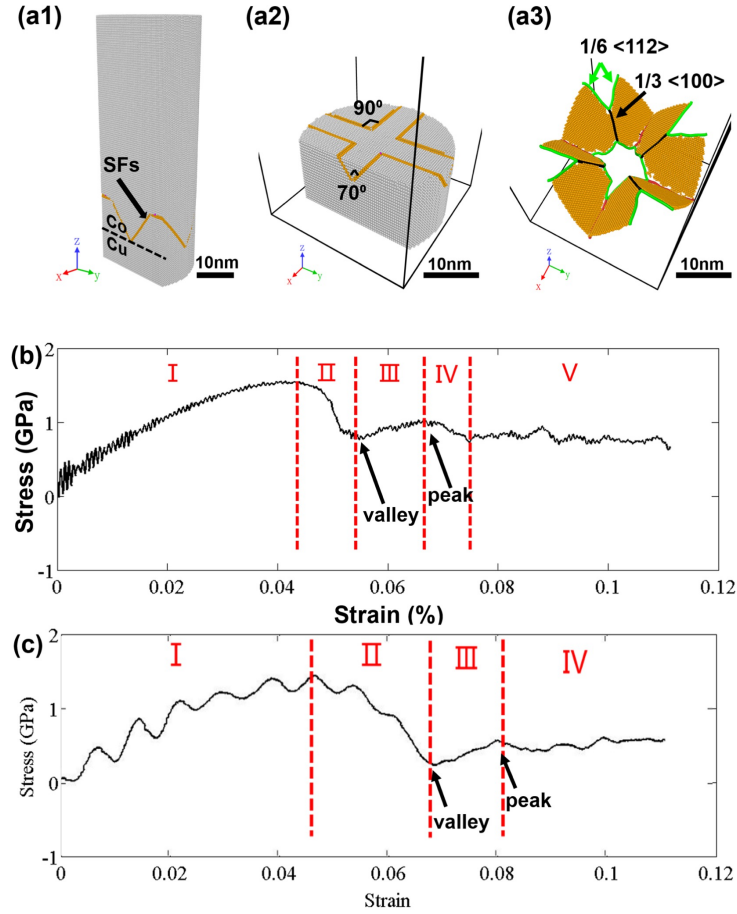


Figure 5.2: MD simulation results for compression of a Cu-Co bilayer nanopillar. (a1) Cross-section view of the pillar before deformation. (a2) A tilted top-down view of initial SFs formed in FCC Co. (a3) Shockley partials (green) and Hirth locks ($b=1/3 \langle 100 \rangle$, black). The stress-strain curves for nanopillar compression at a strain rate of (b) $1.37 \times 10^8/s$ and (c) $1.37 \times 10^9/s$.

To understand the influence of pre-existing SFs on the deformation mechanisms of FCC Co, MD simulations of nanopillar compression at different strain rate on FCC Co were performed. 70° inclined and orthogonal SFs are observed at the Cu/Co interfaces (Figure 5.2(a1), 5.2(a2)), in excellent agreement with the TEM observations presented in Figure 5.1. Careful examination of dislocations near the interface show

pairs of $1/6 \langle 112 \rangle$ Shockley partials, connected by immobile Hirth locks with Burgers vector of $1/3 \langle 100 \rangle$ (Figure 5.2(a3)). Figure 5.2(b) shows the stress-strain curve for the compression simulation performed on the FCC Co/Cu specimen at a strain rate of $1.37 \times 10^8/s$. The stress increases rapidly with strain to a maximum of ~ 1.5 GPa, and then decreases and stabilizes at ~ 1 GPa. Based on different deformation mechanisms observed as compression progresses, we divide the stress-strain curve into different regimes (I-V). There appear to be two hardening regions (I and III) and two softening dominated regions (II and IV) with distinct mechanisms and dislocation activities. We also performed a compression simulation at a higher strain rate of $1.37 \times 10^9/s$ (in Figure 5.2(c)) to do a comparative study of the defect density in the two cases, which will be discussed later. As expected, both cases show similar stress-strain curves since they are both obtained from high strain rates compared to the ones used in experiments. Hence, the following discussions focus primarily on the MD simulations of nanopillar compression at the lower strain rate. Atomic structures along with dislocation analyses analyzed at different strains are shown in Figure 5.3 and 5.4 to gain atomistic insight into the corresponding microstructure evolution.

Initially, the interior of the pillar is relatively free from dislocations (Figure 5.3(a1)) except for the preexisting Shockley partials and Hirth locks formed at the Cu/FCC Co interface. The increase of compressive strain from 0 to 4.6% leads to shortening of the Hirth lock dislocations, which never dissociate into Shockley partials entirely and hence we believe that they contribute to the hardening observed in Region I. As these preexisting Shockley partials are restricted by Hirth locks, there are no other mobile dislocations to accommodate deformation, leading to the so-called dislocation starvation induced hardening [198, 223, 224, 225]. At the peak stress (Figure 5.3(b1)), mobile partials are nucleated from the pillar surface. The partials then rapidly propagate and increase the volume fraction of the SFs in the Co pillar (Figure 5.3(b2)-(b4)), accompanied by rapid stress drop or softening. Figures

5.3(b3)-(b4) also show the nucleation of SFs on multiple slip planes and the formation of dislocation locks at the intersections of these SFs. The introduction of these new dislocation locks initiates the hardening observed in regime III.

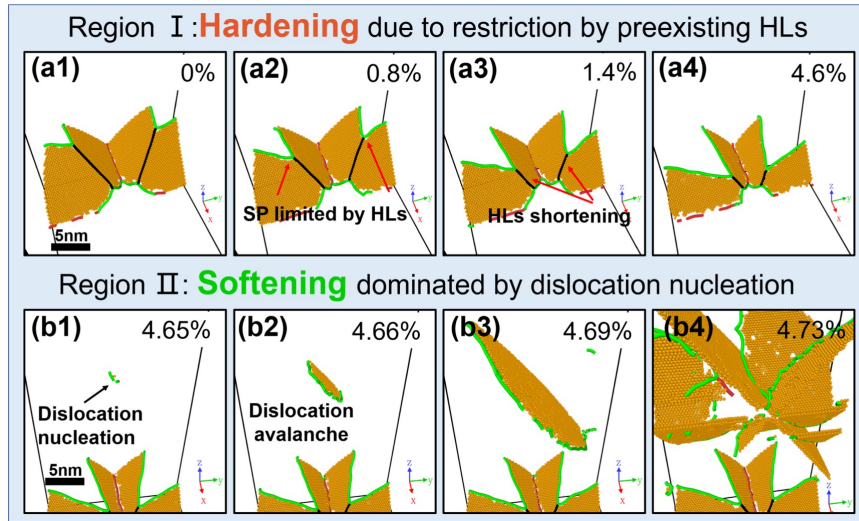


Figure 5.3: Nanostructure evolution at different strains during Region I and II in common neighbor color coding using dislocation analysis. Only defect atoms arranged in HCP structure are shown (orange). Using dislocation analysis, the green lines show Shockley partials (SP), Hirth locks (HL) are in black, and the red lines show other types of dislocations.

As the plastic deformation continues, the density of SFs and Shockley partials increases dramatically, leading to two consequences. First, subsequent nucleation of intrinsic SFs along existing SFs results in thickened SF ribbons, which limit the migration of dislocations in the FCC structure. Second, the density of sessile dislocations (Hirth locks and stair rod dislocations) increases rapidly. The migration of mobile partial dislocations is significantly inhibited by the intercepting SFs and Hirth locks. During the deformation in region III, 3D views of the snapshots in Figures 5.4(a1)-(a4) show the rapid increase of the population of Hirth locks due to the intersecting SFs, and locks and intersections are stable even as the compressive strain increases from 5.49% to 6.5%. The 2D views in Figure 5.4(a1')-(a4') clearly show interceptions of SFs and HCP laminates.

During deformation in regime IV (corresponding to slight softening observed from strain of 6.6% to 7.5%), Shockley partials exiting from SFs intersections glide along the SF ribbons (appearing as HCP laminates sometimes), leading to the formation of TB (Figure 5.4b1-b4). As shown in Figure 5.4(b2')-(b4'), continuous migration of Shockley partials along the TB leads to TB migration along the normal direction.

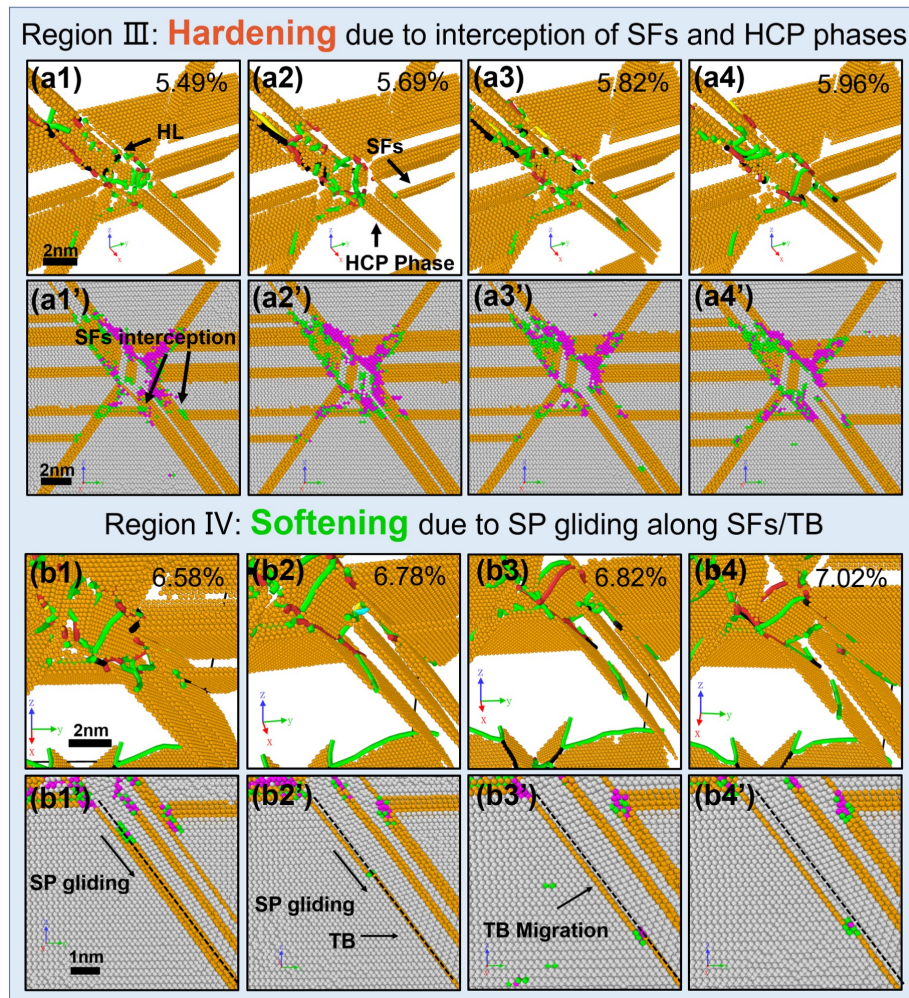


Figure 5.4: Nanostructure evolution at different strains during Region III and IV in common neighbor analysis (orange is for HCP, grey for FCC and pink for BCC) along with dislocation analysis.

5.4 Experimental Results

To investigate the deformability of FCC Co, three sets of compression tests at different strain rates were performed. The stress-strain curves for the micropillars tested at low ($1 \times 10^{-3}/\text{s}$) and high ($5 \times 10^{-3}/\text{s}$) strain rate are different. At low strain rate ($1 \times 10^{-3}/\text{s}$), the yield strength of the micropillar is ~ 700 MPa (red curve shown in Figure 5.5(a)). After a short strain hardening stage (with a strain hardening exponent n of 0.25 ± 0.05) leading to a peak stress of ~ 1100 MPa, the micropillars tested at the low strain rate experience prominent strain softening. In contrast, the micropillars tested at the high strain rate (blue curve shown in Figure 5.5(a)) experience no softening. The yield strength and flow stress plateau are ~ 700 MPa and 1400 MPa, respectively. The strain hardening exponent is 0.35 ± 0.02 for pillars tested at this strain rate.

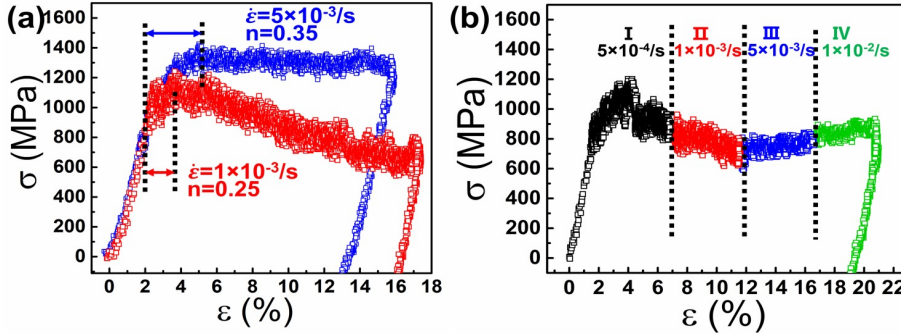


Figure 5.5: In situ micropillar compression tests of FCC (100) Co at different strain rates. (a) At low strain rate ($1 \times 10^{-3}/\text{s}$, red), at high strain rate ($5 \times 10^{-3}/\text{s}$, blue). (b) True stress-true strain curves of jump test at different strain rate ($5 \times 10^{-4}/\text{s}$ - $1 \times 10^{-2}/\text{s}$).

In situ SEM snapshots of micropillars at different strains are shown in Figure 5.6(a) and 5.6(b) for tests carried out at different strain rates. For the micropillar tested at low strain rate, the pillar deforms uniformly (Figure 5.6(a)). Meanwhile, the pillar tested at higher rate (Figure 5.6(b)) shows classical barreling due to friction stress between indenter tip and pillar top surface. No obvious slip bands are observed

in both cases, which will be discussed later.

A jump test was also performed (Figure 5.5(b)) at four different strain rates (5×10^{-4} , 1×10^{-3} , 5×10^{-3} and 1×10^{-2} /s). We found that strain softening occurs at the first two low strain rate regions, followed by strain hardening when strain rate increases to 5×10^{-3} /s or greater. The yield strength of the pillar during the initial jump test is also ~ 700 MPa. The combination of strain softening and strain hardening leads to the surprising V-shape of the true stress-strain curve. In situ SEM snapshots (Figure 5.6c) show that the pillar can sustain strain rate jump tests up to $\sim 20\%$ of strain without any slip bands or failure.

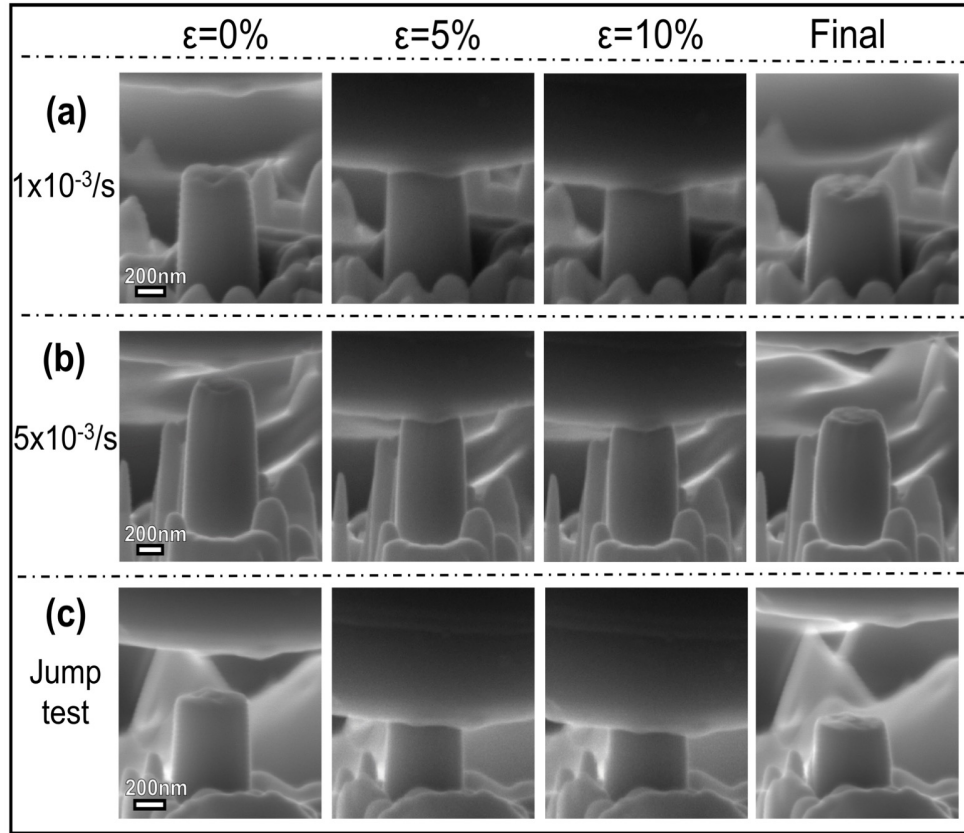


Figure 5.6: SEM images obtained from in situ compression tests of FCC (100) Co pillars at (a) 1×10^{-3} /s and (b) 5×10^{-3} /s strain rates and (c) a jump test with a varying strain rate.

5.5 Discussion

5.5.1 Strengthening and Softening Mechanisms in FCC Co Revealed by MD Simulations

MD simulations show that the deformation in FCC Co is dominated by the activity of partial dislocations. This is possibly due to the low stacking fault energy (SFE) of FCC Co, which is calculated to be -51 mJ/m^2 using the same interatomic potential [97]. The negative SFE value is also predicted by a previous study [226]. Furthermore, MD simulations suggest two types of hardening and softening mechanisms occurring in four regions. The dislocation starvation induced hardening during initial loading in Region I is somewhat surprising as there are preexisting Shockley partials due to the mismatch strain between Cu and FCC Co of $\sim 2\%$. However, these Shockley partials cannot migrate as they are constrained by Hirth locks. MD simulations indeed reveal the shortening of Hirth locks during initial loading, but Shockley partials remain tied to the Hirth Locks. Hardening continues until the avalanche of dislocations due to nucleation of partials and SFs from surface. Such a phenomenon leads to drastic softening in Region II.

The second hardening mechanism revealed by MD is caused by the interception of SFs formed in the previous region and the formation of new Hirth locks at a greater strain level (Region III). Continuous deformation leads to thickening of SF ribbons (HCP laminates) during deformation in region I and II due to nucleation of a significant number of SFs. These HCP laminates as well as SFs play a similar role as TBs or grain boundaries in limiting dislocation mobility and thus contributing to strengthening and work hardening.

The second type of softening mechanisms in Region IV is intriguing. It appears that mobile Shockley partials escape from the interception between certain thin SFs and HCP laminates. These partials migrate along the SF ribbons and lead to the

gradual defaulting of HCP laminate to eventually form a TB. Further migration of Shockley partials along the TB results in the normal motion or migration of the TB along its normal direction. The migration of TBs under deformation of nanotwinned metals has been reported previously [150]. Using MD simulations Li et al. [2] revealed softening in nanotwinned Cu due to the transition from dislocation pile-up mechanisms to partial dominated TB migration in extremely fine (1 nm or less) twinned Cu. Zhu et al. [67] reported the constriction of partials and subsequent absorption (spread) of the full dislocation along TBs in twinned Cu. It is worth mentioning that the second type of softening mechanisms observed here is less drastic compared to the first type of softening, where the avalanche of dislocations occurs.

Finally, we would like to emphasize that even if the hardening and softening observed in regions III and IV in MD simulations are not very significant (limited by the high strain rate characterizing MD simulations), the different atomistic mechanisms that can lead to a hardening or softening response provide qualitative support for the strain rate dependent hardening and softening observed in experiments.

5.5.2 Strain Rate Dependent Deformation Mechanisms in FCC Co with SFs

In this section, we attempt to interpret the strain rate dependent deformation behavior of FCC Co observed in experiments. For the Co pillar tested at low strain rate (1×10^{-3} /s), yield strength is ~ 700 MPa, followed by a transient work hardening stage. Although Hirth Locks in the as-deposited films may be strong barriers for the release of mobile partials, a dislocation starvation dominated hardening mechanism, as predicted by MD simulations, alone may not explain the work hardening observed experimentally, because the specimen dimension is much larger than that used in MD simulation, and it is less likely that all preexisting Shockley partials are constrained by

Hirth locks. The second type of hardening due to blocking of SFs by HCP laminates may be a more realistic work hardening mechanism. It follows that the gradual softening observed at low strain rate may be a consequence of the dissociation of Hirth locks and the activation of abundant partials that glide along SFs.

In fact, in Martinez's study [227], the strength of a Hirth lock is calculated as 0.0032μ , where μ is the shear modulus. For FCC Co, the critical resolved shear stress τ needed to break the Hirth lock is ~ 272 MPa, if we take $\mu = 85$ GPa. When two Shockley partials on different $\{111\}$ planes interact with each other, a $1/3 [002]$ dislocation forms at the junction, then, it dissociates into two Shockley partials $1/6 [1\bar{2}1]$ and $1/6 [\bar{1}21]$. The slip plane and slip direction of the Shockley partials are $\{111\}$ and $\langle 121 \rangle$ respectively. The MD study reveals that the Hirth lock dissociation actually results in the two Shockley partials gliding on the $\{111\}$ plane along the $\langle 121 \rangle$ direction (Figure 5.3(a1)-(a4)). The compressive stress that is needed to break the Hirth lock can hence be calculated by the critical resolved shear stress τ and the Schmid factor

$$\sigma = \frac{\tau}{\cos\Phi\cos\lambda}, \quad (5.1)$$

where Φ is the angle between the slip plane $\{111\}$ and the lateral plane (001) and λ is the angle between the lateral plane (001) and the slip direction $\langle 121 \rangle$. Using this result, the compression stress is calculated to be ~ 1.15 GPa, which is within the stress values observed in the low strain rate compressive test (1×10^{-3} /s) varying between 1 GPa and 1.2 GPa.

MD simulations show that the activation of mobile Shockley partials stems from certain interceptions where Hirth locks did not form. Furthermore, these mobile partials gradually reduce the thickness of SFs via a defaulting process, resulting in a lower density of SF ribbons (HCP laminates). Prior studies show that dislocations

in single crystal pillars or nanowires may exit the free surface [198, 223, 224, 228]. Due to the inability to accumulate internal dislocations, there is a lack of work hardening in these nanowires, and consequently they exhibit either softening or brittle fracture [224, 229]. In sub-micron size single crystal Ni and Al pillars, a similar softening phenomenon has been observed because the dislocation recovery rate exceeds the dislocation nucleation rate [224, 230]. Note that at a low strain rate, despite strain softening, the FCC Co pillar remains uniformly deformed as shown by in situ compression studies. When the strain rate is increased to 5×10^{-3} /s, the micropillar exhibits no strain softening. A prominent strain hardening is observed until the stress reaches a plateau, ~ 1.4 GPa. Plastic yielding occurs at ~ 700 MPa, indicating that the stress necessary to move mobile partials is similar to the pillar deformed at a lower rate. At a higher strain rate, more mobile partial dislocations are nucleated to accommodate plastic deformation. In general, when dislocation nucleation rate is greater than dislocation consumption rate, strain hardening would prevail [230]. In this case, when the density of partial dislocations increases, the chances for Shockley partials to intersect with each other also increase, and thus the probability of forming Hirth locks would also increase.

To test this hypothesis, we performed MD compression simulation at a higher strain rate (1.37×10^9 s). The stress-strain curve for this simulation shown in Figure 5.2(c) reveals a similar trend: two strengthening followed by two softening regions. Dislocation analysis of the two pillars subjected to different stain rates are shown in Figure 5.7(a) and (b). For both cases, we choose the atomistic configurations at the lowest (valley) stress (Figure 5.7(a1) and (b1)) and highest (peak) stress (Figure 5.7(a2) and (b2)) in region III to compare the dislocation structures. We find that the density and number of segments of Hirth locks both increase with increasing stress, which consolidates the role of Hirth locks as a dislocation barrier and their contribution to strain hardening (Figure 5.7(c) and (d)). Additionally, at higher

strain rate, the density and number of segments of Hirth locks are more than two times greater than those at lower strain rate. This analysis also verifies our hypothesis that a higher strain rate increases the number of Hirth locks, hence promotes strain hardening. Finally, macroscopically, when dislocation nucleation and recovery rates reach a balance, the flow stress is maintained at ~ 1.4 GPa. Foregoing interpretation also works well for the experimental compressive jump test performed at various strain rates (Figure 5.5(b)), which leads to a unique V-shape stress-strain curve. The pillar tested during the jump tests also deformed uniformly up to $\sim 20\%$ strain (Figure 5.6(c)).

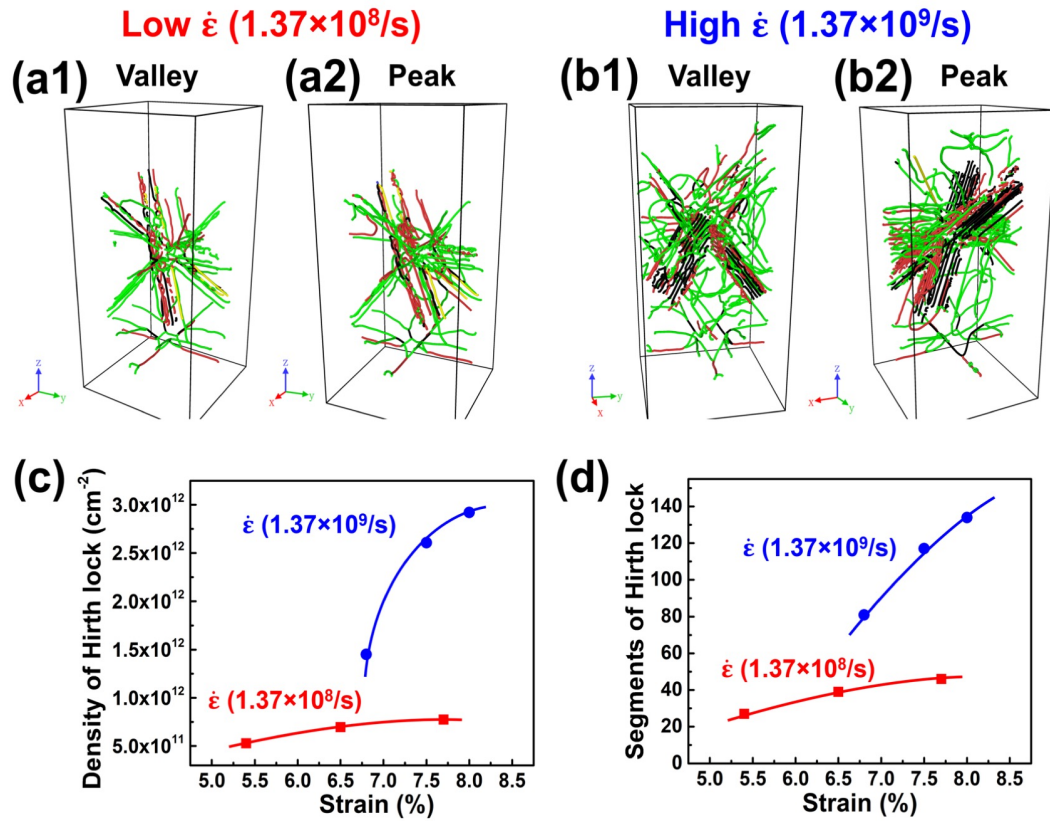


Figure 5.7: Dislocation analysis of MD simulations at the valley and peak of Region III on both stress-strain curves of relatively (a) low (1.37×10^8 /s) and (b) high (1.37×10^9 /s) strain rates. The density (c) and number (d) of Hirth locks function of the strain at low and high strain rates.

In general, FCC single crystal pillars with submicron pillar size, such as Au [198], Cu [231, 232], Ni [224] and Al [229], often experience intermittent strain bursts or serrated yielding during deformation. This plastic instability is an intrinsic characteristic of micrometer size single crystal metals, due to dislocation avalanches. However, instead of intermittent strain burst, single crystal FCC Co with high-density intersecting SFs exhibits significant work hardening and smooth stress-strain curve. The inclined SF ribbons (HCP laminates) block the transmission of partial dislocations and prohibit the formation of dislocation avalanches, which could only be accomplished previously by increasing pillar size in single crystal FCC metals [231, 233]. Moreover, in contrast to the uniform deformation at low strain rate, in situ micropillar compression tests show barreling at a higher strain rate, which is a manifestation of strain hardening in FCC Co due to the formation of a greater density of dislocations and Hirth locks inside pillar as suggested by MD simulations discussed before.

5.6 Conclusion

In summary, we report an intriguing SF dominated deformation mechanism, which is also sensitive to strain rate in single crystal FCC Co (100) pillar. The phenomenon of strain softening at low strain rate arises from insufficient density of intersections or Hirth locks that are effective barriers for dislocation and partial migration and the propagation of partials along SF ribbons. In contrast, at higher strain rate, abundant Hirth locks and SF intersections can effectively inhibit the migration of partials, leading to substantial work hardening. The smooth stress-strain curve and homogenous morphology variation associated with the deformed pillars indicate that SFs can also prohibit strain burst and enhance plasticity. MD simulations furnish atomistic insights into the possible SF-mediated deformation mechanisms at play

and provide support for the contribution of SF ribbons (HCP laminates) and Hirth locks to strain hardening and SF dominated plasticity. The conclusions derived from the combination of experimental and computational studies may stimulate significant interest in the stacking-fault dominated strengthening and plasticity in metallic materials.

Chapter 6

SUMMARY

In this chapter, we summarize our study of deformation mechanisms in HCP and FCC metals and nanostructured metallic multilayers dominated by the evolution and interactions of different types of planar defects and interfaces and present directions for further studies. In Chapter 2, we investigate an intriguing deformation mechanism in HCP Co dominated by phase transformation. In fact, HCP Co with high density SFs exhibits both high strength and ductility as revealed by MD compression simulations and in situ SEM compression tests. MD simulations reveal that HCP-to-FCC phase transformation occurs during deformation due to partial dislocations gliding along the pre-existing SFs parallel to the basal plane during compression. The subsequent generation of inclined SFs on (111) planes in FCC Co plays a key role in accommodating plasticity. We prove by this study that introducing a high density of SFs provides a method of designing high-strength, deformable HCP materials, traditionally lacking independent slip system required to satisfy the Von Mises criterion. This study is performed at 300 K and it would be insightful to determine the effect of temperature on the mechanical behavior and deformation mechanisms in HCP Co with pre-existing SFs, especially nearing its transition temperature of $\sim 700\text{K}$, beyond which Co is stable in an FCC structure. This work was published in

Scripta Materialia in 2019 [165].

In Chapter 3, we report on drastically different mechanical strength and deformability of Cu/Co multilayers with three crystallographic orientations and layer interfaces. The coherent interfaces of FCC (100) and (110) Cu/Co are found to be weak barriers to dislocations and formation of slip bands. (110) Cu/Co exhibit a higher flow stress owing to TBs that inhibit dislocation motion leading to hardening. Nevertheless, a defect network consisting of TBs, SFs and parallel incoherent layer interfaces give FCC/HCP (111)Cu/(0002)Co multilayers their high strength. At the onset of plastic yield, HCP to FCC phase transformation in Co occurs. The coherent interfaces of FCC (100) and (110) Cu/Co lead to a low yield strength and slip bands during in-situ micropillar compression tests. Alternatively, the incoherent interfaces in Cu (111)/Co (0002) multilayer system delivers high yield strength and flow stress. In addition, the formation of a cap layer proves local superplastic deformation. This work was published in Acta Materialia in 2020 [217].

The unprecedented mechanical response of (111)Cu/(0002)Co mediated by a synergistic defect network motivates the study in Chapter 4. In fact, MD compression simulations on (111)Cu/(0002)Co nanopillars with different nanostructures were performed in an attempt to determine the individual effect of each of the three planar defects, TBs in Cu, SFs in Co and Cu-Co interface, on the mechanical response of (111)Cu/(0002)Co. The incoherent HCP Co-FCC Cu interface obstructs dislocation motion across layers leading to high strength. On the other hand, TBs in Cu play two roles. They inhibit movement of partials across the Cu layer contributing to high yield strength. Second, the glide of dislocations along the CTBs triggers detwinning and the dislocation pile-up contributes to the high localization of stress that activates HCP to FCC transformation, turning the Cu-Co interface into a coherent one, transparent to partial dislocations motion thereby accommodating plasticity and ensuring co-deformation of Cu and Co. Finally, the high strength of HCP Co layers is owed to SFs

on the basal planes prohibiting slip on prismatic and pyramidal systems. In addition, a higher density of SFs contributes to plasticity by increasing the localized stress around Cu-Co interfaces, hence, easing the HCP to FCC phase transformation. These results are also reflected on the mechanical response of (111)Cu/(0002)Co multilayers with different layer thicknesses undergoing in situ micropillar compression. The difference in layer thickness resulted in different microstructures. The compression tests show that 25 nm is the optimal layer thickness for high strength and deformability. Cu/Co 5 nm pillars are much softer than 25 nm pillars due to coherent Cu/Co interfaces. When the layer thickness increases to 100 nm, the low density of pre-existing TBs in Cu layers compromises their strength, limiting the deformation to Cu layers, therefore, they're extruded during compression similar to the MD results of the nanopillar with no TBs in Cu, with Co layers remaining undeformed. Therefore, the three parallel planar defects with a high density of TBs in Cu and SFs in Co are necessary to impart an attractive combination of high strength and plasticity.

Finally, we investigate an intriguing SF dominated deformation mechanism in single crystal FCC Co (100) pillar in Chapter 5. We show that the insufficient density of SF intersections or Hirth locks constituting effective barriers for dislocation and partial migration leads to strain softening at low strain rate. In contrast, at higher strain rate, abundant Hirth locks and SF intersections inhibit the migration of partials effectively, leading to substantial work hardening. MD simulations provide atomistic insights into the possible deformation mechanisms governed by SF activity and provide support for the contribution of SF ribbons (HCP laminates) and Hirth locks to strain hardening and SF dominated plasticity. The conclusions derived from this study highlight the possible SF-mediated strengthening and plasticity in metallic materials. This study also includes a strain rate sensitivity assessment of the density of Hirth locks, hence, on hardening. However, the MD method limits us to very high strain rates of about $\sim 10^8 - 10^9$ /s compare to experimental strain rates of

$\sim 10^{-3}$ /s which only allows a qualitative comparison of the strain rate sensitivity. To circumvent the timescale bottleneck of traditional MD, novel time-scaling approaches such as the Autonomous Basin Climbing method can be used and is proven to yield useful information and novel insights into the rate-dependent mechanical behavior for materials science problems of interest, when appropriately complemented with other algorithms and techniques. This study was published in *Materials Science and Engineering:A* in 2018 [144].

In essence, the studies detailed throughout this dissertation provide novel methods of improving the conflicting strength and plasticity of metallic materials and multilayers with pre-existing SFs by harnessing a variety of planar defects such as TBs, SFs and layers interfaces and their interactions. However, other aspects of SFs are yet to be explored.

For instance, the fracture behavior and creep mechanisms of FCC and HCP metals with pre-existing SFs are still not clear. Studying the reaction of SFs to crack propagation and their role in creep mechanisms would be of interest.

Structural materials are a good candidate for nuclear power systems with high radiation tolerance, since GBs, layer interfaces and free surfaces have been shown to improve radiation resistance. TBs interactions with radiation-induced point defects have also been studied extensively. Our current study provides avenues for investigating the role of pre-existing stacking faults in radiation tolerance in metallic materials. Furthermore, the combination of three types of planar defects in (111)Cu/(0002)Co presents an opportunity to study radiation tolerance of metallic multilayers with a variety of pre-existing defects.

REFERENCES

- [1] J. R. Greer, “Nanotwinned metals: It’s all about imperfections,” *Nature materials*, vol. 12, no. 8, pp. 689–690, 2013.
- [2] X. Li, Y. Wei, L. Lu, K. Lu, and H. Gao, “Dislocation nucleation governed softening and maximum strength in nano-twinned metals,” *Nature*, vol. 464, no. 7290, p. 877, 2010.
- [3] Z. Zhang, D. E. Eakins, and F. P. Dunne, “On the formation of adiabatic shear bands in textured hcp polycrystals,” *International Journal of Plasticity*, vol. 79, pp. 196–216, 2016.
- [4] M. H. Anazi and H. M. Zbib, “A continuum deformation model for steel coated with nanolaminate metallic systems,” *Metallurgical and Materials Transactions A*, vol. 49, no. 12, pp. 6093–6109, 2018.
- [5] M. Schneider, E. George, T. Manescau, T. Zálezák, J. Hunfeld, A. Dlouhý, G. Eggeler, and G. Laplanche, “Analysis of strengthening due to grain boundaries and annealing twin boundaries in the crconi medium-entropy alloy,” *International Journal of Plasticity*, vol. 124, pp. 155–169, 2020.
- [6] A. Rooney, Z. Li, W. Zhao, A. Gholinia, A. Kozikov, G. Auton, F. Ding, R. Gorbachev, R. Young, and S. Haigh, “Anomalous twin boundaries in two dimensional materials,” *Nature communications*, vol. 9, no. 1, pp. 1–7, 2018.

- [7] D. Jang, X. Li, H. Gao, and J. R. Greer, “Deformation mechanisms in nanotwinned metal nanopillars,” *Nature nanotechnology*, vol. 7, no. 9, p. 594, 2012.
- [8] Z. Cheng, H. Zhou, Q. Lu, H. Gao, and L. Lu, “Extra strengthening and work hardening in gradient nanotwinned metals,” *Science*, vol. 362, no. 6414, p. eaau1925, 2018.
- [9] Y. Chen, K. Y. Yu, Y. Liu, S. Shao, H. Wang, M. Kirk, J. Wang, and X. Zhang, “Damage-tolerant nanotwinned metals with nanovoids under radiation environments,” *Nature communications*, vol. 6, no. 1, pp. 1–8, 2015.
- [10] R. Raj and M. Ashby, “On grain boundary sliding and diffusional creep,” *Metallurgical transactions*, vol. 2, no. 4, pp. 1113–1127, 1971.
- [11] J. Hu, Y. Shi, X. Sauvage, G. Sha, and K. Lu, “Grain boundary stability governs hardening and softening in extremely fine nanograined metals,” *Science*, vol. 355, no. 6331, pp. 1292–1296, 2017.
- [12] Y. Zhang, G. J. Tucker, and J. R. Trelewicz, “Stress-assisted grain growth in nanocrystalline metals: Grain boundary mediated mechanisms and stabilization through alloying,” *Acta Materialia*, vol. 131, pp. 39–47, 2017.
- [13] V. Chuvil’deev and V. Kopylov, “Theory of nonequilibrium grain boundaries and its applications to describe ultrafine-grained metals and alloys produced by ecap,” 2017.
- [14] S. Ratanaphan, T. Boonkird, R. Sarochawikasit, H. Beladi, K. Barmak, and G. S. Rohrer, “Atomistic simulations of grain boundary energies in tungsten,” *Materials Letters*, vol. 186, pp. 116–118, 2017.

- [15] T. Frolov, Q. Zhu, T. Ooppelstrup, J. Marian, and R. E. Rudd, "Structures and transitions in bcc tungsten grain boundaries and their role in the absorption of point defects," *Acta Materialia*, vol. 159, pp. 123–134, 2018.
- [16] S. Peng, M. Wang, H. Yang, L. Zeng, J. Nan, J. Zhou, Y. Zhang, A. Hallal, M. Chshiev, K. L. Wang, Q. Zhang, and W. Zhao, "Origin of interfacial perpendicular magnetic anisotropy in mgo/cofe/metallic capping layer structures," *Scientific reports*, vol. 5, p. 18173, 2015.
- [17] S. Shao and S. Medyanik, "Interaction of dislocations with incoherent interfaces in nanoscale fcc–bcc metallic bi-layers," *Modelling and Simulation in Materials Science and Engineering*, vol. 18, no. 5, p. 055010, 2010.
- [18] A. Misra, J. Hirth, and H. Kung, "Single-dislocation-based strengthening mechanisms in nanoscale metallic multilayers," *Philosophical Magazine A*, vol. 82, no. 16, pp. 2935–2951, 2002.
- [19] Q. Zhou, P. Huang, M. Liu, F. Wang, K. Xu, and T. Lu, "Grain and interface boundaries governed strengthening mechanisms in metallic multilayers," *Journal of Alloys and Compounds*, vol. 698, pp. 906–912, 2017.
- [20] L. Lu, C. Huang, W. Pi, H. Xiang, F. Gao, T. Fu, and X. Peng, "Molecular dynamics simulation of effects of interface imperfections and modulation periods on cu/ta multilayers," *Computational Materials Science*, vol. 143, pp. 63–70, 2018.
- [21] L. Lu, Y. Shen, X. Chen, L. Qian, and K. Lu, "Ultrahigh strength and high electrical conductivity in copper," *Science*, vol. 304, no. 5669, pp. 422–426, 2004.
- [22] N. Li, J. Wang, A. Misra, X. Zhang, J. Huang, and J. Hirth, "Twinning dislocation multiplication at a coherent twin boundary," *Acta Materialia*, vol. 59, no. 15, pp. 5989–5996, 2011.

- [23] M. Ardeljan, I. J. Beyerlein, and M. Knezevic, “Effect of dislocation density-twin interactions on twin growth in az31 as revealed by explicit crystal plasticity finite element modeling,” *International Journal of Plasticity*, vol. 99, pp. 81–101, 2017.
- [24] Z. Zeng, X. Li, L. Lu, and T. Zhu, “Fracture in a thin film of nanotwinned copper,” *Acta Materialia*, vol. 98, pp. 313–317, 2015.
- [25] J. Wang and H. Huang, “Shockley partial dislocations to twin: another formation mechanism and generic driving force,” *Applied physics letters*, vol. 85, no. 24, pp. 5983–5985, 2004.
- [26] Z.-H. Jin, P. Gumbsch, E. Ma, K. Albe, K. Lu, H. Hahn, and H. Gleiter, “The interaction mechanism of screw dislocations with coherent twin boundaries in different face-centred cubic metals,” *Scripta Materialia*, vol. 54, no. 6, pp. 1163–1168, 2006.
- [27] A. Cao, Y. Wei, and S. X. Mao, “Deformation mechanisms of face-centered-cubic metal nanowires with twin boundaries,” *Applied physics letters*, vol. 90, no. 15, p. 151909, 2007.
- [28] C. Deng and F. Sansoz, “Enabling ultrahigh plastic flow and work hardening in twinned gold nanowires,” *Nano letters*, vol. 9, no. 4, pp. 1517–1522, 2009.
- [29] J. Wang and X. Zhang, “Twinning effects on strength and plasticity of metallic materials,” *Mrs Bulletin*, vol. 41, no. 4, pp. 274–281, 2016.
- [30] H. Wang, P. Wu, J. Wang, and C. Tomé, “A crystal plasticity model for hexagonal close packed (hcp) crystals including twinning and de-twinning mechanisms,” *International Journal of Plasticity*, vol. 49, pp. 36–52, 2013.

- [31] D. Brown, I. Beyerlein, T. Sisneros, B. Clausen, and C. Tomé, “Role of twinning and slip during compressive deformation of beryllium as a function of strain rate,” *International Journal of Plasticity*, vol. 29, pp. 120–135, 2012.
- [32] S. R. Niezgoda, A. K. Kanjarla, I. J. Beyerlein, and C. N. Tomé, “Stochastic modeling of twin nucleation in polycrystals: an application in hexagonal close-packed metals,” *International journal of plasticity*, vol. 56, pp. 119–138, 2014.
- [33] G. J. Tucker and S. M. Foiles, “Quantifying the influence of twin boundaries on the deformation of nanocrystalline copper using atomistic simulations,” *International Journal of Plasticity*, vol. 65, pp. 191–205, 2015.
- [34] P. Chowdhury, H. Sehitoglu, H. Maier, and R. Rateick, “Strength prediction in nico alloys—the role of composition and nanotwins,” *International Journal of Plasticity*, vol. 79, pp. 237–258, 2016.
- [35] X. Xiao, D. Song, H. Chu, J. Xue, and H. Duan, “Mechanical behaviors of irradiated fcc polycrystals with nanotwins,” *International Journal of Plasticity*, vol. 74, pp. 110–126, 2015.
- [36] Y. Liu, N. Li, D. Bufford, J. Lee, J. Wang, H. Wang, and X. Zhang, “In situ nanoindentation studies on detwinning and work hardening in nanotwinned monolithic metals,” *Jom*, vol. 68, no. 1, pp. 127–135, 2016.
- [37] H. Zhou, X. Li, S. Qu, W. Yang, and H. Gao, “A jogged dislocation governed strengthening mechanism in nanotwinned metals,” *Nano letters*, vol. 14, no. 9, pp. 5075–5080, 2014.
- [38] Y. M. Wang, F. Sansoz, T. LaGrange, R. T. Ott, J. Marian, T. W. Barbee Jr, and A. V. Hamza, “Defective twin boundaries in nanotwinned metals,” *Nature Materials*, vol. 12, no. 8, p. 697, 2013.

- [39] X. Zhang, E. Fu, N. Li, A. Misra, Y.-Q. Wang, L. Shao, and H. Wang, “Design of radiation tolerant nanostructured metallic multilayers,” *Journal of engineering materials and technology*, vol. 134, no. 4, 2012.
- [40] X. Zhang, E. Fu, A. Misra, and M. Demkowicz, “Interface-enabled defect reduction in he ion irradiated metallic multilayers,” *Jom*, vol. 62, no. 12, pp. 75–78, 2010.
- [41] T. Höchbauer, A. Misra, K. Hattar, and R. Hoagland, “Influence of interfaces on the storage of ion-implanted he in multilayered metallic composites,” *Journal of applied physics*, vol. 98, no. 12, p. 123516, 2005.
- [42] M. Zhernenkov, S. Gill, V. Stanic, E. DiMasi, K. Kisslinger, J. K. Baldwin, A. Misra, M. Demkowicz, and L. Ecker, “Design of radiation resistant metallic multilayers for advanced nuclear systems,” *Applied Physics Letters*, vol. 104, no. 24, p. 241906, 2014.
- [43] Y. Chen, E. Fu, K. Yu, M. Song, Y. Liu, Y. Wang, H. Wang, and X. Zhang, “Enhanced radiation tolerance in immiscible cu/fe multilayers with coherent and incoherent layer interfaces,” *Journal of Materials Research*, vol. 30, no. 9, pp. 1300–1309, 2015.
- [44] E. Y. Chen, C. Deo, and R. Dingreville, “Irradiation resistance of nanostructured interfaces in zr-nb metallic multilayers,” *Journal of Materials Research*, vol. 34, no. 13, pp. 2239–2251, 2019.
- [45] D. Hull and D. J. Bacon, *Introduction to dislocations*, vol. 37. Elsevier, 2011.
- [46] R. Smallman and K. Westmacott, “Stacking faults in face-centred cubic metals and alloys,” *Philosophical magazine*, vol. 2, no. 17, pp. 669–683, 1957.

- [47] J. Zhang, Z. Leng, S. Liu, J. Li, M. Zhang, and R. Wu, "Microstructure and mechanical properties of mg-gd-dy-zn alloy with long period stacking ordered structure or stacking faults," *Journal of alloys and compounds*, vol. 509, no. 29, pp. 7717–7722, 2011.
- [48] J. Schiøtz, T. Vegge, F. Di Tolla, and K. W. Jacobsen, "Atomic-scale simulations of the mechanical deformation of nanocrystalline metals," *Physical Review B*, vol. 60, no. 17, p. 11971, 1999.
- [49] X. Zhou, X. Li, and K. Lu, "Size dependence of grain boundary migration in metals under mechanical loading," *Physical review letters*, vol. 122, no. 12, p. 126101, 2019.
- [50] Y. Liu, Y. Chen, K. Yu, H. Wang, J. Chen, and X. Zhang, "Stacking fault and partial dislocation dominated strengthening mechanisms in highly textured cu/co multilayers," *International Journal of Plasticity*, vol. 49, pp. 152–163, 2013.
- [51] H. Gleiter, "Nanostructured materials: basic concepts and microstructure," *Acta materialia*, vol. 48, no. 1, pp. 1–29, 2000.
- [52] C. Suryanarayana and C. Koch, "Nanocrystalline materials—current research and future directions," *Hyperfine Interactions*, vol. 130, no. 1-4, p. 5, 2000.
- [53] T. Hanlon, Y.-N. Kwon, and S. Suresh, "Grain size effects on the fatigue response of nanocrystalline metals," *Scripta Materialia*, vol. 49, no. 7, pp. 675–680, 2003.
- [54] M. A. Meyers, A. Mishra, and D. J. Benson, "Mechanical properties of nanocrystalline materials," *Progress in materials science*, vol. 51, no. 4, pp. 427–556, 2006.

- [55] V. Yamakov, D. Wolf, S. R. Phillpot, A. K. Mukherjee, and H. Gleiter, “Dislocation processes in the deformation of nanocrystalline aluminium by molecular-dynamics simulation,” *Nature materials*, vol. 1, no. 1, pp. 45–49, 2002.
- [56] A. v. Hasnaoui, H. Van Swygenhoven, and P. Derlet, “On non-equilibrium grain boundaries and their effect on thermal and mechanical behaviour: a molecular dynamics computer simulation,” *Acta Materialia*, vol. 50, no. 15, pp. 3927–3939, 2002.
- [57] A. Frøseth, P. Derlet, and H. Van Swygenhoven, “Grown-in twin boundaries affecting deformation mechanisms in nc-metals,” *Applied Physics Letters*, vol. 85, no. 24, pp. 5863–5865, 2004.
- [58] A. Cao and Y. Wei, “Molecular dynamics simulation of plastic deformation of nanotwinned copper,” *Journal of Applied Physics*, vol. 102, no. 8, p. 083511, 2007.
- [59] A. Cao, Y. Wei, and E. Ma, “Grain boundary effects on plastic deformation and fracture mechanisms in cu nanowires: Molecular dynamics simulations,” *Physical Review B*, vol. 77, no. 19, p. 195429, 2008.
- [60] G. J. Tucker and D. L. McDowell, “Non-equilibrium grain boundary structure and inelastic deformation using atomistic simulations,” *International Journal of Plasticity*, vol. 27, no. 6, pp. 841–857, 2011.
- [61] T. Zhu and H. Gao, “Plastic deformation mechanism in nanotwinned metals: An insight from molecular dynamics and mechanistic modeling,” *Scripta Materialia*, vol. 66, no. 11, pp. 843–848, 2012.
- [62] H. Song, Y. Li, and M. An, “Atomic simulations of the effect of twist grain

- boundaries on deformation behavior of nanocrystalline copper,” *Computational materials science*, vol. 84, pp. 40–44, 2014.
- [63] L. Lu, R. Schwaiger, Z. Shan, M. Dao, K. Lu, and S. Suresh, “Nano-sized twins induce high rate sensitivity of flow stress in pure copper,” *Acta materialia*, vol. 53, no. 7, pp. 2169–2179, 2005.
- [64] M. Dao, L. Lu, Y. Shen, and S. Suresh, “Strength, strain-rate sensitivity and ductility of copper with nanoscale twins,” *Acta materialia*, vol. 54, no. 20, pp. 5421–5432, 2006.
- [65] Y. Shen, L. Lu, Q. Lu, Z. Jin, and K. Lu, “Tensile properties of copper with nano-scale twins,” *Scripta Materialia*, vol. 52, no. 10, pp. 989–994, 2005.
- [66] Z.-H. Jin, P. Gumbsch, K. Albe, E. Ma, K. Lu, H. Gleiter, and H. Hahn, “Interactions between non-screw lattice dislocations and coherent twin boundaries in face-centered cubic metals,” *Acta Materialia*, vol. 56, no. 5, pp. 1126–1135, 2008.
- [67] T. Zhu, J. Li, A. Samanta, H. G. Kim, and S. Suresh, “Interfacial plasticity governs strain rate sensitivity and ductility in nanostructured metals,” *Proceedings of the National Academy of Sciences*, vol. 104, no. 9, pp. 3031–3036, 2007.
- [68] Z. Wu, Y. Zhang, and D. Srolovitz, “Dislocation–twin interaction mechanisms for ultrahigh strength and ductility in nanotwinned metals,” *Acta Materialia*, vol. 57, no. 15, pp. 4508–4518, 2009.
- [69] I. Shabib and R. E. Miller, “Deformation characteristics and stress–strain response of nanotwinned copper via molecular dynamics simulation,” *Acta Materialia*, vol. 57, no. 15, pp. 4364–4373, 2009.

- [70] C. Huang, X. Peng, T. Fu, X. Chen, H. Xiang, Q. Li, and N. Hu, “Molecular dynamics simulation of bcc ta with coherent twin boundaries under nanoindentation,” *Materials Science and Engineering: A*, vol. 700, pp. 609–616, 2017.
- [71] X. Wu, Y. Zhu, M. Chen, and E. Ma, “Twinning and stacking fault formation during tensile deformation of nanocrystalline ni,” *Scripta Materialia*, vol. 54, no. 9, pp. 1685–1690, 2006.
- [72] J. Schiøtz, F. D. Di Tolla, and K. W. Jacobsen, “Softening of nanocrystalline metals at very small grain sizes,” *Nature*, vol. 391, no. 6667, pp. 561–563, 1998.
- [73] A. Wagih and M. Shaat, “The dependence of accumulative roll bonded copper mechanical properties on grain sub-division, stacking faults, and lattice strains,” *Materials Science and Engineering: A*, vol. 756, pp. 190–197, 2019.
- [74] X. Zhang, B. Li, and Q. Liu, “Non-equilibrium basal stacking faults in hexagonal close-packed metals,” *Acta Materialia*, vol. 90, pp. 140–150, 2015.
- [75] S. Cheng, J. Spencer, and W. Milligan, “Strength and tension/compression asymmetry in nanostructured and ultrafine-grain metals,” *Acta Materialia*, vol. 51, no. 15, pp. 4505–4518, 2003.
- [76] Z. You, X. Li, L. Gui, Q. Lu, T. Zhu, H. Gao, and L. Lu, “Plastic anisotropy and associated deformation mechanisms in nanotwinned metals,” *Acta Materialia*, vol. 61, no. 1, pp. 217–227, 2013.
- [77] G. I. Taylor and H. Quinney, “The plastic distortion of metals,” *Philosophical Transactions of the Royal Society of London. Series A, Containing Papers of a Mathematical or Physical Character*, vol. 230, no. 681-693, pp. 323–362, 1931.

- [78] R. v. Mises, “Mechanik der plastischen formänderung von kristallen,” *ZAMM-Journal of Applied Mathematics and Mechanics/Zeitschrift für Angewandte Mathematik und Mechanik*, vol. 8, no. 3, pp. 161–185, 1928.
- [79] M. An, Q. Deng, Y. Li, H. Song, M. Su, and J. Cai, “Molecular dynamics study of tension-compression asymmetry of nanocrystal α -ti with stacking fault,” *Materials & Design*, vol. 127, pp. 204–214, 2017.
- [80] H. Song and Y. Li, “Effect of stacking fault and temperature on deformation behaviors of nanocrystalline mg,” *Journal of Applied Physics*, vol. 112, no. 5, p. 054322, 2012.
- [81] H. Wei and Y. Wei, “Interaction between a screw dislocation and stacking faults in fcc metals,” *Materials Science and Engineering: A*, vol. 541, pp. 38–44, 2012.
- [82] L. Zhang, C. Lu, G. Michal, G. Deng, and K. Tieu, “The formation and destruction of stacking fault tetrahedron in fcc metals: A molecular dynamics study,” *Scripta Materialia*, vol. 136, pp. 78–82, 2017.
- [83] J. W. Wang, S. Narayanan, J. Y. Huang, Z. Zhang, T. Zhu, and S. X. Mao, “Atomic-scale dynamic process of deformation-induced stacking fault tetrahedra in gold nanocrystals,” *Nature communications*, vol. 4, no. 1, pp. 1–8, 2013.
- [84] P. Wang, S. Xu, J. Liu, X. Li, Y. Wei, H. Wang, H. Gao, and W. Yang, “New insights on stacking fault behavior in twin induced plasticity from meta-atom molecular dynamics simulations,” *arXiv preprint arXiv:1604.00579*, 2016.
- [85] A. Rohatgi, K. S. Vecchio, and G. T. Gray, “The influence of stacking fault energy on the mechanical behavior of cu and cu-al alloys: deformation twinning, work hardening, and dynamic recovery,” *Metallurgical and Materials Transactions A*, vol. 32, no. 1, pp. 135–145, 2001.

- [86] K. Youssef, M. Sakaliyska, H. Bahmanpour, R. Scattergood, and C. Koch, "Effect of stacking fault energy on mechanical behavior of bulk nanocrystalline cu and cu alloys," *Acta materialia*, vol. 59, no. 14, pp. 5758–5764, 2011.
- [87] P.-L. Sun, Y. Zhao, J. Cooley, M. Kassner, Z. Horita, T. Langdon, E. Lavernia, and Y. Zhu, "Effect of stacking fault energy on strength and ductility of nanostructured alloys: An evaluation with minimum solution hardening," *Materials Science and Engineering: A*, vol. 525, no. 1-2, pp. 83–86, 2009.
- [88] Y. Zhao, Y. Zhu, X. Liao, Z. Horita, and T. Langdon, "Tailoring stacking fault energy for high ductility and high strength in ultrafine grained cu and its alloy," *Applied physics letters*, vol. 89, no. 12, p. 121906, 2006.
- [89] X. Wu, X. San, X. Liang, Y. Gong, and X. Zhu, "Effect of stacking fault energy on mechanical behavior of cold-forging cu and cu alloys," *Materials & Design*, vol. 47, pp. 372–376, 2013.
- [90] Y. Zhao, X. Liao, Z. Horita, T. Langdon, and Y. Zhu, "Determining the optimal stacking fault energy for achieving high ductility in ultrafine-grained cu–zn alloys," *Materials Science and Engineering: A*, vol. 493, no. 1-2, pp. 123–129, 2008.
- [91] R. Kumar, S. Dasharath, P. Kang, C. C. Koch, and S. Mula, "Enhancement of mechanical properties of low stacking fault energy brass processed by cryorolling followed by short-annealing," *Materials & Design*, vol. 67, pp. 637–643, 2015.
- [92] J. Li, Y. Chen, S. Xue, H. Wang, and X. Zhang, "Comparison of size dependent strengthening mechanisms in ag/fe and ag/ni multilayers," *Acta Materialia*, vol. 114, pp. 154–163, 2016.
- [93] I. Knorr, N. Cordero, E. T. Lilleodden, and C. A. Volkert, "Mechanical behavior

- of nanoscale cu/pdsi multilayers,” *Acta materialia*, vol. 61, no. 13, pp. 4984–4995, 2013.
- [94] D. Bufford, Z. Bi, Q. Jia, H. Wang, and X. Zhang, “Nanotwins and stacking faults in high-strength epitaxial ag/al multilayer films,” *Applied Physics Letters*, vol. 101, no. 22, p. 223112, 2012.
- [95] J. Wang and A. Misra, “An overview of interface-dominated deformation mechanisms in metallic multilayers,” *Current Opinion in Solid State and Materials Science*, vol. 15, no. 1, pp. 20–28, 2011.
- [96] J. Zhang, X. Zhang, R. Wang, S. Lei, P. Zhang, J. Niu, G. Liu, G. Zhang, and J. Sun, “Length-scale-dependent deformation and fracture behavior of cu/x (x= nb, zr) multilayers: The constraining effects of the ductile phase on the brittle phase,” *Acta Materialia*, vol. 59, no. 19, pp. 7368–7379, 2011.
- [97] X. Zhou, R. Johnson, and H. Wadley, “Misfit-energy-increasing dislocations in vapor-deposited cofe/nife multilayers,” *Physical Review B*, vol. 69, no. 14, p. 144113, 2004.
- [98] J. Wang, R. Hoagland, J. Hirth, and A. Misra, “Atomistic simulations of the shear strength and sliding mechanisms of copper–niobium interfaces,” *Acta materialia*, vol. 56, no. 13, pp. 3109–3119, 2008.
- [99] N. Mara, D. Bhattacharyya, P. Dickerson, R. Hoagland, and A. Misra, “Deformability of ultrahigh strength 5 nm cu/ nb nanolayered composites,” *Applied Physics Letters*, vol. 92, no. 23, p. 231901, 2008.
- [100] A. Misra, X. Zhang, D. Hammon, and R. Hoagland, “Work hardening in rolled nanolayered metallic composites,” *Acta Materialia*, vol. 53, no. 1, pp. 221–226, 2005.

- [101] A. Misra, M. Verdier, Y. Lu, H. Kung, T. Mitchell, M. Nastasi, and J. Embury, "Structure and mechanical properties of cu-x (x= nb, cr, ni) nanolayered composites," *Scripta Materialia*, vol. 39, no. 4-5, pp. 555–560, 1998.
- [102] G. Was and T. Foecke, "Deformation and fracture in microlaminates," *Thin Solid Films*, vol. 286, no. 1-2, pp. 1–31, 1996.
- [103] S. A. Barnett and M. Shinn, "Plastic and elastic properties of compositionally modulated thin films," *Annual Review of Materials Science*, vol. 24, no. 1, pp. 481–511, 1994.
- [104] J. Koehler, "Attempt to design a strong solid," *Physical review B*, vol. 2, no. 2, p. 547, 1970.
- [105] N. Petch, "The cleavage strength of polycrystals," *Journal of the Iron and Steel Institute*, vol. 174, pp. 25–28, 1953.
- [106] H. M. Zbib, C. T. Overman, F. Akasheh, and D. Bahr, "Analysis of plastic deformation in nanoscale metallic multilayers with coherent and incoherent interfaces," *International Journal of Plasticity*, vol. 27, no. 10, pp. 1618–1639, 2011.
- [107] S. N. Medyanik and S. Shao, "Strengthening effects of coherent interfaces in nanoscale metallic bilayers," *Computational materials science*, vol. 45, no. 4, pp. 1129–1133, 2009.
- [108] S. Rao, P. Hazzledine, and D. Dimiduk, "Interfacial strengthening in semi-coherent metallic multilayers," *MRS Online Proceedings Library Archive*, vol. 362, 1994.
- [109] R. Hoagland, T. Mitchell, J. Hirth, and H. Kung, "On the strengthening effects

- of interfaces in multilayer fee metallic composites,” *Philosophical magazine A*, vol. 82, no. 4, pp. 643–664, 2002.
- [110] S. Weng, H. Ning, N. Hu, C. Yan, T. Fu, X. Peng, S. Fu, J. Zhang, C. Xu, D. Sun, Y. Liu, and L. Wu, “Strengthening effects of twin interface in cu/ni multilayer thin films—a molecular dynamics study,” *Materials & Design*, vol. 111, pp. 1–8, 2016.
- [111] M. Phillips, B. Clemens, and W. Nix, “A model for dislocation behavior during deformation of al/al₃sc (fcc/l12) metallic multilayers,” *Acta materialia*, vol. 51, no. 11, pp. 3157–3170, 2003.
- [112] J. Wang, R. G. Hoagland, and A. Misra, “Mechanics of nanoscale metallic multilayers: From atomic-scale to micro-scale,” *Scripta materialia*, vol. 60, no. 12, pp. 1067–1072, 2009.
- [113] Z. Xie, M. Hoffman, P. Munroe, A. Bendavid, Martin, and PJ, “Deformation mechanisms of tin multilayer coatings alternated by ductile or stiff interlayers,” *Acta Materialia*, vol. 56, no. 4, pp. 852–861, 2008.
- [114] A. Misra, J. Hirth, and R. Hoagland, “Length-scale-dependent deformation mechanisms in incoherent metallic multilayered composites,” *Acta materialia*, vol. 53, no. 18, pp. 4817–4824, 2005.
- [115] Q. Zhou, Y. Li, F. Wang, P. Huang, T. Lu, and K. Xu, “Length-scale-dependent deformation mechanism of cu/x (x= ru, w) multilayer thin films,” *Materials Science and Engineering: A*, vol. 664, pp. 206–214, 2016.
- [116] D. Frenkel and B. Smit, *Understanding molecular simulation: from algorithms to applications*, vol. 1. Elsevier, 2001.

- [117] M. S. Daw and M. I. Baskes, “Embedded-atom method: Derivation and application to impurities, surfaces, and other defects in metals,” *Physical Review B*, vol. 29, no. 12, p. 6443, 1984.
- [118] G. P. Pun and Y. Mishin, “Embedded-atom potential for hcp and fcc cobalt,” *Physical Review B*, vol. 86, no. 13, p. 134116, 2012.
- [119] M. R. Hestenes and E. Stiefel, “Methods of conjugate gradients for solving linear systems,” *Journal of research of the National Bureau of Standards*, vol. 49, no. 6, pp. 409–436, 1952.
- [120] A. Stukowski, V. V. Bulatov, and A. Arsenlis, “Automated identification and indexing of dislocations in crystal interfaces,” *Modelling and Simulation in Materials Science and Engineering*, vol. 20, no. 8, p. 085007, 2012.
- [121] A. Stukowski, “Structure identification methods for atomistic simulations of crystalline materials,” *Modelling and Simulation in Materials Science and Engineering*, vol. 20, no. 4, p. 045021, 2012.
- [122] F. Huang, M. Kief, G. Mankey, and R. Willis, “Magnetism in the few-monolayers limit: A surface magneto-optic kerr-effect study of the magnetic behavior of ultrathin films of co, ni, and co-ni alloys on cu (100) and cu (111),” *Physical Review B*, vol. 49, no. 6, p. 3962, 1994.
- [123] R. Naik, C. Kota, J. Payson, and G. Dunifer, “Ferromagnetic-resonance studies of epitaxial ni, co, and fe films grown on cu (100)/si (100),” *Physical Review B*, vol. 48, no. 2, p. 1008, 1993.
- [124] P. Carcia, A. Meinhardt, and A. Suna, “Perpendicular magnetic anisotropy in pd/co thin film layered structures,” *Applied Physics Letters*, vol. 47, no. 2, pp. 178–180, 1985.

- [125] A. Chiba, K. Kumagai, N. Nomura, and S. Miyakawa, "Pin-on-disk wear behavior in a like-on-like configuration in a biological environment of high carbon cast and low carbon forged co-29cr-6mo alloys," *Acta materialia*, vol. 55, no. 4, pp. 1309–1318, 2007.
- [126] M. Srivastava, V. E. Selvi, V. W. Grips, and K. Rajam, "Corrosion resistance and microstructure of electrodeposited nickel-cobalt alloy coatings," *Surface and Coatings Technology*, vol. 201, no. 6, pp. 3051–3060, 2006.
- [127] W. Betteridge, "The properties of metallic cobalt," *Progress in Materials Science*, vol. 24, pp. 51–142, 1980.
- [128] X. Zhang, A. Misra, H. Wang, A. Lima, M. Hundley, and R. Hoagland, "Effects of deposition parameters on residual stresses, hardness and electrical resistivity of nanoscale twinned 330 stainless steel thin films," *Journal of applied physics*, vol. 97, no. 9, p. 094302, 2005.
- [129] X. Zhang, H. Wang, X. Chen, L. Lu, K. Lu, R. Hoagland, and A. Misra, "High-strength sputter-deposited cu foils with preferred orientation of nanoscale growth twins," *Applied Physics Letters*, vol. 88, no. 17, p. 173116, 2006.
- [130] X. Chen and L. Lu, "Work hardening of ultrafine-grained copper with nanoscale twins," *Scripta materialia*, vol. 57, no. 2, pp. 133–136, 2007.
- [131] B. Li, B. Cao, K. Ramesh, and E. Ma, "A nucleation mechanism of deformation twins in pure aluminum," *Acta Materialia*, vol. 57, no. 15, pp. 4500–4507, 2009.
- [132] O. Anderoglu, A. Misra, J. Wang, R. Hoagland, J. Hirth, and X. Zhang, "Plastic flow stability of nanotwinned cu foils," *International Journal of Plasticity*, vol. 26, no. 6, pp. 875–886, 2010.

- [133] N. Li, J. Wang, J. Huang, A. Misra, and X. Zhang, "Influence of slip transmission on the migration of incoherent twin boundaries in epitaxial nanotwinned cu," *Scripta Materialia*, vol. 64, no. 2, pp. 149–152, 2011.
- [134] D. Bufford, H. Wang, and X. Zhang, "High strength, epitaxial nanotwinned ag films," *Acta Materialia*, vol. 59, no. 1, pp. 93–101, 2011.
- [135] A. Hodge, T. Furnish, A. Navid, and T. Barbee Jr, "Shear band formation and ductility in nanotwinned cu," *Scripta Materialia*, vol. 65, no. 11, pp. 1006–1009, 2011.
- [136] N. Li, J. Wang, X. Zhang, and A. Misra, "In-situ tem study of dislocation-twin boundaries interaction in nanotwinned cu films," *Jom*, vol. 63, no. 9, p. 62, 2011.
- [137] D. Bufford, H. Wang, and X. Zhang, "Thermal stability of twins and strengthening mechanisms in differently oriented epitaxial nanotwinned ag films," *Journal of Materials Research*, vol. 28, no. 13, pp. 1729–1739, 2013.
- [138] D. Bufford, Y. Liu, Y. Zhu, Z. Bi, Q. Jia, H. Wang, and X. Zhang, "Formation mechanisms of high-density growth twins in aluminum with high stacking-fault energy," *Materials Research Letters*, vol. 1, no. 1, pp. 51–60, 2013.
- [139] D. Bufford, Y. Liu, J. Wang, H. Wang, and X. Zhang, "In situ nanoindentation study on plasticity and work hardening in aluminium with incoherent twin boundaries," *Nature communications*, vol. 5, p. 4864, 2014.
- [140] Y. Liu, J. Jian, Y. Chen, H. Wang, and X. Zhang, "Plasticity and ultra-low stress induced twin boundary migration in nanotwinned cu by in situ nanoindentation studies," *Applied Physics Letters*, vol. 104, no. 23, p. 231910, 2014.

- [141] S. Zheng, I. J. Beyerlein, J. S. Carpenter, K. Kang, J. Wang, W. Han, and N. A. Mara, “High-strength and thermally stable bulk nanolayered composites due to twin-induced interfaces,” *Nature communications*, vol. 4, p. 1696, 2013.
- [142] F. Sansoz, K. Lu, T. Zhu, and A. Misra, “Strengthening and plasticity in nanotwinned metals,” *MRS bulletin*, vol. 41, no. 4, pp. 292–297, 2016.
- [143] A. Kobler, T. Beuth, T. Klöffel, R. Prang, M. Moosmann, T. Scherer, S. Walheim, H. Hahn, C. Kübel, B. Meyer, T. Schimmel, and E. Bitzek, “Nanotwinned silver nanowires: structure and mechanical properties,” *Acta Materialia*, vol. 92, pp. 299–308, 2015.
- [144] R. Su, D. Neffati, S. Xue, Q. Li, Z. Fan, Y. Liu, H. Wang, Y. Kulkarni, and X. Zhang, “Deformation mechanisms in fcc co dominated by high-density stacking faults,” *Materials Science and Engineering: A*, vol. 736, pp. 12–21, 2018.
- [145] Y. Zhang, S. Xue, Q. Li, C. Fan, R. Su, J. Ding, H. Wang, H. Wang, and X. Zhang, “Microstructure and mechanical behavior of nanotwinned alti alloys with 9r phase,” *Scripta Materialia*, vol. 148, pp. 5–9, 2018.
- [146] S. Xue, W. Kuo, Q. Li, Z. Fan, J. Ding, R. Su, H. Wang, and X. Zhang, “Texture-directed twin formation propensity in al with high stacking fault energy,” *Acta Materialia*, vol. 144, pp. 226–234, 2018.
- [147] R. Yuan, I. J. Beyerlein, and C. Zhou, “Statistical dislocation activation from grain boundaries and its role in the plastic anisotropy of nanotwinned copper,” *Acta Materialia*, vol. 110, pp. 8–18, 2016.
- [148] A. Sedlmayr, E. Bitzek, D. S. Gianola, G. Richter, R. Mönig, and O. Kraft, “Existence of two twinning-mediated plastic deformation modes in au nanowhiskers,” *Acta Materialia*, vol. 60, no. 9, pp. 3985–3993, 2012.

- [149] A. Hodge, Y. Wang, and T. Barbee Jr, “Mechanical deformation of high-purity sputter-deposited nano-twinned copper,” *Scripta materialia*, vol. 59, no. 2, pp. 163–166, 2008.
- [150] Y. Kulkarni and R. J. Asaro, “Are some nanotwinned fcc metals optimal for strength, ductility and grain stability?,” *Acta Materialia*, vol. 57, no. 16, pp. 4835–4844, 2009.
- [151] J. Wang, O. Anderoglu, J. Hirth, A. Misra, and X. Zhang, “Dislocation structures of $\sigma_3 \{112\}$ twin boundaries in face centered cubic metals,” *Applied Physics Letters*, vol. 95, no. 2, p. 021908, 2009.
- [152] N. Lu, K. Du, L. Lu, and H. Ye, “Motion of $1/3 \langle 111 \rangle$ dislocations on $\sigma_3 \{112\}$ twin boundaries in nanotwinned copper,” *Journal of Applied Physics*, vol. 115, no. 2, p. 024310, 2014.
- [153] L. Lu, X. Chen, X. Huang, and K. Lu, “Revealing the maximum strength in nanotwinned copper,” *Science*, vol. 323, no. 5914, pp. 607–610, 2009.
- [154] W. Jian, G. Cheng, W. Xu, H. Yuan, M. Tsai, Q. Wang, C. Koch, Y. Zhu, and S. Mathaudhu, “Ultrastrong mg alloy via nano-spaced stacking faults,” *Materials Research Letters*, vol. 1, no. 2, pp. 61–66, 2013.
- [155] W. F. Hosford, “The mechanics of crystals and textured polycrystals,” *Oxford University Press(USA)*, 1993,, p. 248, 1993.
- [156] R. Hill, *The mathematical theory of plasticity*, vol. 11. Oxford university press, 1998.
- [157] Y. Li, Y. Chen, J. C. Walmsley, R. Mathinsen, S. Dumoulin, and H. J. Roven, “Faceted interfacial structure of $\{101^{-} 1\}$ twins in ti formed during equal channel angular pressing,” *Scripta Materialia*, vol. 62, no. 7, pp. 443–446, 2010.

- [158] G. G. Yapici, I. Karaman, and Z.-P. Luo, “Mechanical twinning and texture evolution in severely deformed ti-6al-4v at high temperatures,” *Acta materialia*, vol. 54, no. 14, pp. 3755–3771, 2006.
- [159] I. Kim, J. Kim, D. Shin, X. Liao, and Y. Zhu, “Deformation twins in pure titanium processed by equal channel angular pressing,” *Scripta Materialia*, vol. 48, no. 6, pp. 813–817, 2003.
- [160] Q. Yu, Z.-W. Shan, J. Li, X. Huang, L. Xiao, J. Sun, and E. Ma, “Strong crystal size effect on deformation twinning,” *Nature*, vol. 463, no. 7279, p. 335, 2010.
- [161] Y. Wang, M. Louie, Y. Cao, X. Liao, H. Li, S. Ringer, and Y. Zhu, “High-pressure torsion induced microstructural evolution in a hexagonal close-packed zr alloy,” *Scripta Materialia*, vol. 62, no. 4, pp. 214–217, 2010.
- [162] Y. Zhu, X. Liao, and X. Wu, “Deformation twinning in nanocrystalline materials,” *Progress in Materials Science*, vol. 57, no. 1, pp. 1–62, 2012.
- [163] S. Plimpton, “Fast parallel algorithms for short-range molecular dynamics,” *Journal of computational physics*, vol. 117, no. 1, pp. 1–19, 1995.
- [164] A. Stukowski, “Visualization and analysis of atomistic simulation data with ovito—the open visualization tool,” *Modelling and Simulation in Materials Science and Engineering*, vol. 18, no. 1, p. 015012, 2009.
- [165] R. Su, D. Neffati, J. Cho, Q. Li, J. Ding, H. Wang, Y. Kulkarni, and X. Zhang, “Phase transformation induced plasticity in high-strength hexagonal close packed co with stacking faults,” *Scripta Materialia*, vol. 173, pp. 32–36, 2019.
- [166] W. Burgers, “On the process of transition of the cubic-body-centered

- modification into the hexagonal-close-packed modification of zirconium,” *Physica*, vol. 1, no. 7-12, pp. 561–586, 1934.
- [167] M. Yoo, “Slip, twinning, and fracture in hexagonal close-packed metals,” *Metallurgical Transactions A*, vol. 12, no. 3, pp. 409–418, 1981.
- [168] V. Yamakov, D. Wolf, S. Phillpot, and H. Gleiter, “Deformation twinning in nanocrystalline Al by molecular-dynamics simulation,” *Acta Materialia*, vol. 50, no. 20, pp. 5005–5020, 2002.
- [169] M. Chen, E. Ma, K. J. Hemker, H. Sheng, Y. Wang, and X. Cheng, “Deformation twinning in nanocrystalline aluminum,” *Science*, vol. 300, no. 5623, pp. 1275–1277, 2003.
- [170] X. Liao, Y. Zhao, S. Srinivasan, Y. Zhu, R. Valiev, and D. Gunderov, “Deformation twinning in nanocrystalline copper at room temperature and low strain rate,” *Applied physics letters*, vol. 84, no. 4, pp. 592–594, 2004.
- [171] L. Zhang and Y. Han, “Twins formation and their role in nanostructuring of zirconium,” *Materials Science and Engineering: A*, vol. 523, no. 1-2, pp. 130–133, 2009.
- [172] X. Wu, K. Youssef, C. Koch, S. Mathaudhu, L. Kecskes, and Y. Zhu, “Deformation twinning in a nanocrystalline hcp Mg alloy,” *Scripta Materialia*, vol. 64, no. 3, pp. 213–216, 2011.
- [173] J. Huang, Y. Wu, and H. Ye, “Phase transformation of cobalt induced by ball milling,” *Applied physics letters*, vol. 66, no. 3, pp. 308–310, 1995.
- [174] F. Delogu, “Kinetics of allotropic phase transformation in cobalt powders undergoing mechanical processing,” *Scripta Materialia*, vol. 58, no. 2, pp. 126–129, 2008.

- [175] J. Sort, N. Mateescu, J. Nogues, S. Suriñach, and M. D. Baró, “Effect of the milling energy on the milling-induced hcp-fcc cobalt allotropic transformations,” in *Journal of Metastable and Nanocrystalline Materials*, vol. 12, pp. 126–133, Trans Tech Publ, 2002.
- [176] Y. Liu, D. Bufford, H. Wang, C. Sun, and X. Zhang, “Mechanical properties of highly textured cu/ni multilayers,” *Acta Materialia*, vol. 59, no. 5, pp. 1924–1933, 2011.
- [177] J. McKeown, A. Misra, H. Kung, R. Hoagland, and M. Nastasi, “Microstructures and strength of nanoscale cu–ag multilayers,” *Scripta materialia*, vol. 46, no. 8, pp. 593–598, 2002.
- [178] Y. Chen, Y. Liu, C. Sun, K. Yu, M. Song, H. Wang, and X. Zhang, “Microstructure and strengthening mechanisms in cu/fe multilayers,” *Acta materialia*, vol. 60, no. 18, pp. 6312–6321, 2012.
- [179] X. Zhang, A. Misra, H. Wang, T. Shen, M. Nastasi, T. Mitchell, J. Hirth, R. Hoagland, and J. Embury, “Enhanced hardening in cu/330 stainless steel multilayers by nanoscale twinning,” *Acta Materialia*, vol. 52, no. 4, pp. 995–1002, 2004.
- [180] P. Dayal, M. Z. Quadir, C. Kong, N. Savvides, and M. Hoffman, “Transition from dislocation controlled plasticity to grain boundary mediated shear in nanolayered aluminum/palladium thin films,” *Thin Solid Films*, vol. 519, no. 10, pp. 3213–3220, 2011.
- [181] W. Guo, E. Jäggle, J. Yao, V. Maier, S. Korte-Kerzel, J. M. Schneider, and D. Raabe, “Intrinsic and extrinsic size effects in the deformation of amorphous cuzr/nanocrystalline cu nanolaminates,” *Acta materialia*, vol. 80, pp. 94–106, 2014.

- [182] J. Zhang, J. Li, X. Liang, G. Liu, and J. Sun, "Achieving optimum mechanical performance in metallic nanolayered cu/x (x= zr, cr) micropillars," *Scientific reports*, vol. 4, p. 4205, 2014.
- [183] E. Fu, N. Li, A. Misra, R. Hoagland, H. Wang, and X. Zhang, "Mechanical properties of sputtered cu/v and al/nb multilayer films," *Materials Science and Engineering: A*, vol. 493, no. 1-2, pp. 283–287, 2008.
- [184] J. M. Wheeler, R. Raghavan, V. Chawla, J. Zechner, I. Utke, and J. Michler, "Failure mechanisms in metal–metal nanolaminates at elevated temperatures: Microcompression of cu–w multilayers," *Scripta Materialia*, vol. 98, pp. 28–31, 2015.
- [185] Y. Kim, A. S. Budiman, J. K. Baldwin, N. A. Mara, A. Misra, and S. M. Han, "Microcompression study of al-nb nanoscale multilayers," *Journal of Materials Research*, vol. 27, no. 3, pp. 592–598, 2012.
- [186] N. Li, M. Demkowicz, N. Mara, Y. Wang, and A. Misra, "Hardening due to interfacial he bubbles in nanolayered composites," *Materials Research Letters*, vol. 4, no. 2, pp. 75–82, 2016.
- [187] Y. Cui, B. Derby, N. Li, N. A. Mara, and A. Misra, "Suppression of shear banding in high-strength cu/mo nanocomposites with hierarchical bicontinuous intertwined structures," *Materials Research Letters*, vol. 6, no. 3, pp. 184–190, 2018.
- [188] Y. Lu, R. Kotoka, J. Ligda, B. Cao, S. Yarmolenko, B. Schuster, and Q. Wei, "The microstructure and mechanical behavior of mg/ti multilayers as a function of individual layer thickness," *Acta materialia*, vol. 63, pp. 216–231, 2014.
- [189] B. Ham and X. Zhang, "High strength mg/nb nanolayer composites," *Materials Science and Engineering: A*, vol. 528, no. 4-5, pp. 2028–2033, 2011.

- [190] S. Pathak, N. Velisavljevic, J. K. Baldwin, M. Jain, S. Zheng, N. A. Mara, and I. J. Beyerlein, “Strong, ductile, and thermally stable bcc-mg nanolaminates,” *Scientific reports*, vol. 7, no. 1, pp. 1–9, 2017.
- [191] D. Bhattacharyya, N. Mara, P. Dickerson, R. Hoagland, and A. Misra, “Compressive flow behavior of al–tin multilayers at nanometer scale layer thickness,” *Acta Materialia*, vol. 59, no. 10, pp. 3804–3816, 2011.
- [192] S. M. Han, M. A. Phillips, and W. D. Nix, “Study of strain softening behavior of al–al₃sc multilayers using microcompression testing,” *Acta Materialia*, vol. 57, no. 15, pp. 4473–4490, 2009.
- [193] C. Mayer, L. Yang, S. Singh, J. Llorca, J. Molina-Aldareguia, Y. Shen, and N. Chawla, “Anisotropy, size, and aspect ratio effects on micropillar compression of alsic nanolaminate composites,” *Acta Materialia*, vol. 114, pp. 25–32, 2016.
- [194] J. Zhang, G. Liu, and J. Sun, “Self-toughening crystalline cu/amorphous cu–zr nanolaminates: deformation-induced devitrification,” *Acta materialia*, vol. 66, pp. 22–31, 2014.
- [195] Z. Fan, S. Xue, J. Wang, K. Yu, H. Wang, and X. Zhang, “Unusual size dependent strengthening mechanisms of cu/amorphous cunb multilayers,” *Acta Materialia*, vol. 120, pp. 327–336, 2016.
- [196] Z. Fan, Q. Li, J. Li, S. Xue, H. Wang, and X. Zhang, “Tailoring plasticity of metallic glasses via interfaces in cu/amorphous cunb laminates,” *Journal of Materials Research*, vol. 32, no. 14, pp. 2680–2689, 2017.
- [197] M. D. Uchic, D. M. Dimiduk, J. N. Florando, and W. D. Nix, “Sample dimensions influence strength and crystal plasticity,” *Science*, vol. 305, no. 5686, pp. 986–989, 2004.

- [198] J. R. Greer and W. D. Nix, “Nanoscale gold pillars strengthened through dislocation starvation,” *Physical Review B*, vol. 73, no. 24, p. 245410, 2006.
- [199] J. Wang, C. Yang, and P. D. Hodgson, “Extrinsic size effect in microcompression of polycrystalline cu/fe multilayers,” *Scripta Materialia*, vol. 69, no. 8, pp. 626–629, 2013.
- [200] N. Mara, D. Bhattacharyya, J. Hirth, P. Dickerson, and A. Misra, “Mechanism for shear banding in nanolayered composites,” *Applied Physics Letters*, vol. 97, no. 2, p. 021909, 2010.
- [201] J. Wang, N. Li, O. Anderoglu, X. Zhang, A. Misra, J. Huang, and J. Hirth, “Detwinning mechanisms for growth twins in face-centered cubic metals,” *Acta Materialia*, vol. 58, no. 6, pp. 2262–2270, 2010.
- [202] Y. Zhu, X. Wu, X. Liao, J. Narayan, L. Kecskés, and S. Mathaudhu, “Dislocation–twin interactions in nanocrystalline fcc metals,” *Acta Materialia*, vol. 59, no. 2, pp. 812–821, 2011.
- [203] J. Zhang, S. Lei, Y. Liu, J. Niu, Y. Chen, G. Liu, X. Zhang, and J. Sun, “Length scale-dependent deformation behavior of nanolayered cu/zr micropillars,” *Acta Materialia*, vol. 60, no. 4, pp. 1610–1622, 2012.
- [204] Y. Li, X. Zhu, J. Tan, B. Wu, W. Wang, and G. Zhang, “Comparative investigation of strength and plastic instability in cu/au and cu/cr multilayers by indentation,” *Journal of Materials Research*, vol. 24, no. 3, pp. 728–735, 2009.
- [205] A. Misra, J. Hirth, R. Hoagland, J. Embury, and H. Kung, “Dislocation mechanisms and symmetric slip in rolled nano-scale metallic multilayers,” *Acta materialia*, vol. 52, no. 8, pp. 2387–2394, 2004.

- [206] J. Carpenter, A. Misra, M. Uchic, and P. Anderson, “Strain rate sensitivity and activation volume of cu/ni metallic multilayer thin films measured via micropillar compression,” *Applied Physics Letters*, vol. 101, no. 5, p. 051901, 2012.
- [207] R. Schoeppner, J. Wheeler, J. Zechner, J. Michler, H. Zbib, and D. Bahr, “Coherent interfaces increase strain-hardening behavior in tri-component nano-scale metallic multilayer thin films,” *Materials Research Letters*, vol. 3, no. 2, pp. 114–119, 2015.
- [208] N. Li, N. Mara, Y. Wang, M. Nastasi, and A. Misra, “Compressive flow behavior of cu thin films and cu/nb multilayers containing nanometer-scale helium bubbles,” *Scripta Materialia*, vol. 64, no. 10, pp. 974–977, 2011.
- [209] A. Misra, M. Verdier, H. Kung, J. Embury, and J. Hirth, “Deformation mechanism maps for polycrystalline metallic multilayers,” *Scripta Materialia*, vol. 41, no. 9, 1999.
- [210] S. I. Rao and P. M. Hazzledine, “Atomistic simulations of dislocation–interface interactions in the cu-ni multilayer system,” *Philosophical Magazine A*, vol. 80, no. 9, pp. 2011–2040, 2000.
- [211] O. Anderoglu, A. Misra, H. Wang, F. Ronning, M. Hundley, and X. Zhang, “Epitaxial nanotwinned cu films with high strength and high conductivity,” *Applied Physics Letters*, vol. 93, no. 8, p. 083108, 2008.
- [212] Z. Shan, L. Lu, A. Minor, E. Stach, and S. Mao, “The effect of twin plane spacing on the deformation of copper containing a high density of growth twins,” *Jom*, vol. 60, no. 9, pp. 71–74, 2008.
- [213] N. Lu, K. Du, L. Lu, and H. Ye, “Transition of dislocation nucleation induced

- by local stress concentration in nanotwinned copper,” *Nature communications*, vol. 6, p. 7648, 2015.
- [214] A. Karimpoor, U. Erb, K. Aust, and G. Palumbo, “High strength nanocrystalline cobalt with high tensile ductility,” *Scripta Materialia*, vol. 49, no. 7, pp. 651–656, 2003.
- [215] K. Davis and E. Teghtsoonian, “Deformation twins in cobalt,” *Acta Metallurgica*, vol. 10, no. 12, pp. 1189–1191, 1962.
- [216] C. Fan, Q. Li, J. Ding, Y. Liang, Z. Shang, J. Li, R. Su, J. Cho, D. Chen, Y. Wang, J. Wang, H. Wang, and X. Zhang, “Helium irradiation induced ultra-high strength nanotwinned cu with nanovoids,” *Acta Materialia*, vol. 177, pp. 107–120, 2019.
- [217] R. Su, D. Neffati, Q. Li, S. Xue, J. Cho, J. Li, J. Ding, Y. Zhang, C. Fan, H. Wang, Y. Kulkarni, and X. Zhang, “Ultra-high strength and plasticity mediated by partial dislocations and defect networks: Part i: Texture effect,” *Acta Materialia*, vol. 185, pp. 181–192, 2020.
- [218] W. Jian, G. Cheng, W. Xu, C. Koch, Q. Wang, Y. Zhu, and S. Mathaudhu, “Physics and model of strengthening by parallel stacking faults,” *Applied Physics Letters*, vol. 103, no. 13, p. 133108, 2013.
- [219] P. Gu, Y. Zhu, and S. N. Mathaudhu, “A model for $\langle c+a \rangle$ dislocation transmission across nano-spaced parallel basal stacking faults in a hcp alloy,” *Philosophical Magazine Letters*, vol. 95, no. 1, pp. 58–66, 2015.
- [220] R. Niu and K. Han, “Strain hardening and softening in nanotwinned cu,” *Scripta Materialia*, vol. 68, no. 12, pp. 960–963, 2013.

- [221] B. Wirth, V. Bulatov, and T. D. de la Rubia, “Dislocation-stacking fault tetrahedron interactions in cu,” *J. Eng. Mater. Technol.*, vol. 124, no. 3, pp. 329–334, 2002.
- [222] F. Hammami and Y. Kulkarni, “Rate dependence of grain boundary sliding via time-scaling atomistic simulations,” *Journal of Applied Physics*, vol. 121, no. 8, p. 085303, 2017.
- [223] J. R. Greer, W. C. Oliver, and W. D. Nix, “Size dependence of mechanical properties of gold at the micron scale in the absence of strain gradients,” *Acta Materialia*, vol. 53, no. 6, pp. 1821–1830, 2005.
- [224] Z. Shan, R. K. Mishra, S. S. Asif, O. L. Warren, and A. M. Minor, “Mechanical annealing and source-limited deformation in submicrometre-diameter ni crystals,” *Nature materials*, vol. 7, no. 2, p. 115, 2008.
- [225] J. R. Greer, J.-Y. Kim, and M. J. Burek, “The in-situ mechanical testing of nanoscale single-crystalline nanopillars,” *Jom*, vol. 61, no. 12, p. 19, 2009.
- [226] W. Jesser and J. Matthews, “Pseudomorphic deposits of cobalt on copper,” *Philosophical Magazine*, vol. 17, no. 147, pp. 461–473, 1968.
- [227] E. Martinez, J. Marian, A. Arsenlis, M. Victoria, and J. M. Perlado, “Atomistically informed dislocation dynamics in fcc crystals,” *Journal of the Mechanics and Physics of Solids*, vol. 56, no. 3, pp. 869–895, 2008.
- [228] H. Tang, K. Schwarz, and H. D. Espinosa, “Dislocation escape-related size effects in single-crystal micropillars under uniaxial compression,” *Acta Materialia*, vol. 55, no. 5, pp. 1607–1616, 2007.
- [229] Z.-J. Wang, Q.-J. Li, Z.-W. Shan, J. Li, J. Sun, and E. Ma, “Sample size effects

- on the large strain bursts in submicron aluminum pillars,” *Applied Physics Letters*, vol. 100, no. 7, p. 071906, 2012.
- [230] S. H. Oh, M. Legros, D. Kiener, and G. Dehm, “In situ observation of dislocation nucleation and escape in a submicrometre aluminium single crystal,” *Nature materials*, vol. 8, no. 2, p. 95, 2009.
- [231] J. Zhang, G. Liu, and J. Sun, “Strain rate effects on the mechanical response in multi-and single-crystalline cu micropillars: grain boundary effects,” *International Journal of Plasticity*, vol. 50, pp. 1–17, 2013.
- [232] A. T. Jennings, J. Li, and J. R. Greer, “Emergence of strain-rate sensitivity in cu nanopillars: Transition from dislocation multiplication to dislocation nucleation,” *Acta Materialia*, vol. 59, no. 14, pp. 5627–5637, 2011.
- [233] F. F. Csikor, C. Motz, D. Weygand, M. Zaiser, and S. Zapperi, “Dislocation avalanches, strain bursts, and the problem of plastic forming at the micrometer scale,” *Science*, vol. 318, no. 5848, pp. 251–254, 2007.